

EFFICIENT SOLUTION OF MAXWELL'S EQUATIONS USING THE NONUNIFORM
ORTHOGONAL FINITE DIFFERENCE TIME DOMAIN METHOD

BY

JOHN ALLAN SVIGELJ

B.S., Michigan State University, 1990
M.S., University of Illinois, 1992

THESIS

Submitted in partial fulfillment of the requirements
for the degree of Doctor of Philosophy in Electrical Engineering
in the Graduate College of the
University of Illinois at Urbana-Champaign, 1995

DISTRIBUTION STATEMENT A
Approved for public release.
Distribution Unlimited

Urbana, Illinois

REPORT DOCUMENTATION PAGE

Form Approved
OMB No. 0704-0188

Public reporting burden for this collection of information is estimated to average 1 hour per response, including the time for reviewing instructions, searching existing data sources, gathering and maintaining the data needed, and completing and reviewing the collection of information. Send comments regarding this burden estimate or any other aspect of this collection of information, including suggestions for reducing this burden, to Washington Headquarters Services, Directorate for Information Operations and Reports, 1215 Jefferson Davis Highway, Suite 1204, Arlington, VA 22202-4302, and to the Office of Management and Budget, Paperwork Reduction Project (0704-0188) Washington, DC 20503.

1. AGENCY USE ONLY (Leave Blank)	2. REPORT DATE 1995	3. REPORT TYPE AND DATES COVERED Final	
4. TITLE AND SUBTITLE Efficient Solution of Maxwell's Equations Using the Nonuniform Orthogonal Finite Difference Time Domain Method		5. FUNDING NUMBERS 11	
6. AUTHORS John Allan Svigelj			
7. PERFORMING ORGANIZATION NAME(S) AND ADDRESS(ES) University of Illinois at Urbana-Champaign			
9. SPONSORING/MONITORING AGENCY NAME(S) AND ADDRESS(ES) AFOSR/NI 110 Duncan Avenue, Room B-115 Bolling Air Force Base, DC 20332-8080		10. SPONSORING/MONITORING AGENCY REPORT NUMBER	
11. SUPPLEMENTARY NOTES			
12a. DISTRIBUTION AVAILABILITY STATEMENT Approved for Public Release		12b. DISTRIBUTION CODE	
13. ABSTRACT (Maximum 200 words) See attached.			
14. SUBJECT TERMS 19980115 223		15. NUMBER OF PAGES	
		16. PRICE CODE	
17. SECURITY CLASSIFICATION OF REPORT Unclassified	18. SECURITY CLASSIFICATION OF THIS PAGE Unclassified	19. SECURITY CLASSIFICATION OF ABSTRACT Unclassified	20. LIMITATION OF ABSTRACT UL

DTIC QUALITY INSPECTED 2

**EFFICIENT SOLUTION OF MAXWELL'S EQUATIONS USING THE NONUNIFORM
ORTHOGONAL FINITE DIFFERENCE TIME DOMAIN METHOD**

BY

JOHN ALLAN SVIGELJ

**B.S., Michigan State University, 1990
M.S., University of Illinois, 1992**

THESIS

**Submitted in partial fulfillment of the requirements
for the degree of Doctor of Philosophy in Electrical Engineering
in the Graduate College of the
University of Illinois at Urbana-Champaign, 1995**

Urbana, Illinois

UNIVERSITY OF ILLINOIS AT URBANA-CHAMPAIGN

THE GRADUATE COLLEGE

APRIL 1995

WE HEREBY RECOMMEND THAT THE THESIS BY

JOHN ALLAN SVIGELJ

ENTITLED EFFICIENT SOLUTION OF MAXWELL'S EQUATIONS USING THE
NONUNIFORM ORTHOGONAL FINITE DIFFERENCE TIME DOMAIN METHOD

BE ACCEPTED IN PARTIAL FULFILLMENT OF THE REQUIREMENTS FOR
THE DEGREE OF

DOCTOR OF PHILOSOPHY

R. Muth

Director of Thesis Research

N. Narayana Rao

Head of Department

Committee on Final Examination†

R. Muth

Chairperson

Paul E. May Jr.

Leon A. Trizell

Jose E. Schutt-Aine

† Required for doctor's degree but not for master's.

**EFFICIENT SOLUTION OF MAXWELL'S EQUATIONS USING THE
NONUNIFORM ORTHOGONAL FINITE DIFFERENCE TIME DOMAIN
METHOD**

John Allan Svilgelj, Ph.D.
Department of Electrical and Computer Engineering
University of Illinois at Urbana-Champaign, 1995
Raj Mittra, Advisor

The Finite Difference Time Domain (FDTD) method is limited by memory requirements and computation time when applied to large problems, complicated geometries, or geometries with fine features. In this thesis, the nonuniform orthogonal FDTD method is presented and applied to a variety of electromagnetic problems. The nonuniform aspect of the method gives great flexibility in modeling complicated geometries with fine features. Furthermore, the variability of the mesh resolution also enables the user to move the boundaries of the computational domain farther away from the center of the problem without an undue increase in the number of cells. Most significantly, the orthogonality of the method preserves the speed of the conventional FDTD method. These three features of the nonuniform orthogonal FDTD method are demonstrated by means of numerical examples throughout the thesis.

Grid dispersion error from the nonuniform mesh is analyzed and numerical examples are presented, demonstrating that small growth rates in mesh discretization lead to acceptably small errors. The issue of absorbing boundary conditions is addressed with the analysis and application of the dispersive boundary condition on nonuniform meshes. New techniques are also introduced for the efficient characterization of microstrip lines, microstrip discontinuities, and coupled microstrip structures using FDTD data. A local mesh refinement technique is introduced for planar perfect electric conductor, and is shown to be three times more accurate than the staircasing approximation.

The versatility of the method is demonstrated by the analysis of a balun-fed folded dipole antenna, the characterization of the transition of grounded coplanar waveguide to microstrip line, and the study of fields in lossy layered media.

DEDICATION

This thesis is dedicated to my grandparents, John and Annie Svigelj, Stanley and Pauline Yukevich, and my parents, John and Janis Svigelj, who taught me the importance of education, hard work, and perseverance.

ACKNOWLEDGMENTS

The author would like to express his gratitude to his advisor, Professor Raj Mittra, for his guidance during the course of the author's graduate study and for providing an exceptional environment for pursuing research in the area of electromagnetics. The author also thanks Professor Jose Schutt-Aine for his efforts in maintaining the computer resources utilized throughout the author's graduate study.

The author expresses his high regard for his doctoral committee, Professor Mittra, Professor Schutt-Aine, Professor Paul Mayes, and Professor Leon Frizzell.

The author acknowledges many members of the Electromagnetic Communication Laboratory and Electromagnetics Laboratory for their assistance and support. Special thanks go to Mr. Stevan Kosanovich for his numerous helpful explanations, suggestions, and insights regarding FDTD methods. Mr. Kosanovich was an invaluable resource for the author. The author is grateful to Dr. Dale Becker, Mr. Jonathon Veihl, Mr. Siva Chebolu, Mr. Robert Wagner, and Dr. Paul Harms for their helpful discussions about FDTD, and Mr. Michael O'Malley, Mr. Kosanovich, and Dr. Ikmo Park for their assistance with the experimental work carried out in this thesis. The author benefited greatly from the encouragement and support from Mr. Sean Ni, Mr. Veihl, Dr. Gregory Otto, Mr. Steve Eiken, Mr. Vaughn Betz, and Mr. Wagner.

The author would like to thank the University of Illinois, the Northrop Corporation, and the Department of Defense for the fellowships that provided financial support. The author thanks the Air Force Office of Scientific Research for giving the author the opportunity to carry out research at Rome Laboratory. In particular, the author wishes to express his appreciation to Dr. Hans Steyskal for his assistance and guidance. The author is grateful for the opportunity to teach. Special thanks go to Professor Jose Schutt-Aine, Mr. Jiun-Hwa Lin, and Mr. David Webb, who were great sources of information and help for the author in his teaching endeavors.

The author thanks Professor Edward Rothwell and Professor Dennis Nyquist for their guidance during the author's undergraduate education, and for their excellent instruction in electromagnetics.

The author expresses his sincere gratitude and love to his parents, brother, and sister, for their love and encouragement throughout the author's life. They have sparked the author's ambition and provided constant support for the author in his efforts.

Finally, it is with love and appreciation that the author thanks his fiancé, Allyson Logsdon, for her love, encouragement, support, and patience, upon which the author relied to ensure the timely completion of this thesis.

TABLE OF CONTENTS

CHAPTER	PAGE
1 INTRODUCTION	1
1.1 Overview	1
1.2 Outline of the Thesis	4
1.3 References	6
2 THE NONUNIFORM ORTHOGONAL FINITE DIFFERENCE TIME DOMAIN METHOD	7
2.1 Introduction	7
2.2 Uniform Finite Difference Time Domain Method	7
2.3 Nonuniform Orthogonal Finite Difference Time Domain Method	9
2.4 Error from Grid Dispersion on Nonuniform Grids	15
2.5 Finline Waveguide	21
2.6 Lossy Layered Media	24
2.7 Conclusions	31
2.8 References	32
3 THE DISPERSIVE ABSORBING BOUNDARY CONDITION APPLIED TO NONUNIFORM ORTHOGONAL MESHES	33
3.1 Introduction	33
3.2 The Mur Absorbing Boundary Conditions	34
3.3 Dispersive Boundary Condition	36
3.4 The Modified Dispersive Boundary Condition	37

3.5 Stability	38
3.6 Microstrip Line with Uniform Mesh	43
3.7 Microstrip Line with Nonuniform Mesh	47
3.8 Angle Absorbing Boundary Condition	51
3.9 Conclusions	64
3.10 References	64
4 CHARACTERIZATION OF MICROSTRIP LINES AND DISCONTINUITIES USING NONUNIFORM ORTHOGONAL FDTD	66
4.1 Introduction	66
4.2 Uniform Microstrip Line	67
4.3 Prony's Method for Scattering Parameter Extraction.....	70
4.4 Microstrip Line with Right-Angle Bend	72
4.5 Microstrip Line with Mitered Right-Angle Bend	75
4.6 Skewed stripline	79
4.7 Straight stripline	83
4.8 Coplanar Waveguide to Microstrip Line	86
4.9 Conclusions	92
4.10 References	93
5 CHARACTERIZATION OF COUPLED MICROSTRIP LINES AND COUPLED STRIPLINES USING NONUNIFORM ORTHOGONAL FDTD	95
5.1 Introduction	95
5.2 Symmetric Coupled Microstrip Lines	96

5.3 Prony's Method for Mode Extraction	101
5.4 Coupled Microstrip Lines	102
5.5 Asymmetric Coupled Microstrip Lines.....	104
5.6 Asymmetric Coupled Striplines	106
5.7 Conclusions	109
5.8 References	109
6 ANALYSIS OF MICROSTRIP ANTENNAS USING FDTD	111
6.1 Introduction	111
6.2 Near-Field to Far-field Transformation	111
6.3 Balun-Fed Folded Dipole	113
6.4 Microstrip-Line Fed Patch Antenna	122
6.5 Coaxial-Line Fed Patch Antenna	125
6.6 Conclusions	132
6.7 References	133
7 CONCLUSIONS AND FUTURE WORK	135
VITA	138

CHAPTER 1

INTRODUCTION

1.1 Overview

The Finite Difference Time Domain (FDTD) method was introduced to the electromagnetics community in 1966 [1.1]. The FDTD method solves Maxwell's equations in partial differential equation form. It is extremely versatile in that it is able to analyze geometrical structures with arbitrary inhomogeneities. This is an attractive aspect of the method when compared with integral equation methods, which require geometry-dependent Green's functions; these can be computationally expensive and difficult to derive for arbitrary inhomogeneities. Although approximations often exist, it frequently remains difficult to obtain robust representations of the Green's functions for the general case [1.2]. Moreover, the FDTD method does not require matrix operations, unlike the Finite Element Method and the Method of Moments. Depending upon the problem, the matrix operations present potential pitfalls for those methods because of ill-conditioned matrices, non-convergent solutions, or simply the computational expense of N by N matrix operations. Additionally, the FDTD method is inherently efficient since it is of order N [1.3].

The FDTD method is explicit and solves differential equations by stepping forward in time. Because it is a time domain method, solutions to transient excitations provide a wide band of results in the frequency domain. This is particularly useful when analyzing frequency-dependent structures, since the frequency-dependent results can be obtained from a single FDTD simulation. Furthermore, the FDTD method is an excellent tool for providing a means for field visualization as a function of time and space. This can be important when studying complex three-dimensional geometries, where analysis of time signatures of fields, voltages, or currents can lead to physical understanding. For example, questions of how a structure responds to various excitations, where sources of

scattering are located, or how discontinuities affect field propagation, can be answered by simply observing electric fields, magnetic fields, voltages, and/or currents, as functions of time and space.

There are several limitations to the FDTD method and these limitations are often related to the accurate description of the geometry being analyzed. When a structure has a fine feature that has to be accurately described, a fine discretization must be used in the computational domain. Complicated geometries are also difficult to model because all defining dimensions must be an integral multiple of the cell discretization in a given direction. This can lead to an exorbitant number of unknowns, which will result in an intractable problem because of either the amount of memory, or the amount of time, required to perform the numerical simulation. The same type of limitations arise when attempting to solve large problems. Here, large refers to problems on the order of 18 million unknowns, or problems with dimensions on the order of 7λ by 7λ by 7λ where the cell discretization is on the order of $\lambda/20$ and the platform used to run the FDTD code has 128 MB of RAM. With unlimited computer resources, any size problem can be solved. How long the simulation will take to run, however, is another issue.

The problem of modeling large problems or geometries with fine features has been addressed by several researchers who have reported expansion techniques [1.4], sub-cell gridding [1.5], and sub-cell modeling [1.6]. Of these methods, sub-cell modeling is the most accurate and can be incorporated into the FDTD update equations without loss of speed and does not require temporal interpolation. Another approach for solving large problems is to implement the FDTD algorithm on a parallel architecture [1.7]. This approach does permit the solution of large problems, but can be expensive in terms of simulation times because of the need to communicate large amounts of data at every time step.

The other geometrical feature that presents difficulties for the FDTD method is curves or angles other than 90° . The usual method for modeling these types of features is

to use a staircase approximation to the geometry. Local mesh refinement techniques have also been reported [1.8] and [1.9]. An alternative approach is to use the curvilinear FDTD method [1.10]. This method does a good job at accurately modeling geometries that have features that can be modeled with continuous non-orthogonal coordinate lines. Special conditions and update equations are required when irregular grids are encountered. The accuracy and enhanced modeling capability of the curvilinear method certainly does not come without a price. The curvilinear method requires at least twice as much memory as the conventional FDTD method to store covariant and contravariant field components, and the curvilinear method is slower because there are more operations in the update equations and conversions are required. In many instances, both the memory requirements and computational time required for the curvilinear method render the method prohibitively expensive. This situation should be remedied to an extent in the future by faster computer processors and the availability of machines with large amounts of memory.

The primary goals of this thesis are to present the nonuniform orthogonal FDTD method, and to demonstrate its applicability to a variety of electromagnetic problems. The nonuniform aspect of the method gives great flexibility in modeling geometries. Furthermore, the variability of the mesh resolution also enables the user to move the boundaries of the computational domain farther away from the center of the problem without an undue increase in the number of cells. Most significantly, the orthogonality of the method preserves the speed of the conventional FDTD method. These three features of the nonuniform orthogonal FDTD method are demonstrated by means of numerical examples throughout the thesis.

Long simulation run times can also be an undesirable characteristic of the FDTD method. The issue of temporal truncation and extrapolation, which must be applied with great care, is not addressed in this thesis. However, numerical techniques which enable the extraction of frequency-dependent information from a minimum number of FDTD

simulations are presented. Moreover, these same techniques can be applied to extract the reflections from imperfect absorbing boundary conditions.

Since the simulation time is directly proportional to the size of the computational domain, it is advantageous to keep the computational domain small. This involves one of the most important issues in electromagnetic modeling using the finite difference time domain method, which is the truncation of the computational domain with absorbing boundary conditions (ABCs). An underlying theme common to research concerning ABCs is that it is desirable to use an ABC which is not only accurate in the modeling of waves at the boundaries, but also can be brought close to the radiating source or discontinuity, thereby saving on the memory and computation requirements. Depending upon the problem being solved, the absorbing boundary should simulate the outward propagation of traveling waves at various angles of incidence, guided modes, or evanescent modes. Clearly, it is advantageous to have a robust absorbing boundary condition that can be used for different types of problems, i.e., guided wave or radiating wave. The modified dispersive absorbing boundary condition is such an ABC [1.11], and it is analyzed and implemented on a nonuniform grid in this thesis.

1.2 Outline of the Thesis

The nonuniform orthogonal FDTD method is applied to a wide variety of electromagnetic problems. Whenever possible, the FDTD results are compared with analytic expressions, experimentally measured results, or the results of other numerical methods, including results from circuit simulators. In certain instances, due to the uniqueness of the problem analyzed, comparisons are not possible.

Chapter 2 introduces the nonuniform orthogonal FDTD method after briefly describing the conventional FDTD method. The nonuniform algorithm is developed based upon the general curvilinear FDTD method. Following the derivation of the nonuniform orthogonal update equations, the error due to the nonuniform grid is

discussed. A theoretical analysis is followed by a numerical example. Finally, problems involving the finline waveguide and lossy layered media are analyzed using the nonuniform orthogonal FDTD method.

Chapter 3 presents the implementation of the dispersive boundary condition (DBC) on a nonuniform orthogonal grid. Motivation for the study of the DBC is provided with an analysis of the Mur ABCs. The DBC and modified DBC equations are derived, followed by a discussion on stability. The DBC for nonuniform grids is tested with a microstrip line problem and a general radiating problem. Error analysis is carried out in the time domain, the frequency domain, and spatially.

Chapter 4 presents a variety of methods for calculating the frequency-dependent characteristics of microstrip lines, striplines, and discontinuities. Use of a Prony technique with the FDTD method is presented and applied to two-port scattering parameter calculations. A local mesh refinement technique is introduced for triangular metallization and demonstrated to increase the accuracy of the FDTD method. The FDTD method and Prony technique are combined to analyze the complicated transition from a grounded coplanar waveguide to a microstrip line.

Chapter 5 uses the FDTD method to characterize coupled microstrip lines and coupled striplines. First, the symmetric problem is considered and an even and odd mode theory is used in addition to the methods of Chapter 4 to characterize the lines. The methods of Chapter 4 are extended to handle the asymmetric case. This new method is presented, followed by numerical examples analyzing coupled symmetric and asymmetric lines. A multidielectric asymmetric coupled stripline problem is also analyzed.

Chapter 6 uses the FDTD method to analyze microstrip antennas. The near-field to far-field transformation is discussed, followed by the analysis of a complicated balun fed folded dipole antenna. The benefits of using the nonuniform orthogonal FDTD method are demonstrated through the analysis of microstrip patch antennas. The results obtained are compared with experimental measurements.

Finally, Chapter 7 summarizes the results of this thesis and suggests topics for further study.

1.3 References

- [1.1] K. S. Yee, "Numerical solution of initial boundary value problems involving Maxwell's equations in isotropic media," *IEEE Trans. Antennas Propagat.*, vol. 14, pp. 302-307, May 1966.
- [1.2] D. B. Webb, "Efficient integral equation solution of electromagnetic scattering by arbitrarily-shaped objects in planar, multilayered media," Ph.D. dissertation, University of Illinois at Urbana-Champaign, 1995.
- [1.3] W. C. Chew, *Waves and Fields in Inhomogeneous Media*. New York: Van Nostrand Reinhold, 1990.
- [1.4] K. S. Kunz and R. J. Luebbers, "A technique for increasing the resolution of finite-difference solution of the Maxwell equation," *IEEE Trans. Electromagn. Compat.*, vol. 23, pp. 419-422, November 1981.
- [1.5] S. S. Zivanovic, K. S. Yee, and K. K. Mei, "A subgridding method for the time-domain finite-difference method to solve Maxwell's equations", *IEEE Trans. Microwave Theory Tech.*, vol. 39, no. 3, pp. 471-479, March 1991.
- [1.6] A. Taflove, K. R. Umashankar, B. Beker, F. Harfoush, and K. S. Yee, "Detailed FD-TD analysis of electromagnetic fields penetrating narrow slots and lapped joints in thick conducting screens," *IEEE Trans. Antennas Propagat.*, vol. 36, no. 2, pp. 247-257, February 1988.
- [1.7] V. Varadarajan and R. Mittra, "Finite-Difference Time-Domain (FDTD) analysis using distributed computing," *IEEE Microwave Guided Wave Lett.*, vol. 4, no. 5, pp. 144-145, May 1994.
- [1.8] T. G. Jurgens, A. Taflove, K. R. Umashankar, and T. G. Moore, "Finite-Difference Time-Domain modeling of curved surfaces," *IEEE Trans. Antennas Propagat.*, vol. 40, no. 4, pp. 357-366, April 1988.
- [1.9] J. Fang and J. Ren, "A locally conformed Finite-Difference Time-Domain algorithm for modeling arbitrary shape planar metal strips," *IEEE Trans. Microwave Theory Tech.*, vol. 41, no. 5, pp. 830-838, May 1993.
- [1.10] R. Holland, "Finite difference solution of Maxwell's equations in generalized nonorthogonal coordinates," *IEEE Trans. Nuc. Sci.*, vol. 30, no. 6, pp. 4589-4591, December 1983.
- [1.11] V. Betz and R. Mittra, "Comparison and evaluation of boundary conditions for the absorption of guided waves in an FDTD simulation," *IEEE Trans. Microwave Guided Wave Lett.*, vol. 2, pp. 499-501, December 1992.

CHAPTER 2

THE NONUNIFORM ORTHOGONAL FINITE DIFFERENCE TIME DOMAIN METHOD

2.1 Introduction

In this chapter the Nonuniform Orthogonal Finite Difference Time Domain method is presented. After first considering the conventional uniform FDTD method, the nonuniform algorithm is developed based upon the general curvilinear FDTD method. The development entails the discussion of basis vectors, metrics, and field locations. Following the derivation of the nonuniform orthogonal update equations, the error due to the nonuniform grid is discussed. A theoretical analysis is followed by a numerical example. Finally, examples of electromagnetics problems that are well-suited to the nonuniform method are presented. Specifically, problems involving the finline waveguide and lossy layered media are analyzed.

2.2 Uniform Finite Difference Time Domain Method

The Finite Difference Time Domain (FDTD) method was introduced to the electromagnetics community by Yee in 1966 [2.1]. Because of its versatility and the advances in computer capability, it has enjoyed widespread use in recent years. The FDTD method discretizes Maxwell's equations in both space and time using second-order accurate central difference formulas. Arbitrary geometries are described on a uniform rectangular mesh, and the electric and magnetic fields are determined at discrete locations within the mesh as functions of time. The electric field values are located on the edges of the rectangular FDTD cells, and the magnetic field values are located at the centers of the faces of the cells. The dimensions of each cell are Δx by Δy by Δz , and the time step is Δt . The time step is related to the mesh discretization through the Courant

stability criterion shown in (2.1), where c is the velocity of light in the medium. The method becomes unstable when (2.1) is violated, but for optimal performance, Δt should be chosen as large as possible [2.2].

$$\Delta t \leq \frac{1}{c \sqrt{\frac{1}{\Delta x^2} + \frac{1}{\Delta y^2} + \frac{1}{\Delta z^2}}} \quad (2.1)$$

The electric field at time $n\Delta t$ is updated in terms of the electric field at the same location at time $(n-1)\Delta t$ and the surrounding magnetic fields at time $(n-1/2)\Delta t$. The update equations for the x-components of the electric and magnetic fields are given in (2.2) and (2.3).

$$\begin{aligned} E_x^n(i, j, k) = & \left(\left(1 - \frac{\sigma \Delta t}{2\epsilon} \right) / \left(1 + \frac{\sigma \Delta t}{2\epsilon} \right) \right) \cdot E_x^{n-1}(i, j, k) \\ & + \left(\left(\frac{\Delta t}{\epsilon} \right) / \left(1 + \frac{\sigma \Delta t}{2\epsilon} \right) \right) \cdot \left(\left(\frac{H_y^{n-1/2}(i, j, k) - H_y^{n-1/2}(i, j, k+1)}{\Delta z} \right) \right. \\ & \left. - \left(\frac{H_z^{n-1/2}(i, j, k) - H_z^{n-1/2}(i, j+1, k)}{\Delta y} \right) \right) \end{aligned} \quad (2.2)$$

$$\begin{aligned} H_x^{n+1/2}(i, j, k) = & H_x^{n-1/2}(i, j, k) + \left(\frac{\Delta t}{\mu} \right) \\ & \cdot \left(\left(\frac{E_y^n(i, j, k-1) - E_y^n(i, j, k)}{\Delta z} \right) - \left(\frac{E_z^n(i, j-1, k) - E_z^n(i, j, k)}{\Delta y} \right) \right) \end{aligned} \quad (2.3)$$

where $F^n(i, j, k) = F(i\Delta x, j\Delta y, k\Delta z; n\Delta t)$, σ is the electrical conductivity, μ is the permeability, and ϵ is the permittivity. Update equations for the other field components are obtained by permuting the fields and indices.

2.3 Nonuniform Orthogonal Finite Difference Time Domain Method

In this section, the update equations for nonuniform orthogonal FDTD will be derived from curvilinear FDTD update equations. Before deriving the update equations, the basis vectors, metrics, covariant fields, contravariant fields, and physical fields will be discussed. The presentation here will follow that of Holland [2.3]. Any general coordinate system can be characterized by unitary basis vectors, $(\vec{a}_1, \vec{a}_2, \vec{a}_3)$. In general, these vectors need not be orthogonal to each other and are not of unit length. However, for the purposes of this work, the vectors will be orthogonal to each other. Typical basis vectors used in this work, shown in Fig. 2.1, are parallel to the edges of the cell. Reciprocal basis vectors can also be used to characterize the coordinate system and can be defined in terms of the basis vectors as follows:

$$\vec{a}^i = \vec{a}_j \times \vec{a}_k / \sqrt{g} \quad (2.4)$$

where \sqrt{g} is equal to the volume of the rectangular prism formed by the basis vectors $(\vec{a}_1, \vec{a}_2, \vec{a}_3)$. These orthogonal vectors satisfy the following properties:

$$\vec{a}_i \cdot \vec{a}^j = \delta_{ij} \quad (2.5)$$

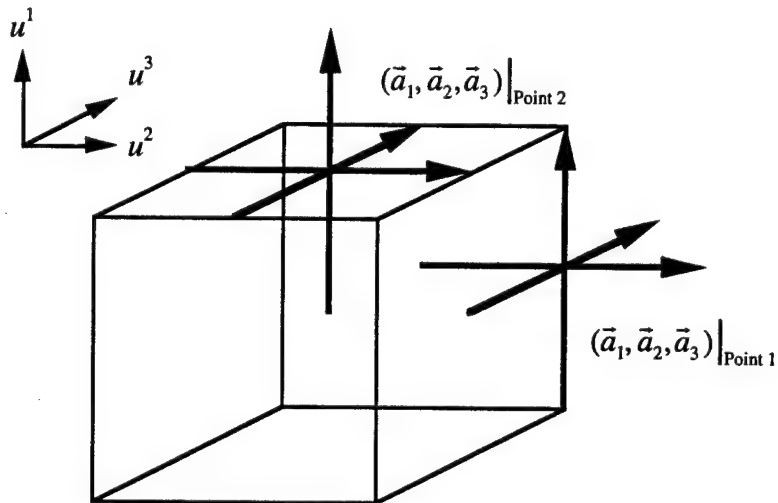


Figure 2.1 Basis vectors shown at two points on a typical FDTD cell. Point 1 is located at the center of an edge along the u^1 coordinate line, and Point 2 is located at the center of a face normal to the u^1 coordinate line.

$$\vec{a}_i \cdot \vec{a}_j = \delta_{ij} g_{ij} \quad (2.6)$$

$$\vec{a}^i \cdot \vec{a}^j = \delta_{ij} g^{ij} \quad (2.7)$$

where g_{ij} is the inverse of g^{ij} and δ_{ij} is the Kronecker delta function.

A general vector can be written in terms of its covariant components, as in (2.8), or in terms of its contravariant components, as in (2.9).

$$\vec{E} = \sum_{i=1}^3 e_i \vec{a}^i \quad (2.8)$$

$$\vec{E} = \sum_{i=1}^3 e^i \vec{a}_i \quad (2.9)$$

The e_i and e^i are related by the following formulas:

$$e_i = g_{ij} e^j \delta_{ij} \quad (2.10)$$

$$e^i = g^{ij} e_j \delta_{ij} \quad (2.11)$$

The e_i and e^i are not physical fields. The physical fields are related to the e_i and e^i as follows:

$$E_i = \sqrt{g^{ii}} e_i \quad (2.12)$$

$$E^i = \sqrt{g_{ii}} e^i \quad (2.13)$$

and the physical fields are related by the following expressions

$$E_i = G_{ij} E^j \quad (2.14)$$

$$E^i = G^{ij} E_j \quad (2.15)$$

where

$$G_{ij} = \sqrt{\frac{g^{jj}}{g_{ii}}} g_{ij} \quad (2.16)$$

$$G^{ij} = \sqrt{\frac{g_{ii}}{g^{jj}}} g^{ij} \quad (2.17)$$

However, from the above definitions for g_{ij} and g^{ij} , (2.14) and (2.15) simplify to $E_i = E^i$.

Using the above definitions, the first component of Faraday's law in point form can be written as

$$-\mu \frac{\partial H^1}{\partial t} = \sqrt{\frac{g_{11}}{g}} \left(\frac{\partial (E_3 / \sqrt{g^{33}})}{\partial u^2} - \frac{\partial (E_2 / \sqrt{g^{22}})}{\partial u^3} \right) \quad (2.18)$$

where the u^i are the coordinate lines of the curvilinear system and the permeability is not a function of time. Similarly, the first component of Ampere's law in point form can be written as

$$\epsilon \frac{\partial E^1}{\partial t} + \sigma E^1 = \sqrt{\frac{g_{11}}{g}} \left(\frac{\partial (H_3 / \sqrt{g^{33}})}{\partial u^2} - \frac{\partial (H_2 / \sqrt{g^{22}})}{\partial u^3} \right) \quad (2.19)$$

A leapfrog scheme is usually used to solve (2.18) and (2.19). First, (2.18) is solved for the H^i , which are then converted to H_i . Then, (2.19) is solved for the E^i . The E^i are converted to E_i and used to solve (2.18), and the process is repeated. For the orthogonal case, it has been shown that $E_i = E^i$. Consequently, the conversions are not necessary. Moreover, it will be demonstrated that the discretized versions of (2.18) and (2.19) reduce to simple forms requiring the same number of operations as (2.2) and (2.3).

Using central differences, (2.18) is written as

$$\begin{aligned} H^1(i, j, k)^{n+1/2} &= H^1(i, j, k)^{n-1/2} + \frac{\sqrt{g_{11}/g}}{\mu/\Delta t} \Big|_{H_1} \\ &\cdot \left(\frac{E_2(i, j, k)^n / \sqrt{g^{22}} - E_2(i, j, k-1)^n / \sqrt{g^{22}}}{U_n(i, j, k) - U_n(i, j, k-1)} \Big|_{E_2} \right. \\ &\left. + \frac{E_3(i, j-1, k)^n / \sqrt{g^{33}} - E_3(i, j, k)^n / \sqrt{g^{33}}}{U_n(i, j, k) - U_n(i, j-1, k)} \Big|_{E_3} \right) \end{aligned} \quad (2.20)$$

where μ and $\sqrt{g_{11}/g}$ are evaluated at the H_i mesh points and the $\sqrt{g^{ii}}$ are evaluated at the E_i mesh points, as the notation indicates. The U_n s are the successive points of the curvilinear coordinates and, by definition, their difference is unity.

Since the nonuniform orthogonal system considered in this work is Cartesian, the coordinate lines (u^1, u^2, u^3) correspond directly to the x-, y-, and z-directions. Figure 2.2 shows that the E_x and H_x (E_1 and H_1) components are located at positions marked with unfilled and filled triangles, respectively. The y- and z-component positions are marked with circles and squares, respectively. Cell nodes are located at cell vertices and labeled with U_n , and cell face centers are labeled with U_c . The following definitions are made to assist in the simplification process. Let $d_{xn}(i)$ be the distance between two nodes located at i and $i-1$. Similarly, let $d_{yn}(j)$ be the distance between two nodes at j and $j-1$, and $d_{zn}(k)$ be the distance between nodes at k and $k-1$. Define $d_{xc}(i)$ as the distance between the cell centers $U_c^2(i+1, j, k)$ and $U_c^2(i, j, k)$ as shown in Fig. 2.2. Note that $d_{xc}(i)$ is also equal to the distance between cell centers $U_c^3(i+1, j, k)$ and $U_c^3(i, j, k)$. Let $d_{yc}(j)$ and $d_{zc}(k)$ be defined similarly.

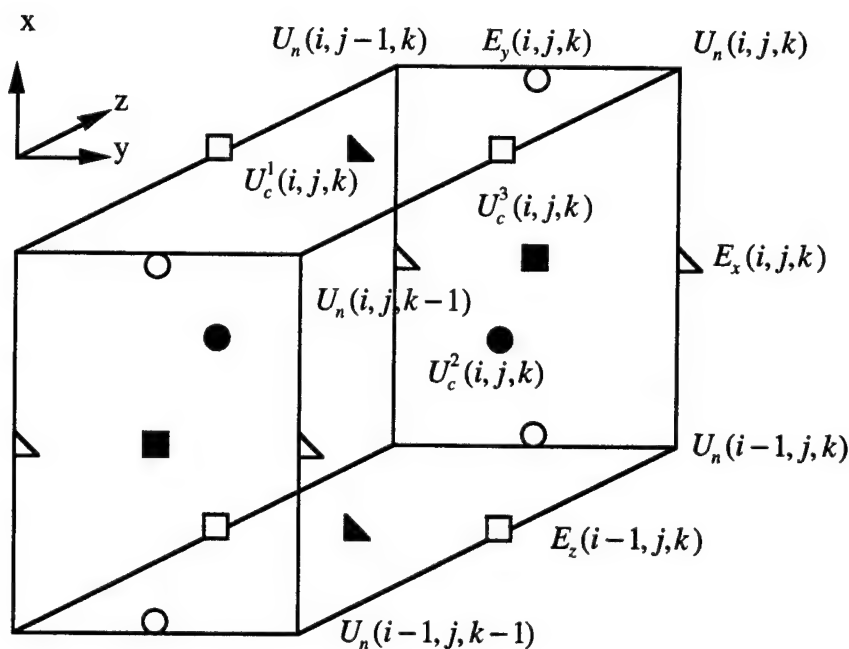


Figure 2.2 Typical FDTD cell showing locations of the electric and magnetic fields. Electric fields are located along cell edges and magnetic fields are located at cell face centers, labeled U_c . The cell nodes are labeled U_n .

Using these definitions, the various factors in (2.20) can be evaluated and simplified.

$$g_{11}|_{H_1(i,j,k)} = dxc(i) \cdot dxc(i) \quad (2.21)$$

$$\sqrt{g}|_{H_1(i,j,k)} = dxc(i) \cdot dyn(j) \cdot dzn(k) \quad (2.22)$$

$$\sqrt{g^{22}}|_{E_2(i,j,k)} = \sqrt{g^{22}}|_{E_2(i,j,k-1)} = 1/dyn(j) \quad (2.23)$$

$$\sqrt{g^{33}}|_{E_3(i,j,k)} = \sqrt{g^{33}}|_{E_3(i,j-1,k)} = 1/dzn(k) \quad (2.24)$$

Substituting (2.21) through (2.24) into (2.20) and simplifying result in the following equation.

$$H^1(i,j,k)^{n+1/2} = H^1(i,j,k)^{n-1/2} + \frac{\Delta t}{\mu} \cdot \left(\frac{E_2(i,j,k)^n - E_2(i,j,k-1)^n}{dzn(k)} + \frac{E_3(i,j-1,k)^n - E_3(i,j,k)^n}{dyn(j)} \right) \quad (2.25)$$

Equation (2.25) is identical in form to (2.3).

Turning now to (2.19), central differencing leads to (2.26).

$$E^1(i,j,k)^{n+1} = \left(\left(1 - \frac{\sigma \Delta t}{2\epsilon} \right) / \left(1 + \frac{\sigma \Delta t}{2\epsilon} \right) \right)_{E_1} E^1(i,j,k)^n + \sqrt{g_{11}/g} \left(\left(\frac{\Delta t}{\epsilon} \right) / \left(1 + \frac{\sigma \Delta t}{2\epsilon} \right) \right)_{E_1} \cdot \left(\left(\frac{H_2(i,j,k)^{n+1/2} / \sqrt{g^{22}} - H_2(i,j,k+1)^{n+1/2} / \sqrt{g^{22}}}{U_c^2(i,j,k+1) - U_c^2(i,j,k)} \right)_{H_2} + \left(\frac{H_3(i,j+1,k)^{n+1/2} / \sqrt{g^{33}} - H_3(i,j,k)^{n+1/2} / \sqrt{g^{33}}}{U_c^3(i,j+1,k) - U_c^3(i,j,k)} \right)_{H_3} \right) \quad (2.26)$$

Again, note that the denominators of the partials with respect to the curvilinear coordinates are unity by definition. The metric factors are evaluated in the following equations.

$$g_{11}|_{E_1(i,j,k)} = dxn(i) \cdot dxn(i) \quad (2.27)$$

$$\sqrt{g}|_{E_1(i,j,k)} = dxn(i) \cdot dyc(j) \cdot dzc(k) \quad (2.28)$$

$$\sqrt{g^{22}}|_{H_2(i,j,k)} = \sqrt{g^{22}}|_{H_2(i,j,k+1)} = 1/dyc(j) \quad (2.29)$$

$$\sqrt{g^{33}}|_{H_3(i,j,k)} = \sqrt{g^{33}}|_{H_3(i,j+1,k)} = 1/dzc(k) \quad (2.30)$$

Substituting Equations (2.27) through (2.30) into (2.26) results in

$$\begin{aligned} E^1(i,j,k)^{n+1} = & \left(\left(1 - \frac{\sigma \Delta t}{2\epsilon} \right) / \left(1 + \frac{\sigma \Delta t}{2\epsilon} \right) \right) E^1(i,j,k)^n \\ & + \left(\left(\frac{\Delta t}{\epsilon} \right) / \left(1 + \frac{\sigma \Delta t}{2\epsilon} \right) \right) \left(\left(\frac{H_2(i,j,k)^{n+1/2} - H_2(i,j,k+1)^{n+1/2}}{dzc(k)} \right) \right. \\ & \left. + \left(\frac{H_3(i,j+1,k)^{n+1/2} - H_3(i,j,k)^{n+1/2}}{dyc(j)} \right) \right) \end{aligned} \quad (2.31)$$

which is identical in form to Equation (2.2).

It is important to note that since the nonuniform orthogonal update equations are identical in form to the uniform update equations, there is no loss of speed when updating the fields. Care must be taken when computing the coefficients in the nonuniform update equations since variable cell discretization must be taken into account in order to accurately weight the coefficients when dealing with interfaces between different media [2.4]. However, the advantages from memory savings and decrease in total run time due to a smaller number of unknowns far outweigh this slight disadvantage. For many classes of problems, this difficulty can be avoided entirely by requiring that cell discretizations normal to a material interface be equal, in which case, the algorithm can be implemented with the same efficiency as the uniform method.

2.4 Error from Grid Dispersion on Nonuniform Grids

It is clear that the ability to allow the FDTD mesh to vary will result in a reduction in the number of unknowns. The mesh can be dense in areas where fine features must be accurately modeled and then allowed to expand or grow to a relatively "coarse" mesh in areas where fine discretization is not necessary. However, one cannot simply allow the mesh to grow at an arbitrary rate. The mesh must be varied gradually; otherwise, phase error due to grid dispersion will contaminate the solution at an unacceptable level. An excellent discussion of grid dispersion error can be found in [2.5]. The development in [2.5] will be followed here, simplified to the one-dimensional case and perturbed to include the nonuniformity of the grid.

Consider the scalar wave equation for homogenous media given in (2.32).

$$\frac{1}{c^2} \frac{\partial^2}{\partial t^2} \phi(z, t) = \nabla^2 \phi(z, t) \quad (2.32)$$

Since any wave can be expressed as a sum of plane waves, solutions of (2.32) are comprised of plane waves.

$$\phi(z, t) = A(t) e^{-jk_z z} \quad (2.33)$$

The discretized form of the plane wave in (2.33) is given in (2.34).

$$\phi_m^l = e^{j\omega\Delta t} e^{-jk_z m\Delta z} \quad (2.34)$$

Discretizing (2.32) using central differencing results in (2.35).

$$\phi_m^{l+1} = \left(\frac{\Delta t}{\Delta z} \right)^2 c^2 (\phi_{m+1}^l - 2\phi_m^l + \phi_{m-1}^l) + 2\phi_m^l - \phi_m^{l-1} \quad (2.35)$$

Substituting (2.34) into (2.35) results in the one-dimensional numerical dispersion relation given in (2.36).

$$\sin\left(\frac{\omega\Delta t}{2}\right) = \left(\frac{c\Delta t}{\Delta z}\right) \sin\left(\frac{k_z \Delta z}{2}\right) \quad (2.36)$$

Now, consider a cell whose discretization, Δz_2 , is larger than Δz . Solving (2.36) for the numerical propagation constant yields

$$\beta = \frac{2}{\Delta t} \sin^{-1} \left[\frac{c \Delta t}{\Delta z_2} \sin \left(\frac{k_o \Delta z_2}{2} \right) \right] \quad (2.37)$$

where $\beta = \omega/c$ and $k_o = k_z$. Equation (2.37) is an exact solution to the numerical dispersion relation (2.36). An approximate solution to (2.36) can be obtained by writing

$$\sin \left(\frac{\omega \Delta t}{2} \right) = rs \quad (2.38)$$

where $r = \frac{c \Delta t}{\Delta z}$ and $s = \sin \left(\frac{k_z \Delta z}{2} \right)$. Using series expansions for $\sin x$ and $\sin^{-1} x$ and retaining second-order terms yield the approximate solution to the numerical dispersion relation

$$\beta = k_o \left[1 - \frac{(k_o \Delta z_2)^2}{24} + \frac{(c \Delta t)^2 k_o^2}{24} \right] \quad (2.39)$$

where $\beta = \omega/c$ and $k_o = k_z$.

Suppose that Δz_1 is the minimum cell discretization and that Δt is chosen such that $\Delta t = \Delta z_1/c$. Clearly, there is no phase error due to grid dispersion if $\Delta z_2 = \Delta z_1$ in (2.37) and (2.39). When $\Delta z_2 \neq \Delta z_1$, then (2.37) and (2.39) can be used to determine the normalized phase error for a given cell as a function of the ratio $\Delta z_2/\Delta z_1$. For example, let $\Delta z_1 = 10$ mm and allow Δz_2 to vary. At a frequency of 1.5 GHz, $\Delta z_1 = \lambda/20$. Since the largest practical value of Δz_2 is $\lambda/10$, the ratio $\Delta z_2/\Delta z_1$ can range from 1 to 2. The percent error in normalized phase is plotted in Fig. 2.3, where M1 refers to (2.37) and M2 refers to (2.39) and the frequency values, f , are given in gigahertz. The agreement between methods M1 and M2 verifies the approximations made in deriving (2.39). For $f = 1.5$ GHz, there is a 1.2% error in the normalized phase at a ratio of 2. For $f = 0.75$ GHz, the ratio goes up to 4 where the error is about 1.55%. This error is per cell, so the error will accumulate as the field propagates from cell to cell. It is evident that the smaller the cell size in terms of wavelength, the larger the acceptable growth ratio between cells. For example, there is less than 0.2% error at $f = 1.5$ GHz for a ratio of 1.2 and less than 0.2% error at $f = 0.75$ GHz for a ratio of 1.6.

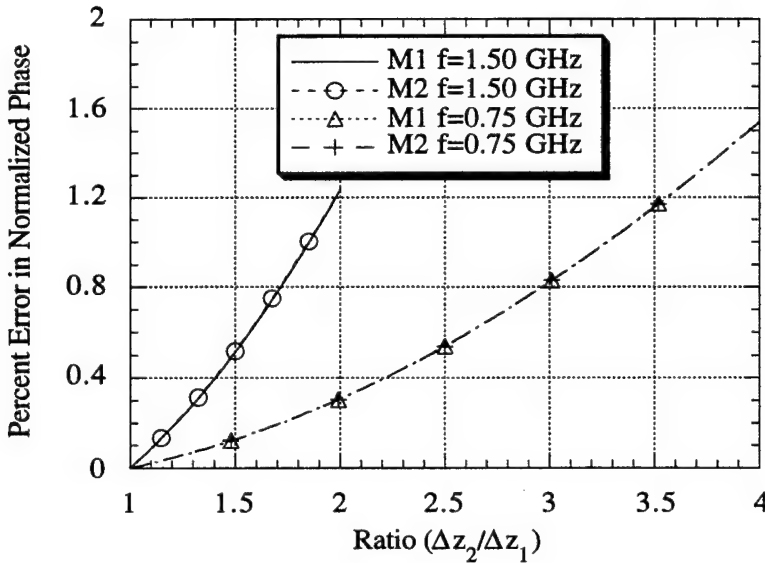


Figure 2.3 Percent error in normalized phase per cell for two frequencies and two methods. M1 refers to (2.37) and M2 refers to (2.39).

In practical applications, Δt is usually chosen less than the value specified by the Courant stability criterion, (2.1). To show how this affects the error due to the nonuniform grid, consider $\Delta z_1 = 10$ mm and $f = 1.5$ GHz. Rewriting (2.39) leads to

$$\beta = k_o \left[1 - \frac{\pi^2}{2400} \left(\left(\frac{\Delta z_2}{\Delta z_1} \right)^2 - \eta^2 \right) \right] \quad (2.40)$$

where $\beta = \omega/c$, $k_o = k_z$, and $c\Delta t = \eta\Delta z_1$. Figure 2.4 shows that varying the time step increases the percent error in the normalized phase by not more than 0.1 % when η is at least 0.9.

To test the effect of the nonuniformity of the grid on a practical numerical example, a stripline embedded in free space was analyzed. Since the stripline structure supports a TEM mode, the grid dispersion error can be determined by varying the grid in the direction of propagation and calculating the relative dielectric constant. In this case, the relative dielectric constant should be one. The geometry of the stripline is shown in Fig. 2.5(a), where the separation between the ground planes, H , is 6.0 mm, and the width,

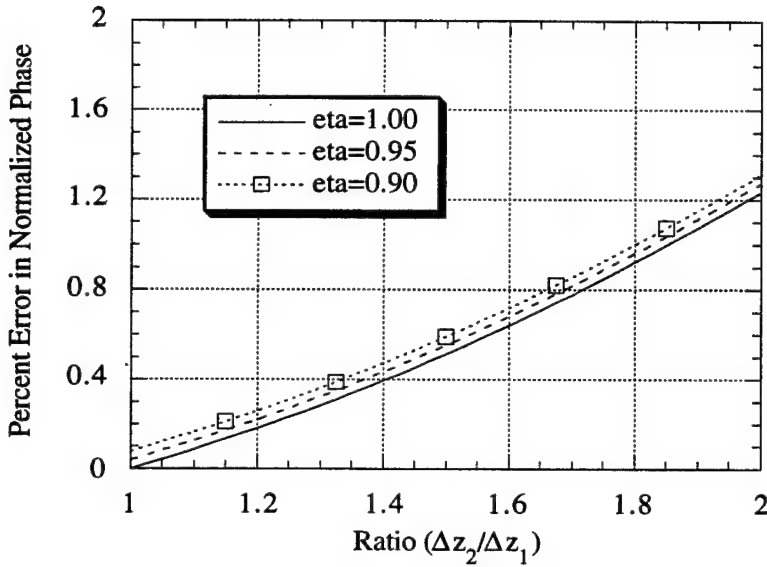


Figure 2.4 Percent error in normalized phase per cell for $f = 1.5$ GHz and $\eta = c\Delta t / \Delta z_1$ where $\Delta z_1 = \lambda / 20$.

W , of the centered stripline is 4.0 mm. The cross-section of the stripline is discretized uniformly with $\Delta x = \Delta y = 500 \mu\text{m}$. The line runs in the z -direction, and an example of 15 cells of uniform cell discretization is shown in Fig. 2.5(b), and a nonuniform discretization with growth rate 1.2 is shown in Fig. 2.5(c). Note that in Fig. 2.5(c) the mesh begins expanding with the 12th cell and stops at the 15th cell. The first eleven cells are uniformly discretized. The smallest cell in the z -direction is $\Delta z_1 = 500 \mu\text{m}$ and the largest cell is $\Delta z_2 = 1.0 \text{ mm}$.

The effective dielectric constant is calculated by monitoring the current at two locations along the line, 15 cells apart. Depending on the cell discretization, the distance, L , between the two points will vary. The time domain signatures of the currents at the two positions are transformed into the frequency domain and the effective dielectric constant is then given by (2.41)

$$\epsilon_{\text{ref}}(\omega) = \left[\left(\frac{c_o}{\omega L} \right) \ln \left(\frac{\tilde{I}(d)}{\tilde{I}(d+L)} \right) \right]^2 \quad (2.41)$$

where \tilde{I} is a function of frequency.

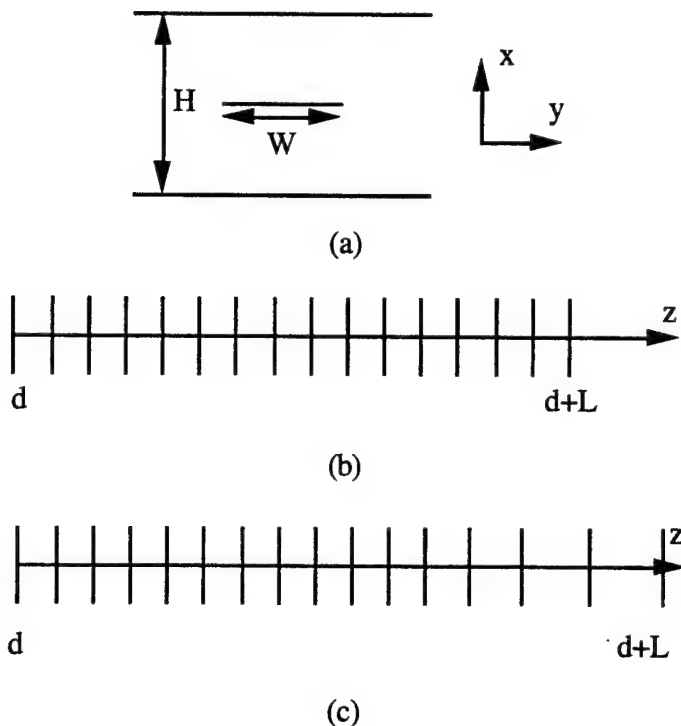


Figure 2.5 Geometry of stripline used to test numerical grid dispersion. (a) Cross-section of stripline, $W = 4.0$ mm, $H = 6.0$ mm. (b) Uniform cell discretization in the direction of propagation. (c) Nonuniform cell discretization in the direction of propagation with growth rate 1.2, cells growing near the "d+L" location.

Six different growth rates were tested and the value of the effective dielectric constant is shown in Fig. 2.6, where the curves are labeled on the graph according to the growth rate of the mesh. Note that the uniform case (growth rate = 1.0) results in a maximum error of 0.75 % at 30 GHz. The nonuniform cells were positioned within the 15-cell region such that the largest cell was the 15th cell. This explains the fact that a growth rate of 1.1 gives rise to more total error than larger growth rates for frequencies up to about 23 GHz. When the growth rate is 1.1, it takes seven cells to go from Δz_1 to Δz_2 , whereas using larger growth rates, a much smaller number of cells is used in the transition from Δz_1 to Δz_2 . When the mesh grows from the first monitoring location, the total error exhibits the expected behavior as a function of frequency and the growth rate,

as shown in Fig. 2.7. Error accumulates as the field propagates from "d" to "d+L" and the larger cells contribute more error per cell. For a growth rate of 1.2, the accumulated error is about 1.32 % at 30 GHz.

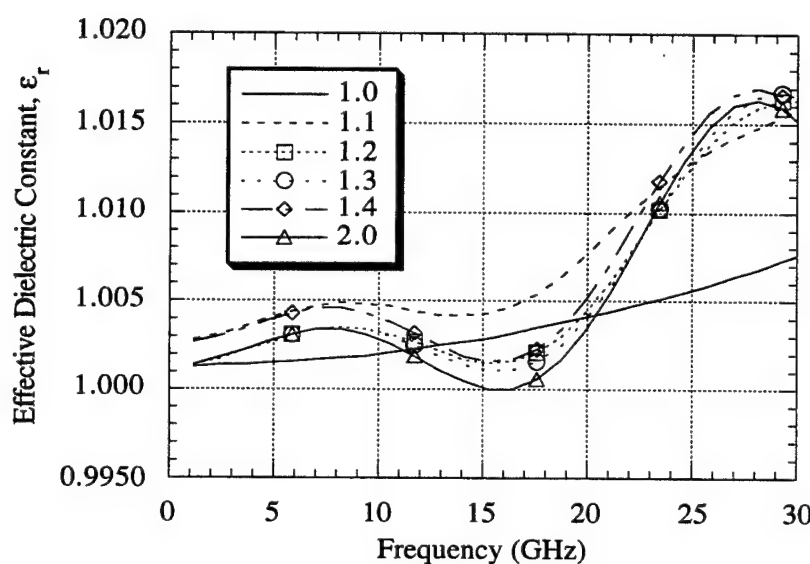


Figure 2.6 Effective dielectric constant as a function of frequency for the air-filled stripline of Fig. 2.5. The growth rate varies as indicated in the legend, and the mesh grows near the second monitoring point, "d+L."

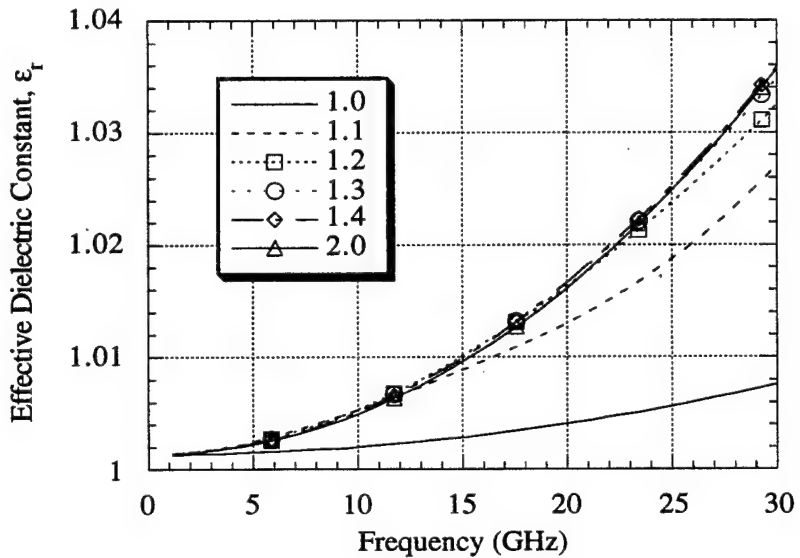


Figure 2.7 Effective dielectric constant as a function of frequency for the air-filled stripline of Fig. 2.5. The growth rate varies as indicated in the legend, and the mesh grows near the first monitoring point, "d."

2.5 Finline Waveguide

The finline waveguide became popular in the late 1970s with the increased interest in millimeter-wave integrated circuits [2.6]. The finline structure is shown in Fig. 2.8. It can be viewed as a shielded slotline, a ridged waveguide with dielectric, or a slab loaded waveguide with fins [2.7]. For millimeter-wave applications, the finline is preferred over the microstrip line because the finline does not require stringent manufacturing tolerances, is less susceptible to the propagation of higher-order modes, and interfaces well with waveguide instrumentation [2.6]. Several frequency domain techniques have been successfully applied to characterize the finline waveguide and related structures [2.7]-[2.11]. This type of problem is particularly well-suited to nonuniform orthogonal FDTD because of the thin dielectric slab which has to be modeled accurately. The mesh can grow as it moves away from the gap and toward the shield walls.

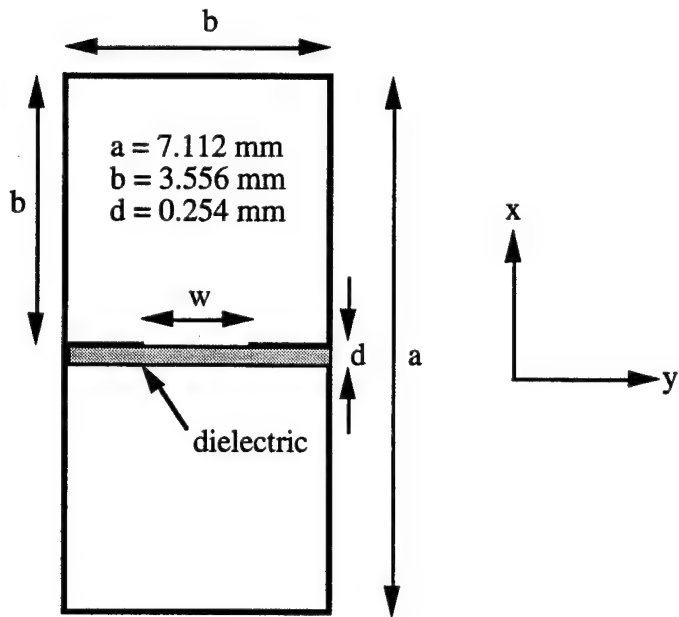


Figure 2.8 Geometry of the unilateral finline waveguide (with dielectric) and the symmetrical ridged waveguide (without dielectric).

In this section, the cutoff frequency of a symmetrical ridged waveguide with a varying aperture is calculated. The geometry being investigated is shown in Fig. 2.8, where the dielectric has a dielectric constant of one. The entire cross-section is excited with an impulse source, and the time signature of E_y is monitored at several locations. These time signatures are then Fourier transformed to the frequency domain, and a spike occurs at the cutoff frequency. The aperture width, w , was varied and is shown as a fraction of b , the length of the top wall of the waveguide, as shown in Fig. 2.8. Normalized cutoff frequencies calculated with the FDTD method are compared with results using the regular solution of the singular integral equation (RSSIE) method [2.11]. As shown in Fig. 2.9, the agreement between the two methods is very good.

After monitoring fields in the time domain and transforming to the frequency domain, the field distribution is readily available over a wide frequency band. Figure 2.10 shows the normalized distribution of E_y in the aperture of a unilateral finline waveguide with dielectric constant 2.22 at a frequency of 30 GHz for two different aperture widths. Again, the entire cross-section is excited with an impulse and the time

signatures are monitored in the aperture and then transformed to the frequency domain. These results compare well with aperture distributions calculated using the spectral domain method.

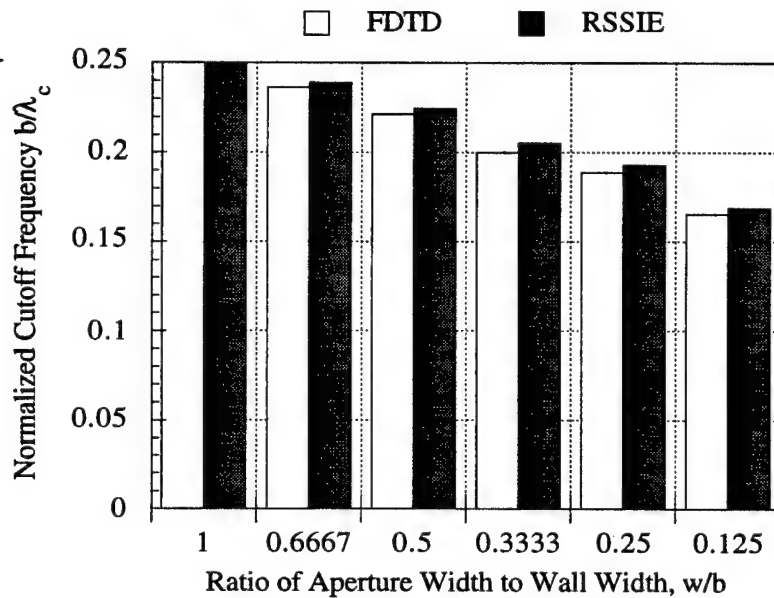


Figure 2.9 Normalized cutoff frequency of symmetrical ridged waveguide computed using FDTD and RSSIE.

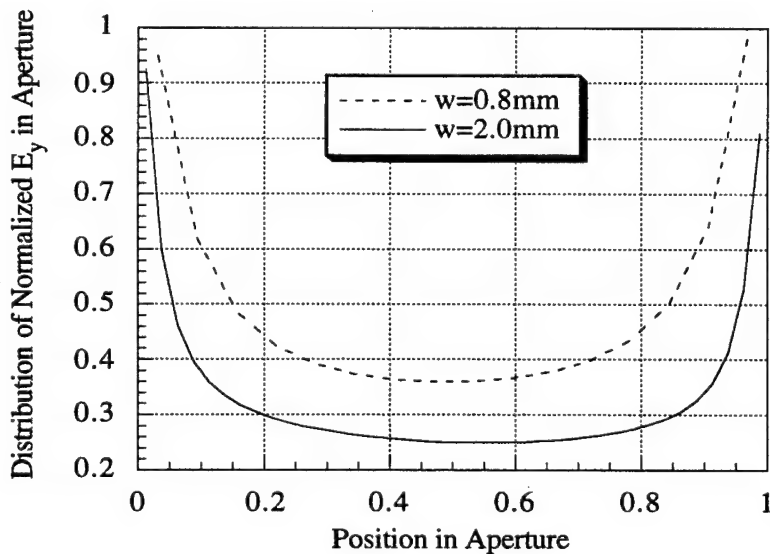


Figure 2.10 Distribution of normalized E_y in aperture of unilateral finline waveguide for two different aperture widths.

2.6 Lossy Layered Media

An application that is ideal for nonuniform FDTD is the analysis of fields in a lossy medium. The lossy medium considered in this section is seawater, which is assumed to have a constant conductivity of 4 S/m and $\epsilon_r = 72$. In sediment layer #1, $\sigma_1 = 2$ S/m and in sediment layer #2, $\sigma_2 = 1$ S/m. The geometry, shown in Fig. 2.11, is a 10 m long dipole oriented along the x-axis and excited with a Gaussian pulse that has a 3 dB cutoff frequency of 10 kHz. The dipole is centered in a volume that is 200 m by 100 m by 100 m. The problem is discretized with a mesh that has $\Delta x = 2$ m, $\Delta y = 1$ m, and $\Delta z = 1$ m near the dipole. The mesh discretization then expands away from the source, and is truncated with pec boundaries. The time step for FDTD simulations is determined by the Courant stability criterion as shown in (2.1). For this problem, the frequencies of interest are extremely low; thus, the time step would be restrictively small. Therefore, a different approach is taken for describing the medium and choosing the time step.

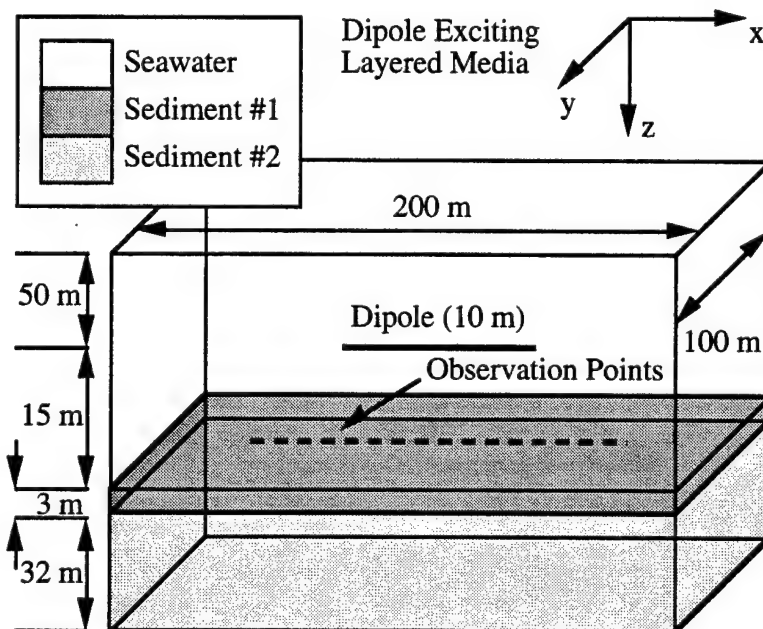


Figure 2.11 Geometry used for the analysis of fields in lossy layered media. The line of observation points is 14 m below the dipole source. The dipole source is centered in the computational volume.

Since $c = 1/\sqrt{\mu_0 \mu_r \epsilon_0 \epsilon_r}$, the time step, Δt , will increase if ϵ_r increases. The inequality $\omega \epsilon \ll \sigma$ must also be satisfied because seawater is a good conductor. Since the frequencies of interest are very low, ϵ_r can be increased to a value on the order of $1.0 \cdot 10^6$ without affecting the low frequency results [2.12]. This results in a much larger time step. The value of ϵ_r is chosen to be $4.0 \cdot 10^6$ and Δt is chosen to be $2.2 \mu\text{s}$. Electric and magnetic fields are monitored along a line parallel to the x-axis 14 m below the dipole source. The simulation is run for 6000 iterations, with field values recorded every ten iterations. The time signatures are converted to the frequency domain via the discrete Fourier transform (DFT).

When the entire background medium is seawater, an analytic expression for the fields exists. Nonuniform FDTD results are compared to analytic expressions in Figs. 2.12 - 2.14. The agreement is excellent.

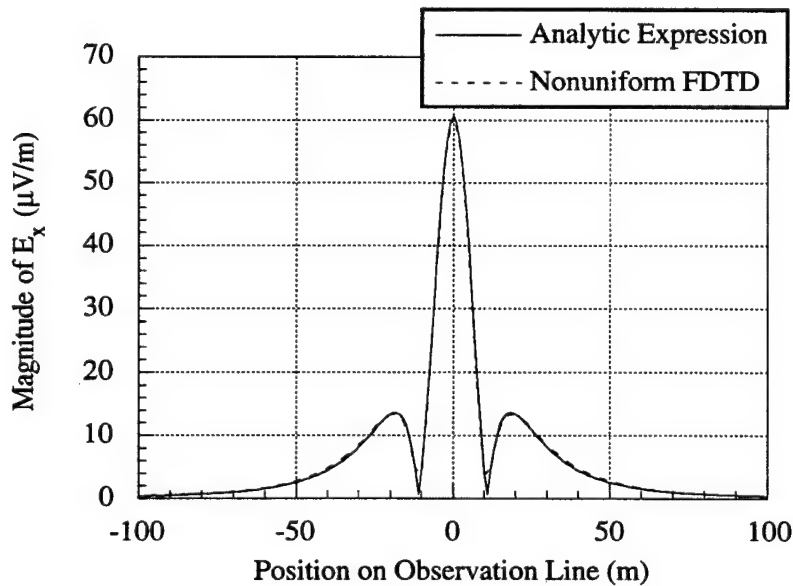


Figure 2.12 Magnitude of E_x in seawater observed 14 m below the source at $f = 1 \text{ Hz}$.

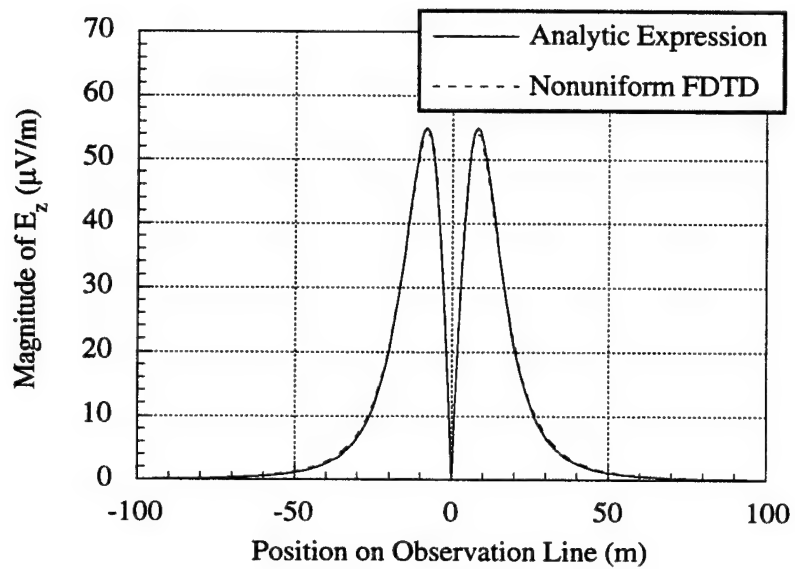


Figure 2.13 Magnitude of E_z in seawater observed 14 m below the source at $f = 1$ Hz.

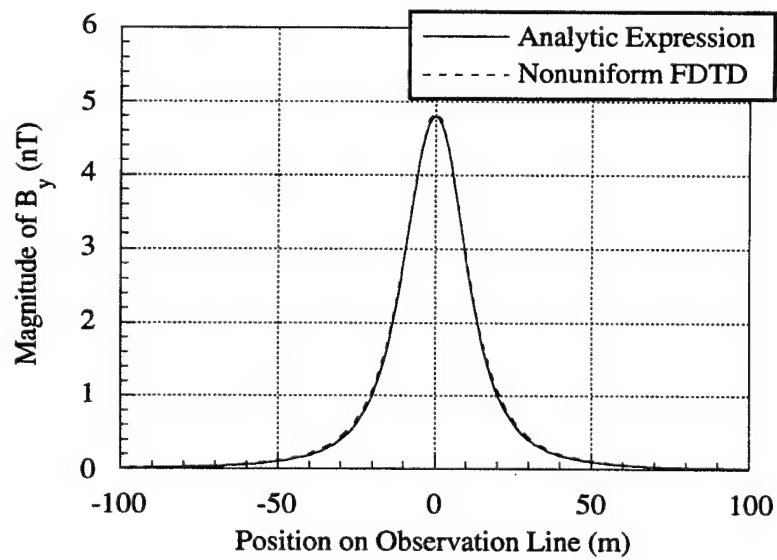


Figure 2.14 Magnitude of B_y in seawater observed 14 m below the source at $f = 1$ Hz.

When layers of sediment are present, as shown in Fig. 2.11, the FDTD results are compared to those for an integral equation method provided by the U.S. Navy [2.13]. Figures 2.15 - 2.17 show the nonuniform FDTD and Navy results, and again the agreement is excellent.

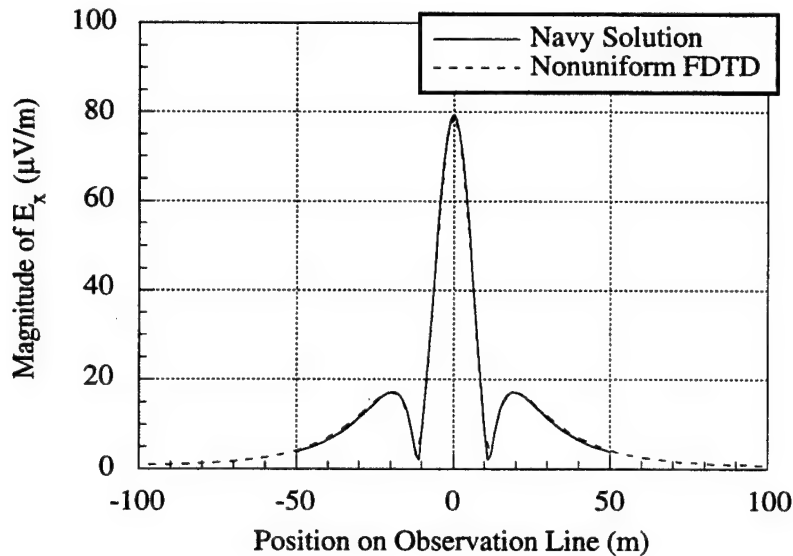


Figure 2.15 Magnitude of E_x in seawater with lossy layers observed 14 m below the source at $f = 1$ Hz.

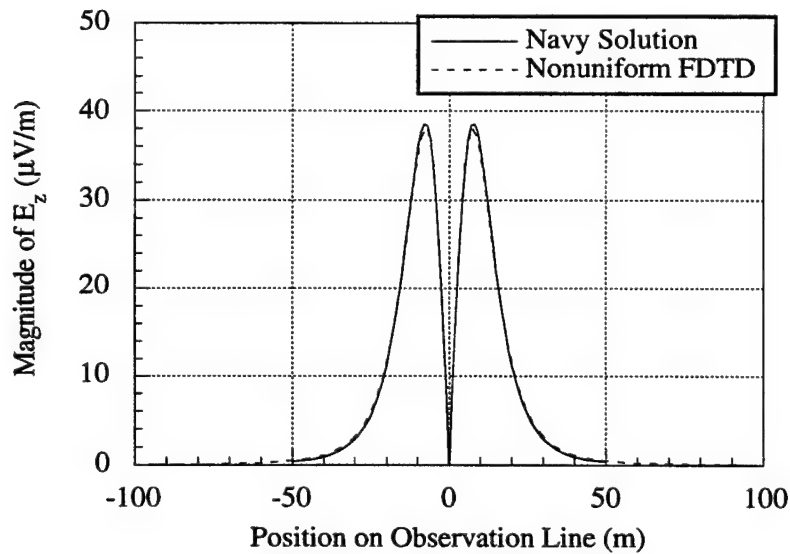


Figure 2.16 Magnitude of E_z in seawater with lossy layers observed 14 m below the source at $f = 1$ Hz.

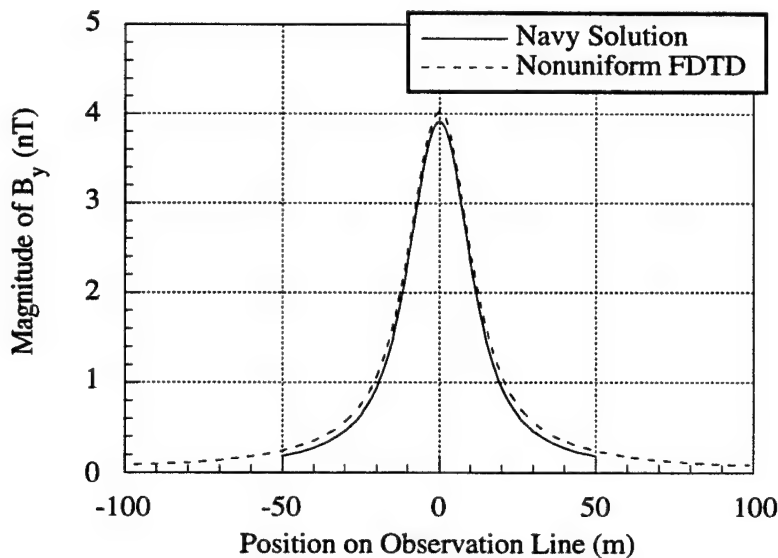


Figure 2.17 Magnitude of B_y in seawater with lossy layers observed 14 m below the source at $f = 1$ Hz.

Figure 2.18 shows the magnitude of the residual electric field, which is the absolute value of the difference between the fields in seawater alone and the fields with the layers of sediment present. The agreement between the results of the two methods is excellent.

The computational volume used for the FDTD simulations was 62 cells by 62 cells by 62 cells. When the same problem was solved using uniform FDTD, the computational volume was 100 cells by 100 cells by 100 cells. The nonuniform FDTD resulted in a 76% reduction of required memory. Moreover, the smaller number of unknowns also led to a shorter computation time. To further demonstrate the utility of the nonuniform mesh, the seawater problem was solved with a computational volume that was 39 cells by 39 cells by 39 cells. Field magnitudes are plotted in Figs. 2.19 - 2.21. Again the agreement is excellent. This FDTD simulation was nine times faster than the

62 by 62 by 62 case and gave a 75% memory savings. Relative to the 100 by 100 by 100 case, the 39 by 39 by 39 case represents a 94% savings in memory.

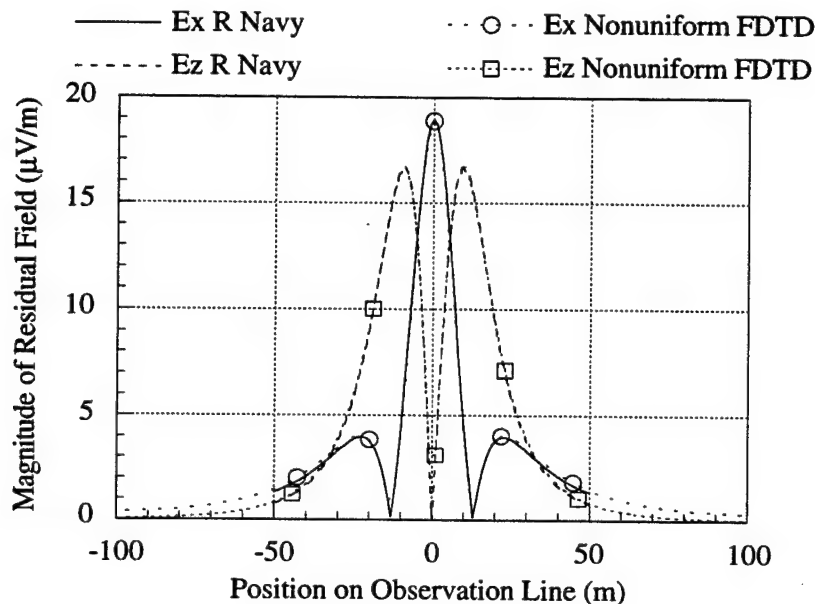


Figure 2.18 Comparison of FDTD results with integral equation results for the residual electric field observed 14 m below the source at $f = 1$ Hz.

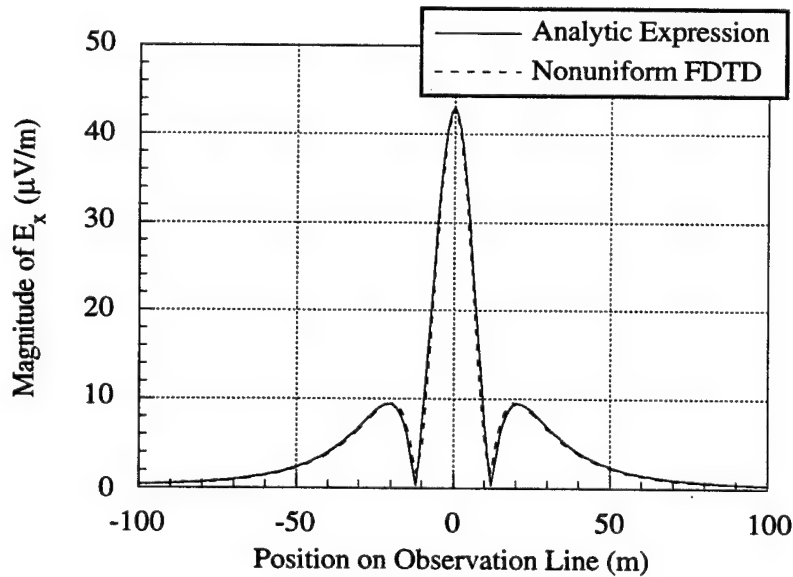


Figure 2.19 Magnitude of E_x in seawater observed 15.9 m below the source at $f = 1$ Hz.

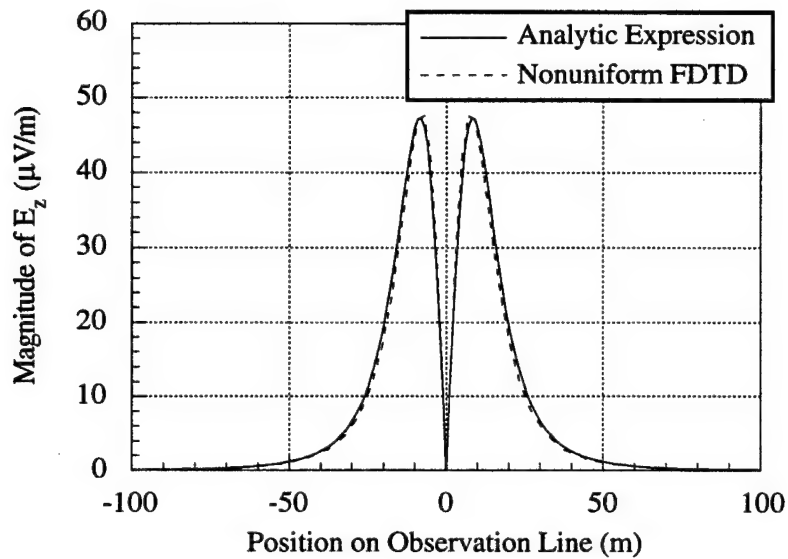


Figure 2.20 Magnitude of E_z in seawater observed 14.8 m below the source at $f = 1$ Hz.

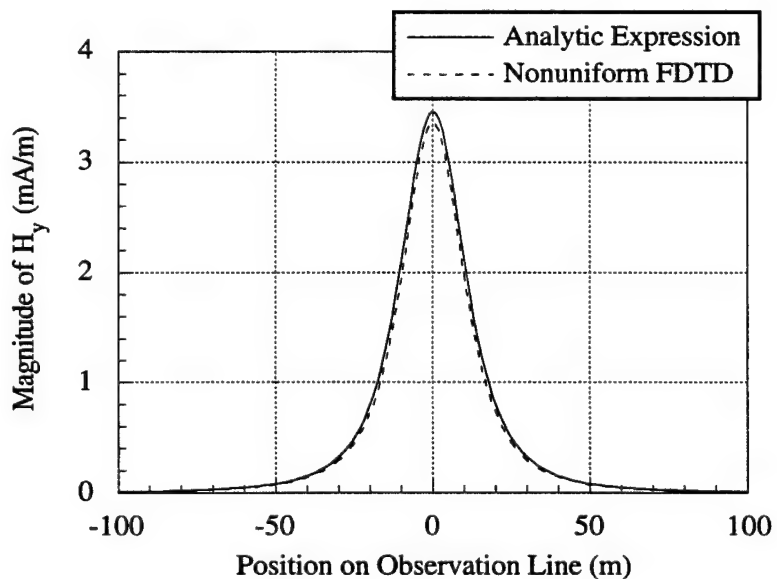


Figure 2.21 Magnitude of H_y in seawater observed 14.8 m below the source at $f = 1$ Hz.

The nonuniform FDTD method is very applicable to this type of problem because of the ability to let the mesh discretization grow. Moreover, a single FDTD simulation provides a wide band of frequency information, provided the geometry is excited with a transient source. This was the case here, although results are only shown for a single frequency. The nonuniform orthogonal FDTD approach is preferred over moment method type solutions for this problem because of the ability to vary the geometrical and electrical features of the problem without the derivation of a complicated Green's function. For example, it would be a simple matter to vary the surface of the sediment in a random fashion so as to model a rough surface, or to embed any kind of dielectric or metal slabs horizontally, or vertically, within the layers of sediment, or in the seawater.

2.7 Conclusions

This chapter described the uniform FDTD method and introduced the nonuniform orthogonal FDTD method. The nonuniform orthogonal FDTD method was developed from the general curvilinear FDTD method. The grid dispersion error due to the nonuniform mesh was analyzed, theoretically in terms of phase error per cell, and numerically in terms of accumulated phase error from the field propagating along a nonuniformly meshed stripline. It was demonstrated that the cell size in terms of wavelength as well as the growth rate of the mesh are critical in determining the amount of error, which can be maintained at acceptably low levels while still reducing memory requirements. Several example problems were presented which demonstrated the flexibility of the nonuniform FDTD method as well as the attractive features of memory savings and accurate fine feature modeling. In the case of the finline problem, small cell discretization was used to model the fine features of the geometry. In the case of the lossy layered media problem, the mesh grew rapidly from the regions of interest, which enabled the boundaries of the computational domain to be positioned sufficiently far away from the source and layers of sediment. This was accomplished with a small

number of unknowns relative to the uniform method. The results presented were in excellent agreement with analytic and moment method techniques.

2.8 References

- [2.1] K. S. Yee, "Numerical solution of initial boundary value problems involving Maxwell's equations in isotropic media," *IEEE Trans. Antennas Propagat.*, vol. 14, pp. 302-307, May 1966.
- [2.2] P. H. Aoyagi, "On the efficient and accurate application of partial differential equation solvers of Maxwell's equations in the time domain," Ph.D. dissertation, University of Illinois at Urbana-Champaign, 1992.
- [2.3] R. Holland, "Finite difference solution of Maxwell's equations in generalized nonorthogonal coordinates," *IEEE Trans. Nuc. Sci.*, vol. 30, no. 6, pp. 4589-4591, December 1983.
- [2.4] D. L. Paul, N. M. Pothecary, and C. J. Railton, "Calculation of the dispersive characteristics of open dielectric structures by the finite-difference time-domain method," *IEEE Trans. Microwave Theory Tech.*, vol. 42, no. 7, pp. 1207-1212, July 1994.
- [2.5] W. C. Chew, *Waves and Fields in Inhomogeneous Media*. New York: Van Nostrand Reinhold, 1990.
- [2.6] P. J. Meier, "Integrated fin-line millimeter components," *IEEE Trans. Microwave Theory Tech.*, vol. 22, pp. 1209-1216, December 1974.
- [2.7] J. B. Knorr and P. M. Shayda, "Millimeter-wave fin-line characteristics," *IEEE Trans. Microwave Theory Tech.*, vol. 28, pp. 737-743, July 1980.
- [2.8] T. Itoh and R. Mittra, "Dispersion characteristics of slot lines," *Electron. Lett.*, vol. 7, pp. 364-365, July 1971.
- [2.9] T. Itoh and R. Mittra, "Spectral-domain approach for calculating the dispersion characteristics of microstrip lines," *IEEE Trans. Microwave Theory Tech.*, vol. 21, pp. 496-499, July 1973.
- [2.10] T. Itoh and R. Mittra, "A technique for computing dispersion characteristics of shielded microstrip lines," *IEEE Trans. Microwave Theory Tech.*, vol. 22, pp. 896-898, October 1974.
- [2.11] Y.-F. Huang and S.-L. Lai, "Regular solution of shielded planar transmission lines," *IEEE Trans. Microwave Theory Tech.*, vol. 42, no. 1, pp. 84-91, January 1994.
- [2.12] P. H. Harms (private communication), March 1994.
- [2.13] R. Mittra (private communication), April 1994.

CHAPTER 3

THE DISPERSIVE ABSORBING BOUNDARY CONDITION APPLIED TO NONUNIFORM ORTHOGONAL MESHES

3.1 Introduction

One of the most important issues in electromagnetic modeling using the finite difference time domain method is the truncation of the computational domain with absorbing boundaries. Considerable efforts have been directed to the development, analysis, and improvement of absorbing boundary conditions (ABCs) [3.1]-[3.15]. An underlying theme common to research concerning ABCs is that it is desirable to use an ABC which is not only accurate in the modeling of waves at the boundaries, but also can be brought close to the radiating source or discontinuity, thereby saving on the memory and computation requirements. Depending upon the problem being solved, the absorbing boundary should simulate the outward propagation of travelling waves at various angles of incidence, guided modes, or evanescent modes. Clearly, it is advantageous to have a robust absorbing boundary condition that can be used for different types of problems, i.e., guided wave or radiating wave. The modified dispersive absorbing boundary condition is such an ABC [3.6].

The purpose of this chapter is to present the implementation of the dispersive boundary condition (DBC) on a nonuniform orthogonal grid. Motivation for the study of the DBC is presented with an analysis of the Mur ABCs. The DBC and modified DBC equations are derived, followed by a discussion on stability. The DBC for uniform grids is numerically tested with a microstrip line problem. Finally, the DBC for nonuniform grids is tested with a microstrip line problem and a general radiating problem. Error analysis is carried out in the time domain, the frequency domain, and spatially.

3.2 The Mur Absorbing Boundary Conditions

It is worthwhile to examine the limitations of the first- and second-order Mur absorbing boundary conditions [3.1]. Not only does this motivate the study of the dispersive boundary condition (DBC), but it also provides some insight regarding the performance of the DBC.

The well-known first-order Mur ABC is given in Equation (3.1).

$$\left(\frac{\partial}{\partial x} - \frac{1}{c} \frac{\partial}{\partial t} \right) E|_{x=0} = 0 \quad (3.1)$$

This ABC is unconditionally stable, straightforward to implement, and has minimal memory requirements. It can be used for radiating problems as well as for guided wave problems. The main drawback of the first-order Mur is that it only absorbs waves that are normally incident with velocity c . Additionally, higher-order ABCs are usually preferred over the first-order Mur because the reflections from the first-order Mur, which are typically on the order of 3 to 4% of the field incident on the boundary, can seriously degrade frequency domain results.

The second-order Mur ABC is given in Equation (3.2).

$$\left(\frac{1}{c} \frac{\partial^2}{\partial x \partial t} - \frac{1}{c^2} \frac{\partial^2}{\partial t^2} + \frac{1}{2} \left(\frac{\partial^2}{\partial y^2} + \frac{\partial^2}{\partial z^2} \right) \right) E|_{x=0} = 0 \quad (3.2)$$

The second-order Mur requires tangential derivatives on the boundary. Obviously, this leads to problems on the corners of the computational domain since there is not enough information to perform the derivative. Thus, additional corner conditions must be implemented. A more serious concern is the inability of the second-order Mur to absorb guided waves, for example, waves traveling on a microstrip line. This phenomenon can be explained by considering the dispersion relation and the Mur operator.

The dispersion relation is given in Equation (3.3)

$$k_x^2 + k_y^2 + k_z^2 = k^2 = \frac{\omega^2}{c^2} \quad (3.3)$$

where

$$k_x = k \sin(\theta) \cos(\phi) \quad (3.4)$$

$$k_y = k \sin(\theta) \sin(\phi) \quad (3.5)$$

$$k_z = k \cos(\theta) \quad (3.6)$$

are the Cartesian components of the propagation vector, θ is measured from the z-axis and ϕ is in the x-y plane referenced from the x-axis. In order to study the simulation of waves propagating outward in the z-direction, the dispersion relation is rewritten in terms of k_z , as follows:

$$k_z = \sqrt{k^2 - k_x^2 - k_y^2} \quad (3.7)$$

Simplifying Equation (3.7) gives

$$k_z = \sqrt{1 - \sin^2(\theta)} \quad (3.8)$$

It is the approximation of the square root in Equation (3.8) that determines the order of the Mur operator. The radical is expanded in a series using the small argument approximation, thus limiting the angle of incidence θ to small values, and the number of terms kept in the series yields the order of the Mur operator. The first-order Mur keeps one term, leading to a simple expression for k_z .

$$k_z \approx k \quad (3.9)$$

The second-order Mur keeps two terms and gives the following approximation for k_z :

$$k_z \approx k \left(1 - \frac{1}{2} \sin^2(\theta) \right) \quad (3.10)$$

Recall that the goal is to absorb a guided wave normally incident on a z-plane boundary. A guided wave traveling in a dielectric medium will travel with a velocity slower than the speed of light in free space, $v_z < c_o$. Since v_z and k_z are inversely related, a decrease in v_z means an increase in k_z . Thus, k_z should be greater than k . This is impossible, given Equation (3.10), and explains the inability of the second-order Mur to absorb guided waves. This serious limitation is not a problem for the dispersive boundary condition.

3.3 Dispersive Boundary Condition

The dispersive boundary condition analyzed in this work is of the same form as the absorbing boundary condition developed by Higdon, [3.3] and [3.4]. The Higdon absorbing boundary condition was developed for radiating problems, and the parameters of the ABC that can be varied are the speeds of the incident waves divided by the angles of incidence, $c/\cos(\theta)$. This same boundary condition can be used for guided wave problems if one interprets the wave speeds as normal velocities and modifies them accordingly [3.5]. The dispersive boundary condition (DBC) is written as follows:

$$\left(\frac{\partial}{\partial z} + \frac{1}{v_1} \frac{\partial}{\partial t} \right) \left(\frac{\partial}{\partial z} + \frac{1}{v_2} \frac{\partial}{\partial t} \right) E|_{z=z_{\max}} = 0 \quad (3.11)$$

The DBC has the form of the product of two first-order Mur operators. The differencing of this expression is straightforward and results in the following update equation on a uniform grid:

$$\begin{aligned} E_M^n = & 2E_{M-1}^{n-1} - E_{M-2}^{n-2} + (\gamma_1 + \gamma_2)(E_M^{n-1} - E_{M-1}^n - E_{M-1}^{n-2} + E_{M-2}^{n-1}) \\ & - \gamma_1 \gamma_2 (E_M^{n-2} - 2E_{M-1}^{n-1} + E_{M-2}^n) \end{aligned} \quad (3.12)$$

where the superscripts represent the indexing in time, the subscripts represent the indexing in space, and

$$\gamma_i = \frac{\Delta z - v_i \Delta t}{\Delta z + v_i \Delta t} \quad (3.13)$$

When the operator (3.11) is discretized on a nonuniform grid, the order in which the operators are applied has an effect on the resulting update equation for the boundary. Applying the operator with the v_1 term first yields the update equation

$$\begin{aligned} E_M^n = & 2E_{M-1}^{n-1} - E_{M-2}^{n-2} + (\gamma_{11} + \gamma_{12})(E_M^{n-1} - E_{M-1}^n) + (\gamma_{11} + \gamma_{22})(E_{M-2}^{n-1} - E_{M-1}^{n-2}) \\ & - \gamma_{11} \gamma_{12} (E_M^{n-2} - E_{M-1}^{n-1}) - \gamma_{11} \gamma_{22} (E_{M-2}^n - E_{M-1}^{n-1}) \end{aligned} \quad (3.14)$$

$$\gamma_{ij} = \frac{\Delta z_i - v_j \Delta t}{\Delta z_i + v_j \Delta t} \quad (3.15)$$

where Δz_1 is the discretization for the cell closest to the boundary. Applying the operator with v_2 first results in

$$\begin{aligned} E_M^n = & 2E_{M-1}^{n-1} - E_{M-2}^{n-2} + (\gamma_{11} + \gamma_{12})(E_M^{n-1} - E_{M-1}^n) + (\gamma_{12} + \gamma_{21})(E_{M-2}^{n-1} - E_{M-1}^{n-2}) \\ & - \gamma_{11}\gamma_{12}(E_M^{n-2} - E_{M-1}^{n-1}) - \gamma_{12}\gamma_{21}(E_{M-2}^n - E_{M-1}^{n-1}) \end{aligned} \quad (3.16)$$

These equations differ only in the second and fourth multipliers. Since it is not obvious which equation should perform better, a third equation was written which averages the second and fourth multipliers from Equations (3.14) and (3.16).

$$\begin{aligned} E_M^n = & 2E_{M-1}^{n-1} - E_{M-2}^{n-2} + (\gamma_{11} + \gamma_{12})(E_M^{n-1} - E_{M-1}^n) - \gamma_{11}\gamma_{12}(E_M^{n-2} - E_{M-1}^{n-1}) \\ & + \left(\frac{\gamma_{11} + \gamma_{22} + \gamma_{12} + \gamma_{21}}{2} \right) (E_{M-2}^{n-1} - E_{M-1}^{n-2}) \\ & - \left(\frac{\gamma_{11}\gamma_{22} + \gamma_{12}\gamma_{21}}{2} \right) (E_M^{n-2} - E_{M-1}^{n-1}) \end{aligned} \quad (3.17)$$

Since the multipliers are precomputed, each of these update equations requires only nine additions and five multiplications.

Numerical examples testing the performance of these equations follow in Sections 3.7 and 3.8.

3.4 The Modified Dispersive Boundary Condition

Betz and Mittra [3.6] introduced a damping factor into one of the operators of the DBC in order to improve the dc offset problem encountered in his research. Additionally, the damping factor can be used in the absence of the time derivative to absorb evanescent waves. The damping factor also stabilizes the DBC as is reported in Section 3.5. In this section, the chief concern is the discretization of the modified dispersive boundary condition on a nonuniform grid.

$$\left(\frac{\partial}{\partial z} + \frac{1}{v_1} \frac{\partial}{\partial t} + \alpha \right) \left(\frac{\partial}{\partial z} + \frac{1}{v_2} \frac{\partial}{\partial t} \right) E|_{z=z_{\max}} = 0 \quad (3.18)$$

Since evanescent waves are not considered in this work, only one damping term is used.

Discretizing Equation (3.18), assuming that the operator with the damping factor is applied first, results in the following update equation

$$\begin{aligned} E_M^n = & E_{M-1}^{n-1} + \beta(E_{M-1}^{n-1} - E_{M-2}^{n-2}) + (\gamma_{11} + \gamma_{12})(E_M^{n-1} - E_{M-1}^n) \\ & + (\gamma_{11} + \beta\gamma_{22})(E_{M-2}^{n-1} - E_{M-1}^{n-2}) - \gamma_{11}\gamma_{12}(E_M^{n-2} - E_{M-1}^{n-1}) \\ & - \gamma_{11}\gamma_{22}(E_{M-2}^n - E_{M-1}^{n-1}) \end{aligned} \quad (3.19)$$

where the superscripts represent time, the subscripts represent space, and γ_{ij} is defined as in Equation (3.15). Following the approach taken in [3.7], the term β is defined as

$$\beta = \frac{\Delta z_1 + v_1 \Delta t}{\Delta z_1 + v_1 \Delta t(1 + \alpha \Delta z_1)} \quad (3.20)$$

This definition is obtained by applying the damping term α only to the term E_M^n . An alternative definition for β can be found by applying central differencing in space and time to each component of (3.18) when discretizing. Following this procedure leads to the definition in Equation (3.21).

$$\beta = \frac{\Delta z_1 + v_1 \Delta t(1 - \alpha \Delta z_1)}{\Delta z_1 + v_1 \Delta t(1 + \alpha \Delta z_1)} \quad (3.21)$$

There are three parameters that can be varied in Equation (3.18). The effects of these parameters, as well as the definitions in Equations (3.20) and (3.21), on the performance of the DBC will be presented in Sections 3.5 - 3.8.

3.5 Stability

It has been reported that stability problems sometimes arise when using second-order and higher-order dispersive boundary conditions [3.7], i.e., the ABC is not always reliable. The results of this work also confirm this. Various explanations are given for the stability problem. One explanation states that the generation of spurious dc signals depends on subtle factors such as the exact order of the additions in the update equations, the spatial distribution of the incident field, and the other boundary conditions truncating the mesh [3.8]. A rigorous approach to the stability issue has been reported

regarding the stability of Liao's ABC [3.9]. In [3.9] it has been shown that one of the poles of the reflection coefficient due to the ABC is on the unit circle in the complex k -plane, rendering the ABC marginally unstable. It is demonstrated that perturbing one of the multipliers in the differencing scheme for the Liao ABC has drastic effects on the stability of the ABC. Since the DBC and Liao's ABC are both of the same form as the Higdon ABC, this analysis can also be applied to the DBC. Moreover, it is stated that perturbing the multiplier in order to stabilize the Liao ABC is equivalent to adding a damping factor to the DBC. This will be demonstrated via a numerical example.

The mesh used to test the stability of the DBC was 40 by 40 by 41 cells, and was discretized with $\Delta x = \Delta y = \Delta z = 3.750$ mm. The center of the mesh was excited with a z-directed point source with the following time variation:

$$y(t) = \frac{T \exp(2)}{16} \frac{d}{dt} \left[\left(\frac{t}{T} \right)^4 \exp\left(\frac{-t}{T}\right) \right] \quad (3.22)$$

where

$$T = \frac{0.152}{f_c} \quad (3.23)$$

where f_c was chosen to be 1.75 GHz and Δt was chosen to be 6.25 ps. The z-component of the electric field was monitored 15 cells from the source in the y-direction for time step 0 to time step 10000.

Four different ABCs were used in this stability test, a first-order Mur, and three DBCs with δ equal to 0.00, 0.05, and 0.10, where δ is defined in Equation (3.24).

$$\delta = \alpha \Delta z \quad (3.24)$$

The z-component of the electric field for time steps 0 to 500 is shown in Fig. 3.1. Clearly, the second-order DBC does a much better job of absorbing the incident pulse than the first-order Mur. Figure 3.2 shows the electric field as a function of time for time steps 1500 to 2500. Note that the electric field due to the DBC without the damping term is growing, while the Mur and the damped DBC remain stable.

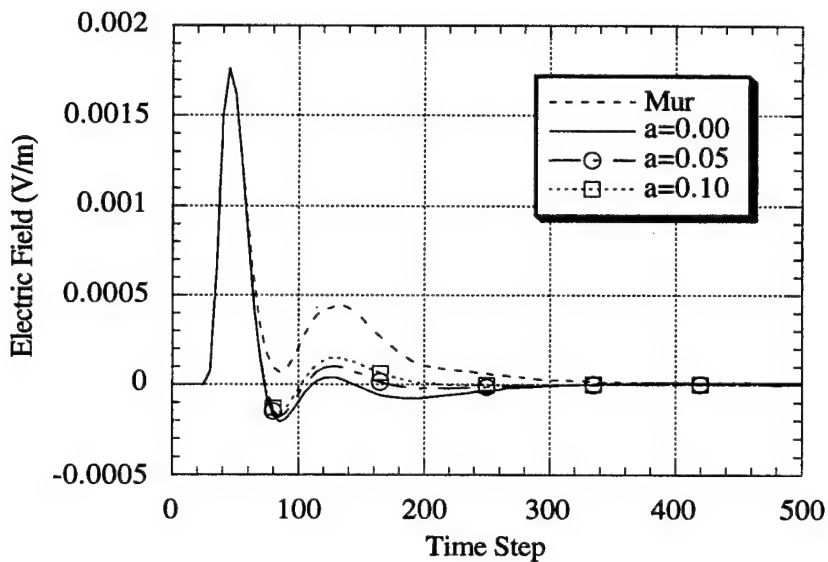


Figure 3.1 Electric field response near boundary for first-order Mur ABC and DBC with $a = \delta$, for $\delta = 0$, $\delta = 0.05$, and $\delta = 0.10$.

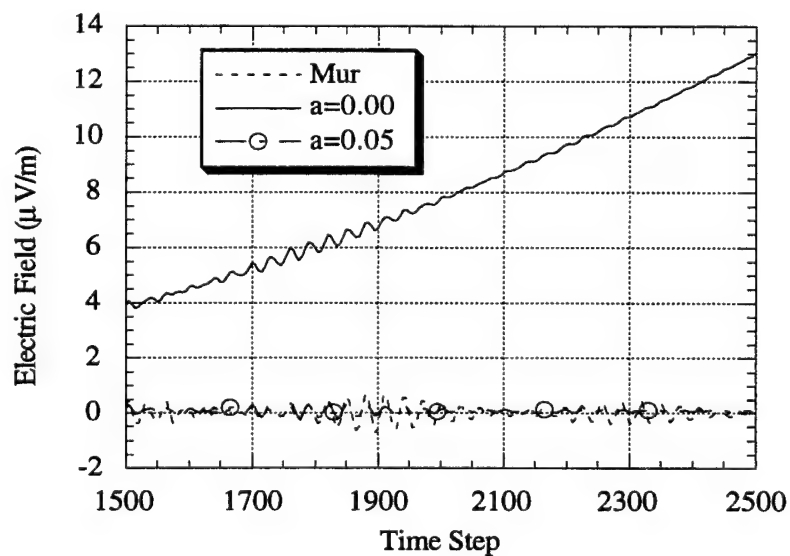


Figure 3.2 Electric field response near boundary for first-order Mur ABC and DBC with $a = \delta$, for $\delta = 0$ (unstable) and $\delta = 0.05$ (stable).

Figure 3.3 demonstrates the stability of the damped DBC, showing the electric field from time step 0 to time step 10000. Finally, Fig. 3.4 shows that there is a slight dc offset when the value of δ is not large enough. However, when $\delta = 0.10$, there is no undesirable dc offset and the ABC is stable.

The same test was performed on a nonuniform mesh, and the DBC was found to be stable without the addition of a damping term. Figure 3.5 shows the electric field 5 cells from the boundary as a function of time for the DBC with δ equal to zero and δ equal to 0.10. Although the DBC does not become unstable, there is a slight dc offset without the damping term, as shown in Fig. 3.6. The addition of the damping term eliminates the dc offset as in the uniform case.

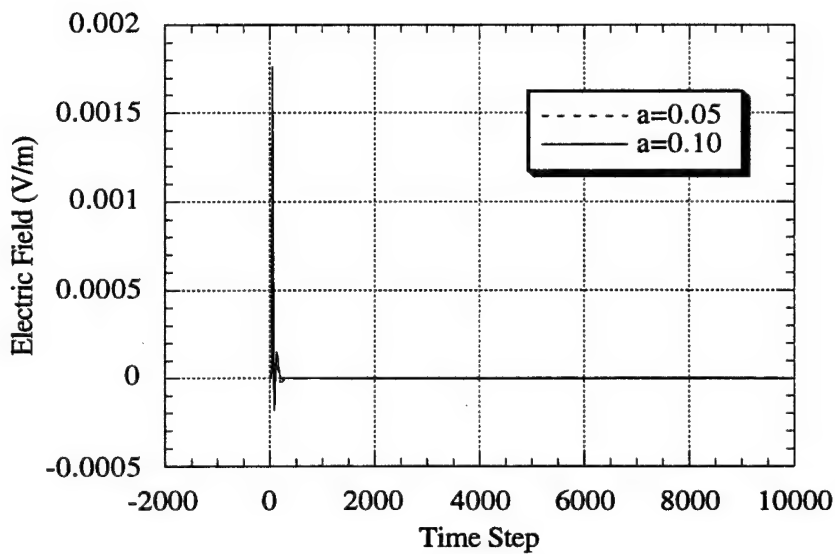


Figure 3.3 Electric field response near the boundary for the DBC with $a = \delta$, for $\delta = 0.05$ and $\delta = 0.10$. The damping term stabilizes the DBC.

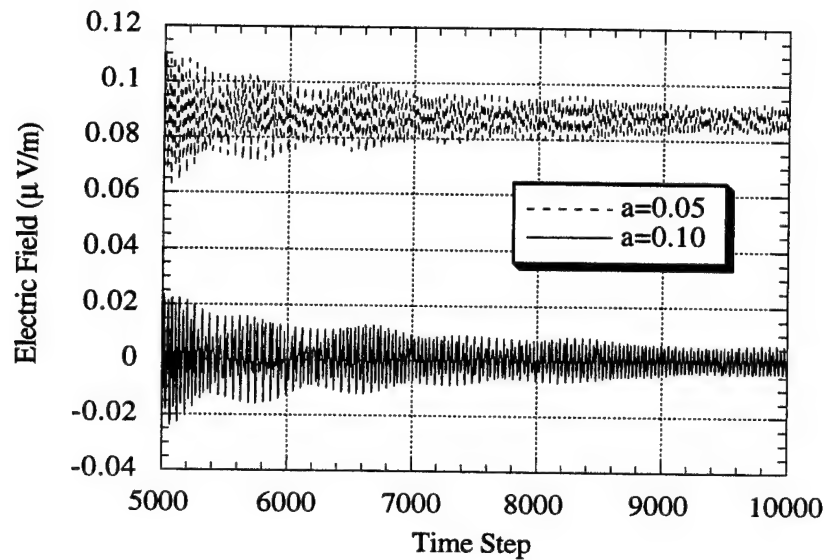


Figure 3.4 Electric field response near the boundary for the DBC with $a = \delta$, for $\delta = 0.05$ and $\delta = 0.10$. The larger damping term eliminates the dc offset.

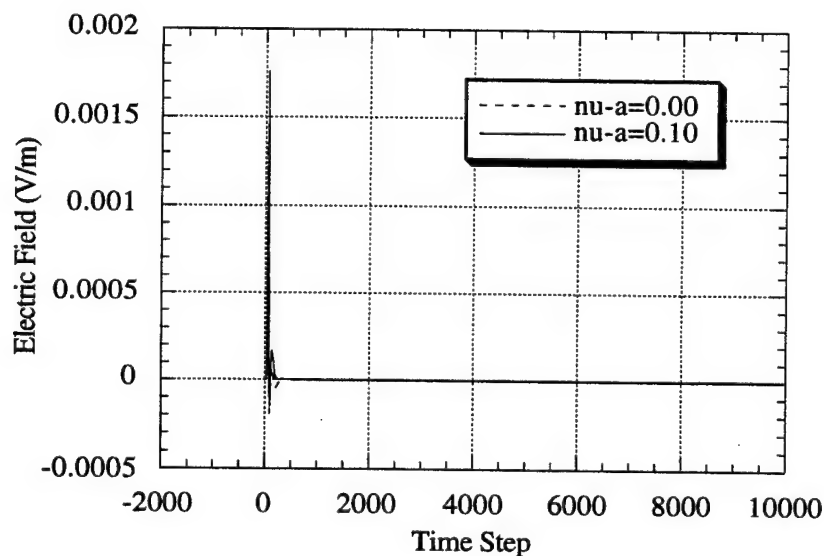


Figure 3.5 Electric field response near the boundary for the DBC on a nonuniform grid with $a = \delta$, for $\delta = 0.00$ and $\delta = 0.10$. Both cases are stable.

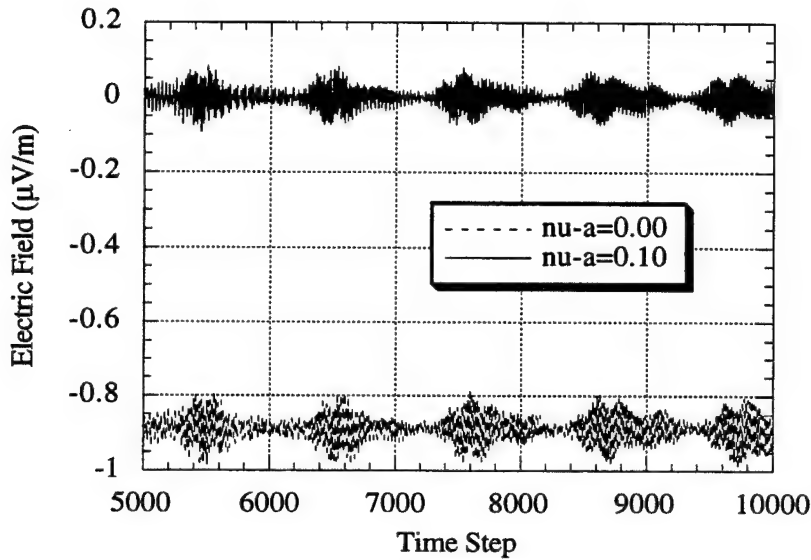


Figure 3.6 Electric field response near the boundary for the DBC on a nonuniform grid with $a = \delta$, for $\delta = 0.00$ and $\delta = 0.10$. The damping term eliminates the dc offset.

3.6 Microstrip Line with Uniform Mesh

In this section, the dispersive boundary condition (DBC) is tested on a microstrip line. The width of the line is equal to the thickness of the dielectric substrate, which is 2.54 mm, as shown in Fig. 3.7. The dielectric constant of the substrate is 10.2. The DBC is used to truncate the end walls of the microstrip line, the bottom wall is a perfect electric conductor, and the side and top walls are truncated with the first-order Mur ABC. The mesh is discretized with $\Delta x = \Delta y = \Delta z = 0.3715$ mm, and the time step Δt is 0.6053 ps, which is 0.99 times the limiting value from the Courant stability criterion. The structure is excited with a window function with a 3 dB cutoff frequency of 8 GHz. To test the effectiveness of the DBC, the problem is run with two meshes. The test mesh is 24 by 44 by 270 and the larger reference mesh is 24 by 44 by 500. The voltage is monitored along the line as a function of time. The solution on the reference line is considered to be exact since the simulation is stopped before reflections from the far end of the line can reach

the point where the voltage is monitored and corrupt the signal. The difference between the reference solution and the test solution will show the effectiveness of the ABC being tested.

The normalized reflected voltage is plotted as a function of time in Fig. 3.8. The curve labeled "mur" is the result using a first-order Mur ABC on the test boundary. The ABC is implemented so that the speed of the wave is determined by the material property of the medium in a given cell. For example, cells in air are updated with the velocity of free space, whereas cells in the dielectric are updated with a velocity of $c / \sqrt{\epsilon_r}$. The peak of the normalized reflection in the time domain is around 0.025. The curve labeled "dbc0" is the result of setting $\delta = 0$, $\epsilon_{r1} = 7.12$, and $\epsilon_{r2} = 8.5$. For "dbc1", $\delta = 0.1$, $\epsilon_{r1} = 7.12$, and $\epsilon_{r2} = 8.5$, and for "dbc2", $\delta = 0.1$, $\epsilon_{r1} = 8.5$, and $\epsilon_{r2} = 7.12$. All three of the DBC results appear to be considerable improvements when compared with the Mur result.

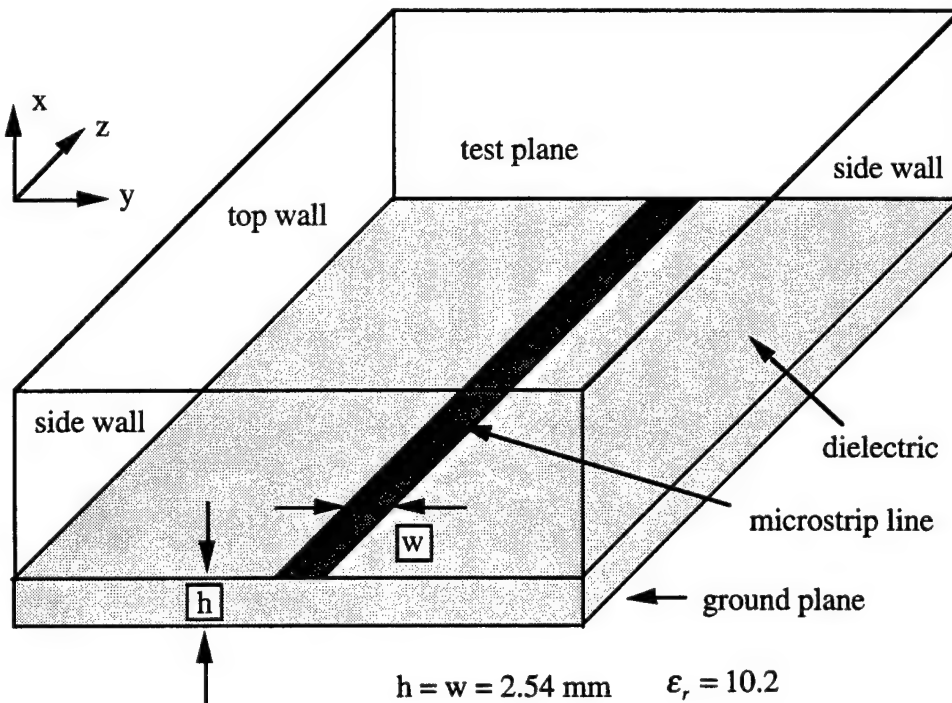


Figure 3.7 Geometry of the microstrip line used to test the DBC. The relevant dimensions are labeled in the figure.

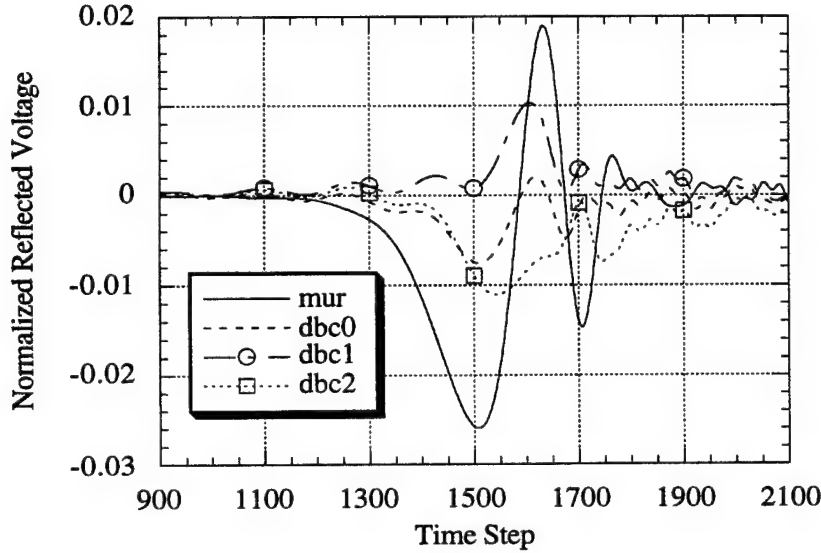


Figure 3.8 Normalized reflected voltage on the microstrip line as a function of time: "mur" is first-order Mur; "dbc0" has $\delta = 0$, $\epsilon_{r1} = 7.12$, and $\epsilon_{r2} = 8.5$; "dbc1" has $\delta = 0.1$, $\epsilon_{r1} = 7.12$, and $\epsilon_{r2} = 8.5$; "dbc2" has $\delta = 0.1$, $\epsilon_{r1} = 8.5$, and $\epsilon_{r2} = 7.12$.

Another useful way to ascertain the effectiveness of the ABCs under test is to define a reflection coefficient due to the ABC. The test voltage is subtracted from the reference voltage, giving the reflected voltage. The test voltage and reflected voltages are transformed to the frequency domain, and the reflection coefficient is then defined as the ratio of the reflected voltage to the incident voltage. The magnitude of the reflection coefficient is plotted as a function of frequency in Fig. 3.9, where it can be seen that the best performing ABC is the DBC with δ set to zero. Although this yields the best result, it can potentially lead to late time instabilities, as was demonstrated in Section 3.5. Since the δ term is applied in the first operator, the choice of ϵ_{r1} and ϵ_{r2} is significant. Clearly, it is best to choose the smaller ϵ_r value for ϵ_{r1} . This results in a reflection coefficient with magnitude less than 0.01 over the 1 GHz to 16 GHz range.

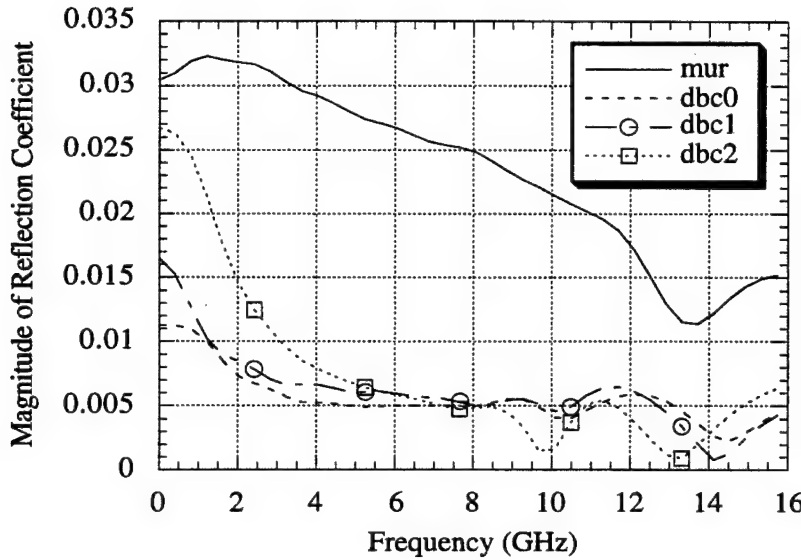


Figure 3.9 Magnitude of reflection coefficient as a function of frequency for the microstrip line. Curves are labeled as in Fig. 3.8.

The error due to the ABCs can also be quantified using error norms. Two different norms are used in this analysis, an L_1 norm and an L_2 norm. The norms are defined as follows:

$$L_m = \left(\sum_{i=1}^n |v_{r_i} - v_{t_i}|^m \right)^{\frac{1}{m}} \quad (3.25)$$

where v_{r_i} and v_{t_i} are the reference and test voltages, respectively. Error norms are listed in Table 3.1. The numerical data show the same trend as the graphical data presented.

Table 3.1 Error for DBC tested on microstrip line

DBC	δ	ϵ_{r1}	ϵ_{r2}	$L1 (*10^{-2})$	$L2 (*10^{-4})$
0	0.0	7.12	8.50	0.392367	1.765111
1	0.1	7.12	8.50	0.457797	2.068264
2	0.1	8.50	7.12	0.778930	3.206607
First-order Mur				1.429872	6.966470

3.7 Microstrip Line with Nonuniform Mesh

The effectiveness of the dispersive boundary condition (DBC) when applied to a uniform mesh was demonstrated in previous sections. In this section, the DBC is applied to a microstrip line with a nonuniform mesh. Again, two meshes are used to test the effectiveness of the DBC. The large reference mesh is 24 by 44 by 500 cells and the test mesh is 24 by 44 by 270 cells. The geometry is excited and the voltage monitored in the same manner as in the uniform case. In order to isolate the effects of the nonuniform mesh and nonuniform boundary condition, only the last four cells in the z-direction are nonuniform and the growth rate between neighboring cells is at most 1.20. Three parameters are varied when testing the performance of the DBC. These parameters are ϵ_{r_1} , ϵ_{r_2} , and δ , where δ is defined in Equation (3.24) and α appears with ϵ_{r_1} as shown in Equation (3.18).

Different values and combinations of ϵ_r and δ were tested, and time domain results are plotted in Figs. 3.10 - 3.12. In these figures, the difference between the reference voltage and test voltage is normalized by the maximum value of the reference voltage. The values of ϵ_{r_1} and ϵ_{r_2} are 7.12 and 8.5, respectively, for cases 0, 1, 3, and 4. For case 2, $\epsilon_{r_1} = 8.5$ and $\epsilon_{r_2} = 7.12$. The δ values for cases 0 through 4 are 0.0, 0.10, 0.10, 0.05, and 0.01, respectively. Figure 3.10 shows that case 0 produces less reflection than case 1. The result from the first-order Mur ABC is also provided in Fig. 3.10. The peak in the time domain reflection from the first-order Mur ABC is more than three times greater than the largest peak from the DBC. Figure 3.11 compares cases 2 through 4 and clearly shows that case 2 yields poor results. Comparing the results of Fig. 3.10 with the results in Fig. 3.11 shows that although the reflection from case 2 is large, it is still an improvement over the first-order Mur result. The time range is narrowed in Fig. 3.12 and the effect of varying δ is shown. The smaller values of δ produce smaller reflections in this time range.

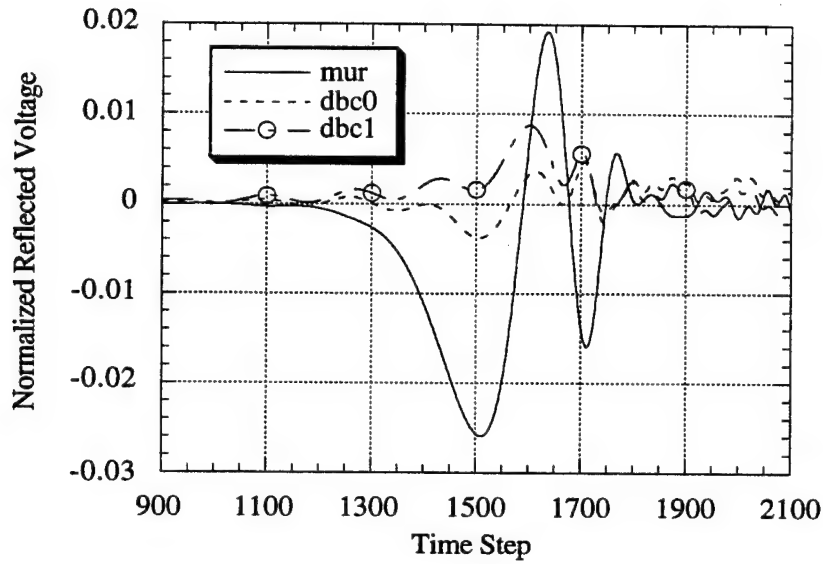


Figure 3.10 Normalized reflected voltage as a function of time for the microstrip line on a nonuniform grid. The first-order Mur result is labeled "mur," $\epsilon_{r1} = 7.12$, $\epsilon_{r2} = 8.5$, "dbc0" has $\delta = 0$, and "dbc1" has $\delta = 0.1$

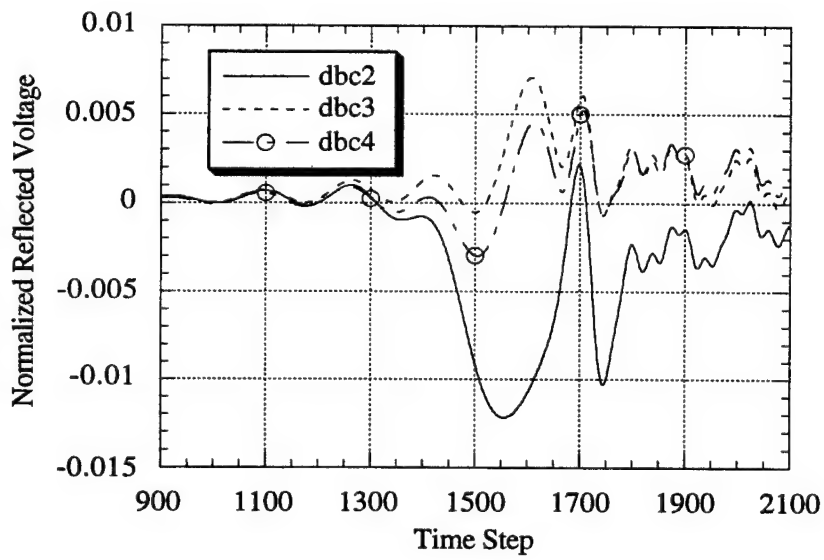


Figure 3.11 Normalized reflected voltage as a function of time for the microstrip line on a nonuniform grid. "dbc2" has $\delta = 0.1$, $\epsilon_{r1} = 8.5$, and $\epsilon_{r2} = 7.12$, "dbc3" has $\delta = 0.05$, $\epsilon_{r1} = 7.12$, and $\epsilon_{r2} = 8.5$, "dbc4" has $\delta = 0.01$, $\epsilon_{r1} = 7.12$, and $\epsilon_{r2} = 8.5$.

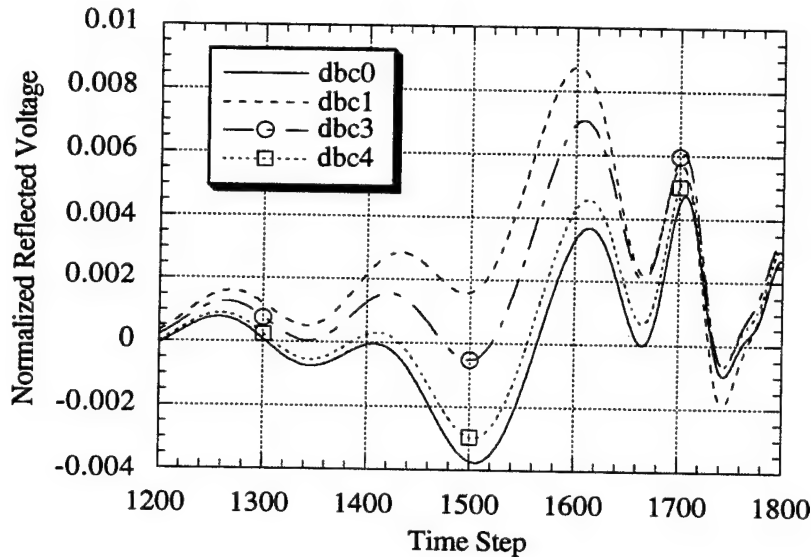


Figure 3.12 Normalized reflected voltage as a function of time for the microstrip line on a nonuniform grid. Curves labeled as in Figs. 3.10 and 3.11.

Frequency domain plots of the magnitude of the reflection coefficient are shown in Figs. 3.13 and 3.14. Figure 3.13 shows that when $\epsilon_{r_1} = 7.12$ and $\epsilon_{r_2} = 8.5$, the DBC outperforms the first-order Mur by a factor of around 5 or 6 in the frequency range of 4 GHz to 10 GHz. When $\epsilon_{r_1} = 8.5$, $\epsilon_{r_2} = 7.12$, and $\delta = 0.10$, the DBC is still much more effective than the first-order Mur, which is not obvious from examining the time domain results. Figure 3.14 compares the effects of varying δ . Again, the smaller δ produces smaller reflections.

As with the uniform mesh microstrip line test, the errors can be quantified with error norms. The numerical data presented in Table 3.2 show the same trends as the graphical data. To minimize the reflection from the absorbing boundary, the smaller value of the two dielectric constants should be used in the first operator, and the damping term should be small, but remain nonzero in order to prevent late-time instabilities.

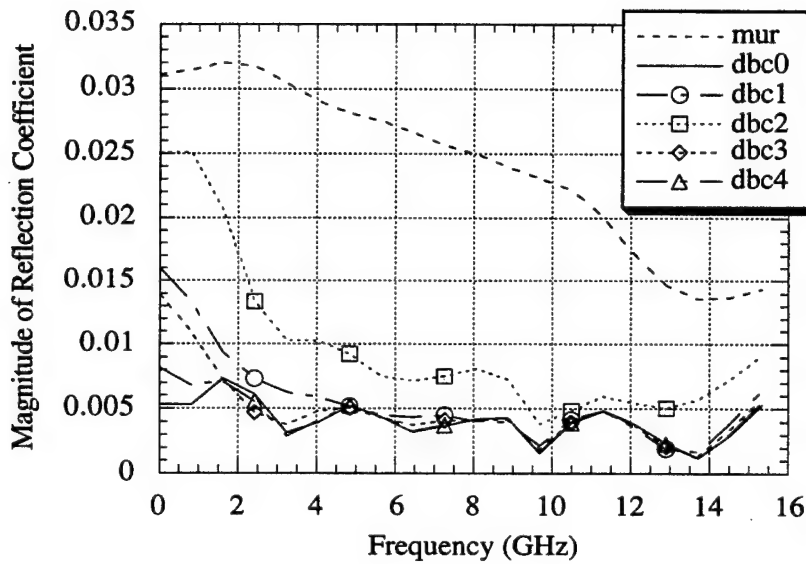


Figure 3.13 Magnitude of reflection coefficient as a function of frequency for the microstrip line on a nonuniform grid. Curves labeled as in Figs. 3.10 and 3.11.

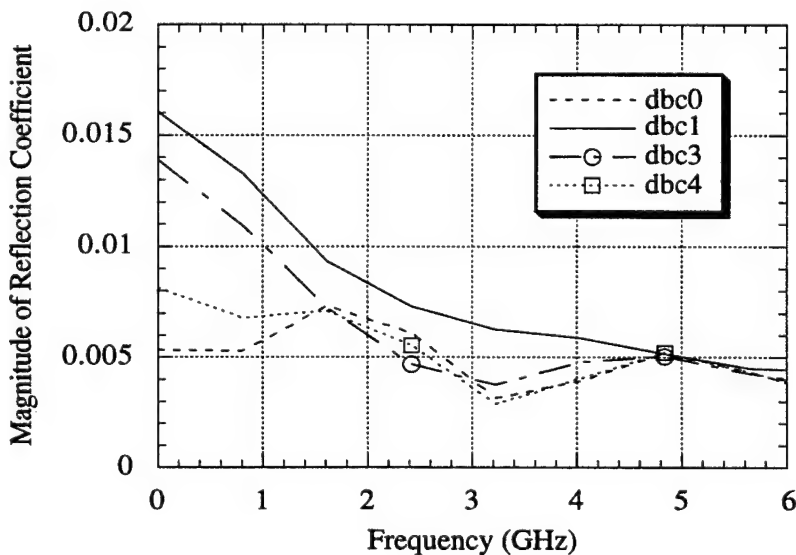


Figure 3.14 Magnitude of reflection coefficient as a function of frequency for the microstrip line on a nonuniform grid. Curves labeled as in Figs. 3.10 and 3.11.

Table 3.2 Error for DBC tested on microstrip line with nonuniform mesh

DBC	δ	ϵ_{r1}	ϵ_{r2}	L1 ($\times 10^{-2}$)	L2 ($\times 10^{-4}$)
0	0.00	7.12	8.50	0.452295	1.448510
1	0.10	7.12	8.50	0.491422	1.997053
2	0.10	8.50	7.12	0.814429	3.536524
3	0.05	7.12	8.50	0.431705	1.701391
4	0.01	7.12	8.50	0.453550	1.488936
First-order Mur				1.473694	7.053369

3.8 Angle Absorbing Boundary Condition

The form of the dispersive boundary condition (DBC) allows one to choose the velocity which will optimize the performance of the boundary condition for any given problem. This is important since it can then be used for both guided wave and radiating wave problems. When the DBC is used for a radiation problem, it will be referred to as the angle absorbing boundary condition (AABC).

In order to test the AABC, a simple point source radiating in free space was analyzed. A large mesh with 104 by 104 by 103 cells provided the reference solution and a smaller mesh with 54 by 54 by 53 cells was used to test the AABC. The majority of the test mesh is uniform with $\Delta x = \Delta y = \Delta z = 9.000$ mm. The outer four layers in each direction are nonuniform with a maximum growth rate of 1.2. The time step is chosen to be 15.625 ps and the center of the mesh is excited with the following z-directed source:

$$E_z(n) = A * (10 - 15\cos(\varphi) + 6\cos(2\varphi) - 3\cos(3\varphi)) \quad (3.26)$$

where $A = 1.0/320.0$, $\varphi = 2\pi f_r n \Delta t$, and $f_r = 1$ GHz. The source, shown in Fig. 3.15, is nonzero for 64 time steps.

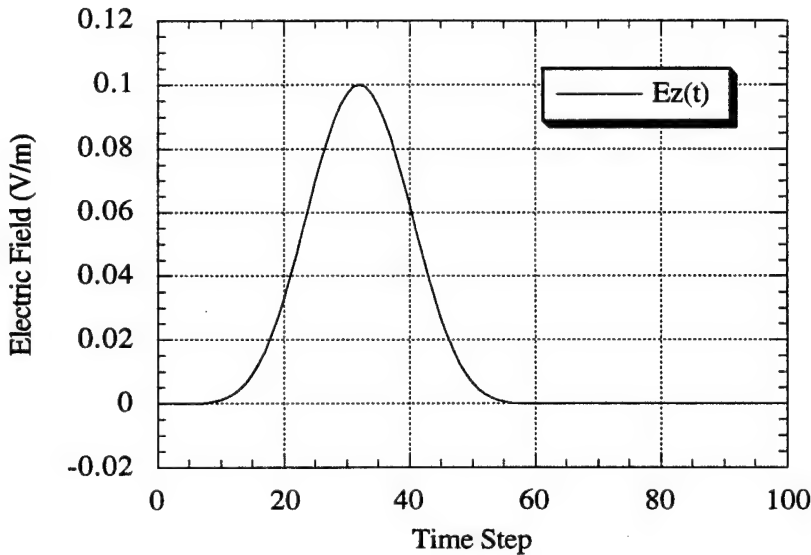


Figure 3.15 Time signature of the point source excitation used to test the angle absorbing boundary condition.

Error analysis is carried out as a function of time and position. The z-component of the electric field is monitored from time step 80 to time step 160 on the plane two cells from the $y = 0$ boundary. This allows the source pulse to pass through the boundary and shows the effect of the imperfect radiating boundary condition. When the error is shown as a function of time, the absolute value of the difference between the reference solution and the test solution is summed at each location on the test plane and normalized by the maximum value of the sum of the magnitudes of the field values in the reference solution in the time range of interest. The expression for the error is given in Equation (3.27)

$$Error(t) = \frac{\sum_{ij} |v_r(i, j, t) - v_t(i, j, t)|}{\max\left(\sum_{ij} |v_r(i, j, t)|\right)_{all, t}} \quad (3.27)$$

where v_r is the reference field value, v_t is the test field value, i and j are spatial indices, and t is the time index. When the error is presented as a function of position, the sum of the absolute value of the difference between the reference solution and the test solution

from time step 80 to time step 160 is normalized by the sum of the absolute value of the reference solution over that same time interval for a given position, as shown in Equation (3.28).

$$Error(p) = \frac{\sum_i |v_r(p, t) - v_i(p, t)|}{\sum_i |v_r(p, t)|} \quad (3.28)$$

where p is the position index. The position moves along a diagonal from the lower left corner to the center of the test plane. This corresponds to moving from position 0 to position 25 as shown in Fig. 3.16. A diagonal line was chosen in order to gauge the performance of the ABCs being tested as a function of position. This is important because the performance of ABCs in corners is of interest. Using monitoring locations along a diagonal gives a wider range of incident angles upon the boundary as opposed to a line parallel to one of the edges of the mesh.

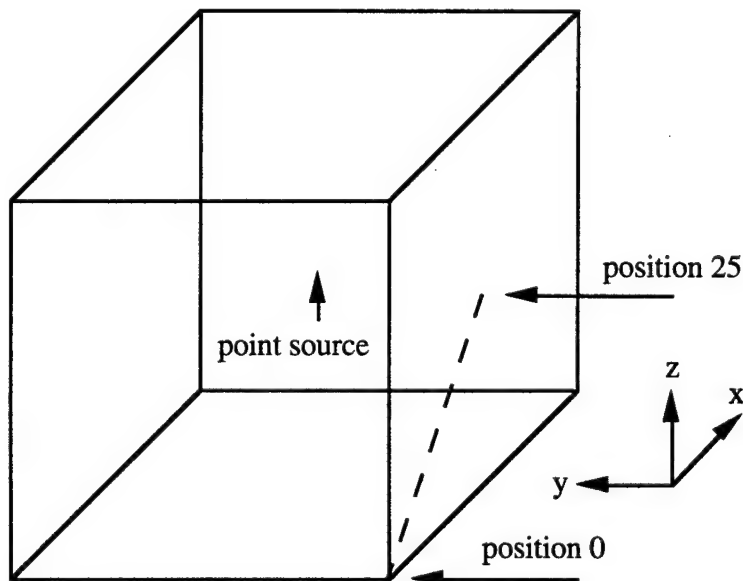


Figure 3.16 The geometry used to test the Angle Absorbing Boundary Condition is a point source radiating in free space. The fields are monitored on a line in the $y = 2$ plane.

As discussed previously, the order of the implementation of the operators does make a difference on the nonuniform grid, whether or not the damping term is present. The AABC was tested with no damping term using two different angles, one of which was always zero. For a given angle, there were three possible implementations. One with v_1 modified by the angle and v_2 equal to c , one with v_2 modified by the angle, and one with the multipliers determined by averaging the multipliers from the first two cases. The nonzero angles tested were 15° , 30° , and 45° . The results are compared with the first-order Mur.

Results for normalized error as a function of time are shown in Figs. 3.17 - 3.20. Figure 3.17 shows results in which the v_1 term is modified by the angle as shown on the plot legend and "mur" refers to the first-order Mur ABC. Figures 3.18 - 3.20 compare the errors obtained using the three different implementations of the AABC for a given angle. The best results are achieved when v_1 is modified by a 45 degree angle.

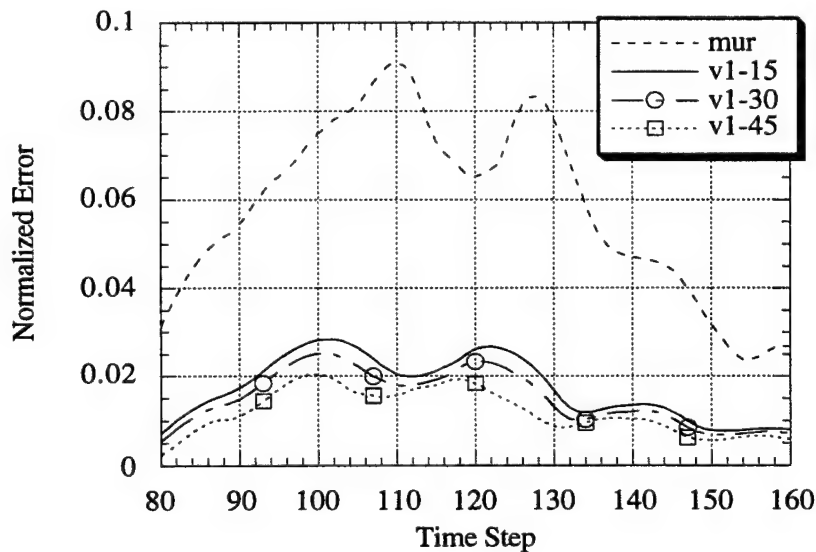


Figure 3.17 Normalized error as a function of time. "mur" is first-order Mur, $\theta_2 = 0$, and θ_1 varies in degrees as shown in the legend.

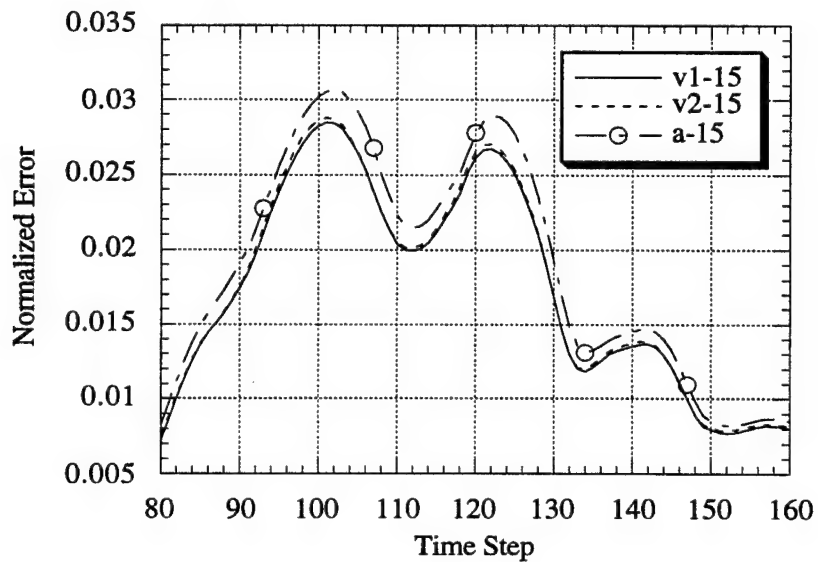


Figure 3.18 Normalized error as a function of time. "v1-15" has $\theta_1 = 15^\circ$ and $\theta_2 = 0^\circ$; "v2-15" has $\theta_1 = 0^\circ$ and $\theta_2 = 15^\circ$; "a-15" averages the multipliers.

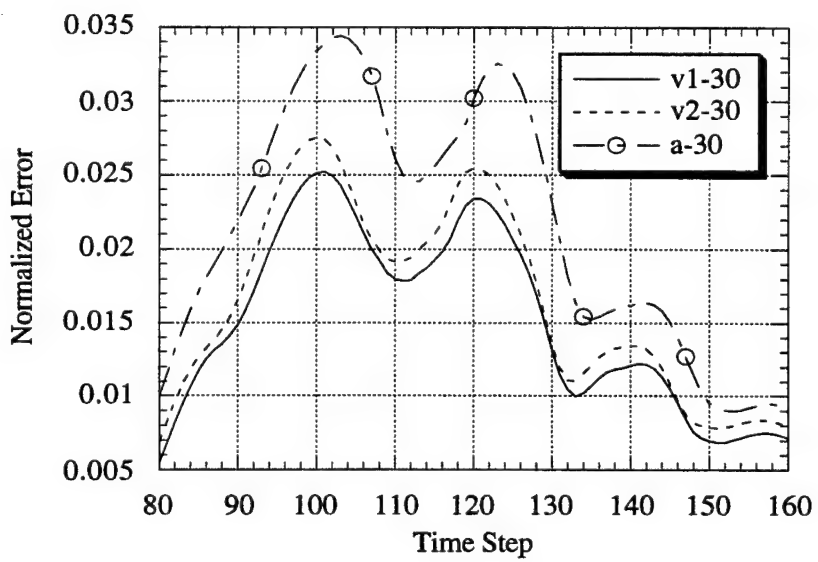


Figure 3.19 Normalized error as a function of time. "v1-30" has $\theta_1 = 30^\circ$ and $\theta_2 = 0^\circ$; "v2-30" has $\theta_1 = 0^\circ$ and $\theta_2 = 30^\circ$; "a-30" averages the multipliers.

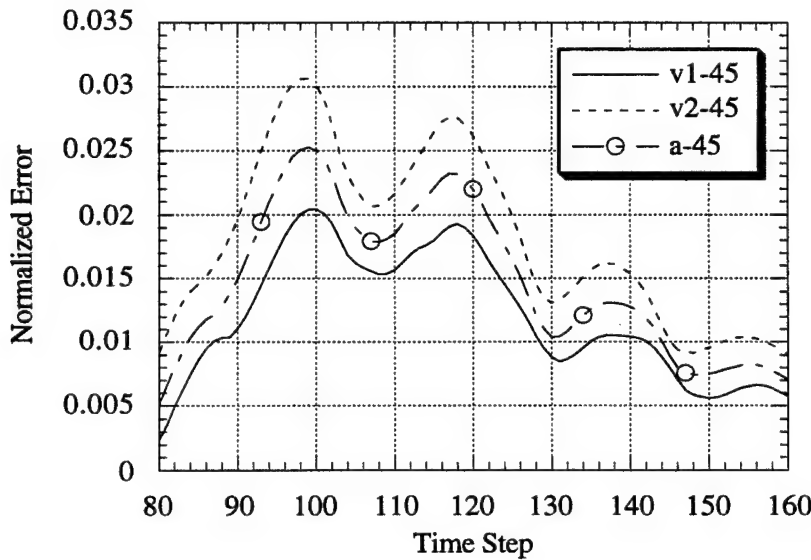


Figure 3.20 Normalized error as a function of time. "v1-45" has $\theta_1 = 45^\circ$ and $\theta_2 = 0^\circ$; "v2-45" has $\theta_1 = 0^\circ$ and $\theta_2 = 45^\circ$; "a-45" averages the multipliers.

Monitoring the error as a function of position shows the benefits of using the AABC. Figures 3.21 - 3.24 show the normalized error as a function of position for various angles. The optimal results are obtained when an angle of 45 degrees is used in conjunction with the v_1 operator. This is particularly apparent near the corner of the mesh, where the 45 degree angle causes the normalized error to be less than 5%. The error from the first-order Mur, on the other hand, is on the order of 33% near the corner. This is a key point because the second-order Mur cannot be implemented directly in the corners, and when an averaged first-order Mur is used, significant error is introduced into the numerical data. As expected, the performance near the corner improves as the angle varies from zero to 45 degrees. It is interesting to note that averaging the multipliers gives better results than modifying the v_2 operator only when the 45 degree angle is used. This can be seen from Figs. 3.22 - 3.24.

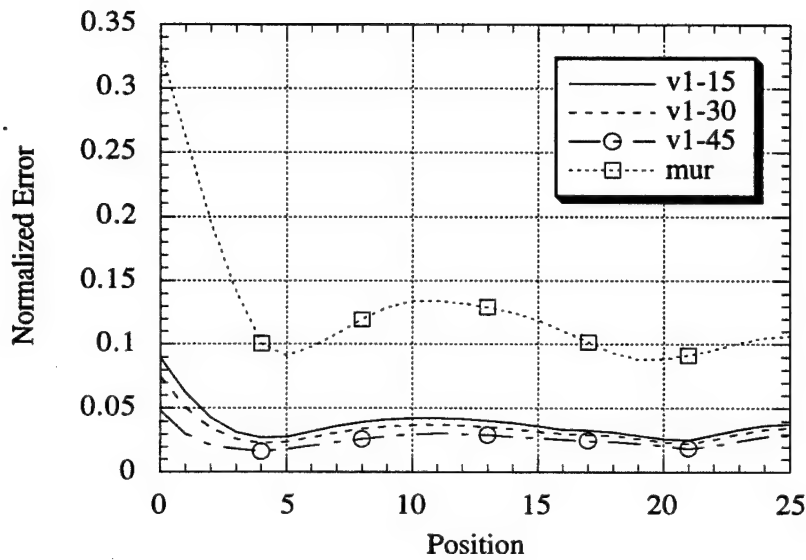


Figure 3.21 Normalized error as a function of position. Curves labeled as in Fig. 3.17.

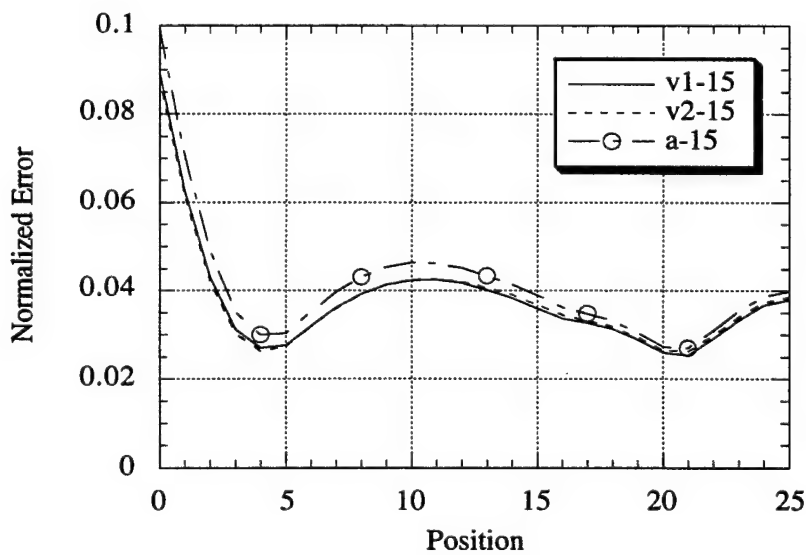


Figure 3.22 Normalized error as a function of position. Curves labeled as in Fig. 3.18.

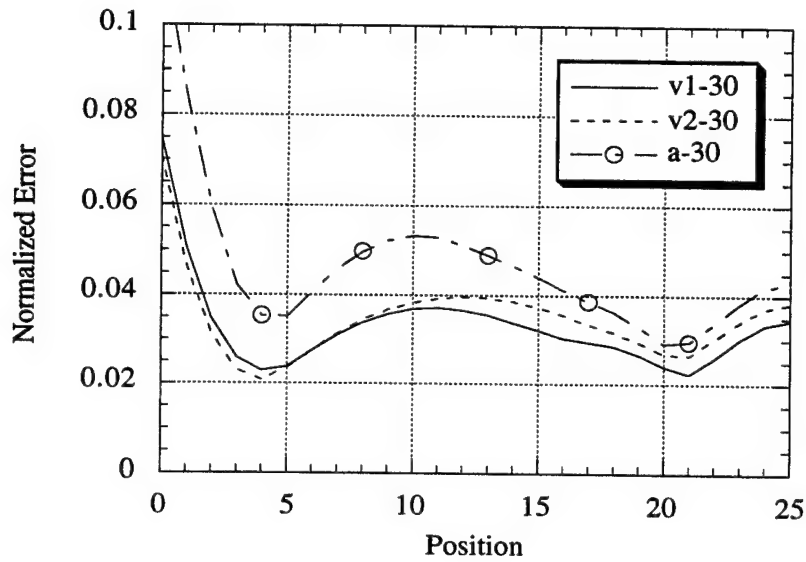


Figure 3.23 Normalized error as a function of position. Curves labeled as in Fig. 3.19.

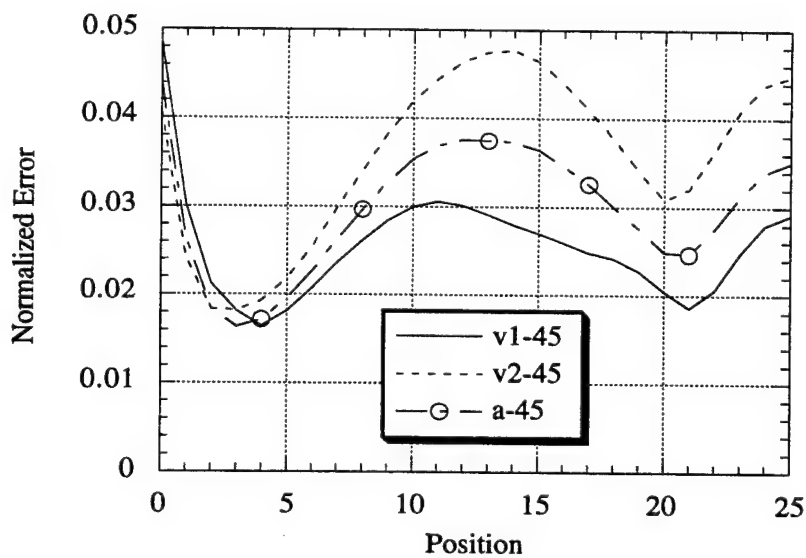


Figure 3.24 Normalized error as a function of position. Curves labeled as in Fig. 3.20.

The total error can be measured in terms of the L_1 norm as defined previously. By summing the error as a function of both position and time, a single numerical value is obtained. This procedure was followed in order to quantify the total error for the different implementations and parameter values. The calculated norms are normalized by the L_1 norm due to the first-order Mur ABC. Figure 3.25 shows the normalized total error as a function of angle. The v_1 operator has a 45° angle and the angle in the v_2 operator varies. Clearly it is best to have $\theta_1 = 45^\circ$ and $\theta_2 = 0^\circ$ to minimize the total error.

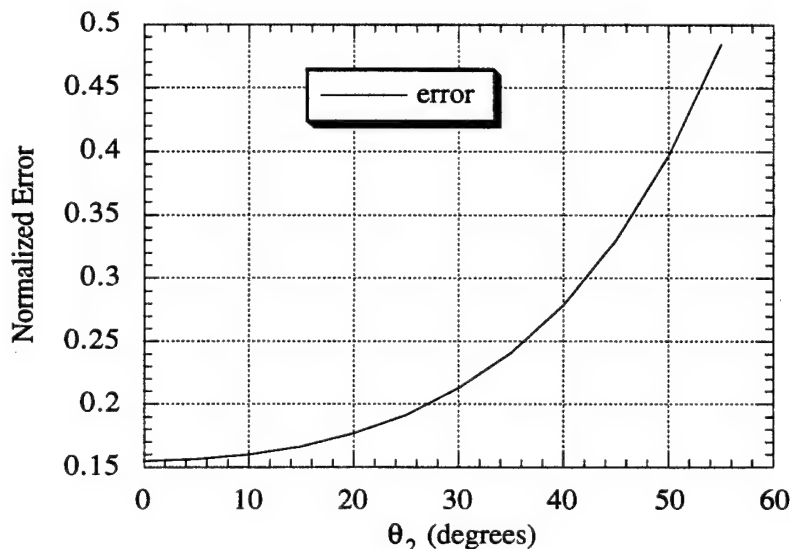


Figure 3.25 Error normalized to error due to first-order Mur. $\theta_1 = 45^\circ$ and θ_2 varies.

The total error can also be plotted as a function of the damping factor, δ . Two possible differencing schemes were presented in a previous section. These implementations of the modified DBC will be referred to as "d1" and "d2," where "d1" is given by Equation (3.20) and "d2" is given by Equation (3.21). The L_1 norms of total error are normalized by the total error due to a first-order Mur ABC and plotted as a function of δ in Fig. 3.26. As expected, the "d2" scheme is more sensitive to the value of

δ since it appears in both the numerator and denominator of the multipliers. In the "d1" scheme, the damping factor is found only in the denominator; hence, the error is less sensitive to variations of δ . Figure 3.26 shows that error is minimized for "d1" when δ is in the range of 0.15 to 0.20. Error is minimized for "d2" when δ is around 0.08. The performance of the "d1" implementation is only slightly better than for the "d2" scheme.

The addition of the damping term not only stabilizes the AABC, but also improves the performance. Figures 3.27 and 3.28 show the normalized error as a function of position for the "d2" implementation, with $\theta_1 = 45^\circ$ and $\theta_2 = 0^\circ$. Three values of δ are used as shown on the plot legend. Figure 3.27 displays the L_1 norm error normalized by the sum of the reference solution, while Fig. 3.28 shows the L_2 norm error normalized by the square root of the sum of the squares of the field values in the reference solution. These curves show the same type of behavior as the curves in Figs. 3.21 - 3.24. One interesting feature of these results is that the damping term reduces the error for positions 6 through 17.

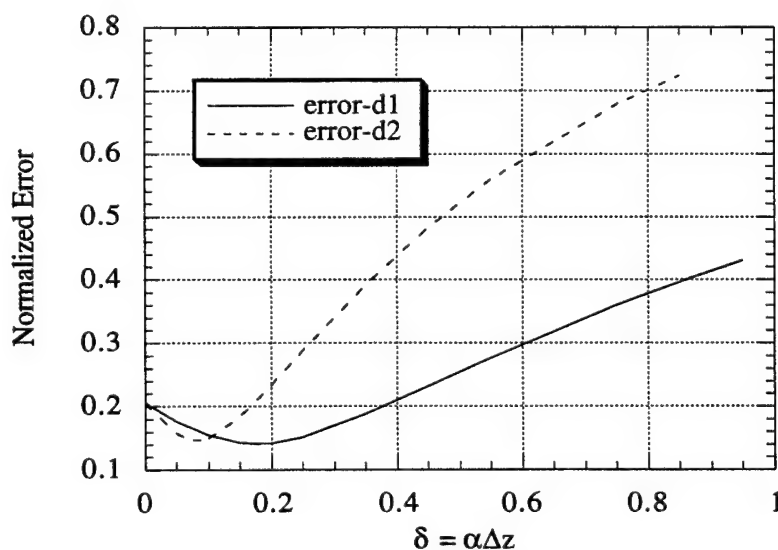


Figure 3.26 Error normalized to error due to first-order Mur. $\theta_1 = 45^\circ$ and $\theta_2 = 0^\circ$. "d1" uses Equation (3.20) and "d2" uses Equation (3.21).

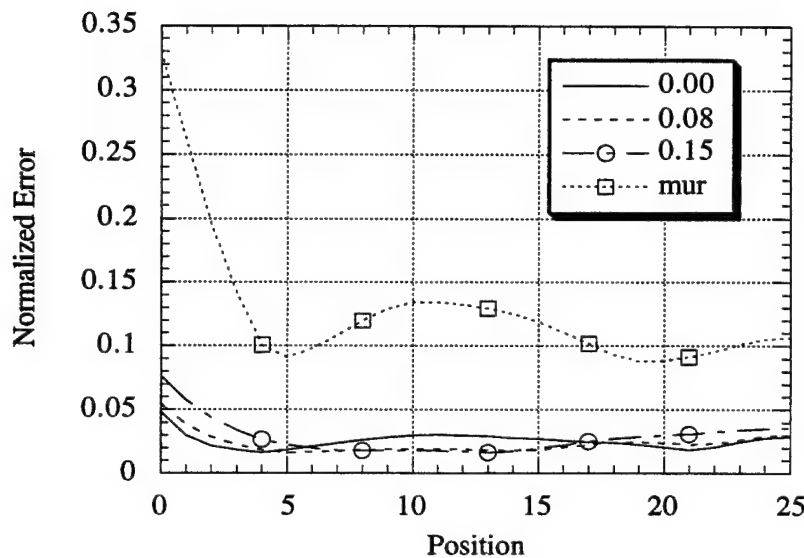


Figure 3.27 L_1 normalized error as a function of position. $\theta_1 = 45^\circ$ and $\theta_2 = 0^\circ$, "mur" is first-order Mur; AABC has δ values as shown in the legend.

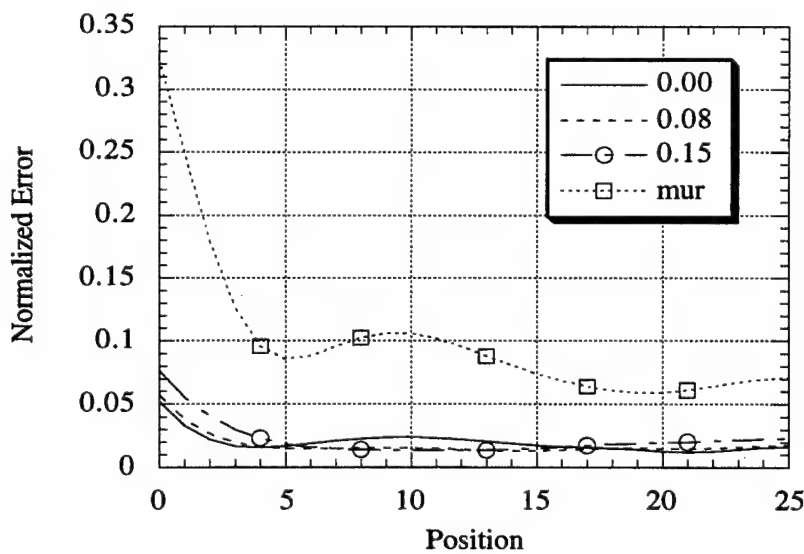


Figure 3.28 L_2 normalized error as a function of position. $\theta_1 = 45^\circ$ and $\theta_2 = 0^\circ$, "mur" is first-order Mur; AABC has δ values as shown in the legend.

The improvement is also apparent when looking at the error as a function of time. In Fig. 3.29, the normalized error from δ equal to zero is compared with results when δ equals 0.10 for two cases. In case 1, $\theta_1 = 45^\circ$ and $\theta_2 = 0^\circ$ and in case 2, $\theta_1 = 0^\circ$ and $\theta_2 = 45^\circ$. Case 1 is labeled as v1-45 on the plot legend, and the "d" indicates the nonzero δ value. The damping term actually makes the performance worse for case 2, but case 2 is inferior to case 1 in performance. Case 1 is improved with the damping factor, as desired. Figure 3.30 shows the effect of varying the value of δ for $\theta_1 = 45^\circ$ and $\theta_2 = 0^\circ$. The normalized error is plotted as a function of time; it appears that the best results occur when δ is around 0.20. This agrees with the results in Fig. 3.26.

Error norms were calculated and are presented in Table 3.3. These values agree with the graphical data, showing that the best performance is obtained when using $\theta_1 = 45^\circ$, $\theta_2 = 0^\circ$, and a nonzero δ which can be chosen according to the results in Fig. 3.26.

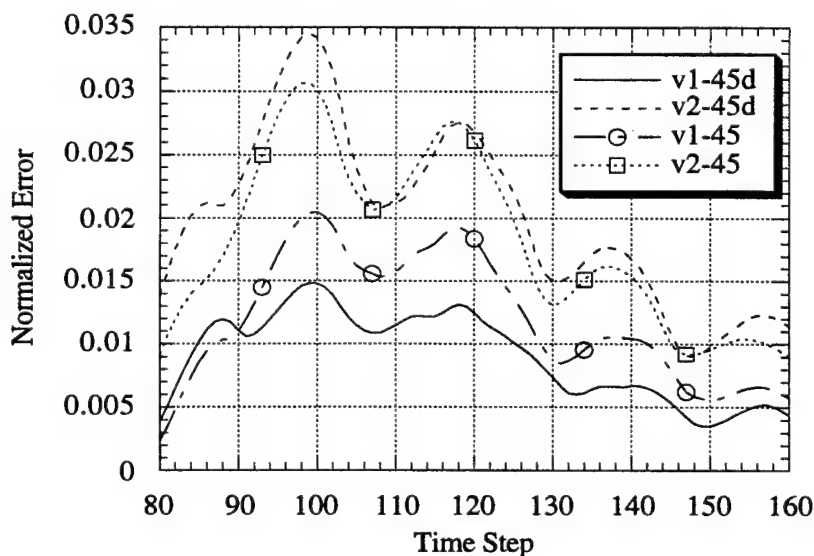


Figure 3.29 Normalized error as a function of time. "v1-45" indicates that $\theta_1 = 45^\circ$ and $\theta_2 = 0^\circ$ and "d" means that $\delta = 0.10$.

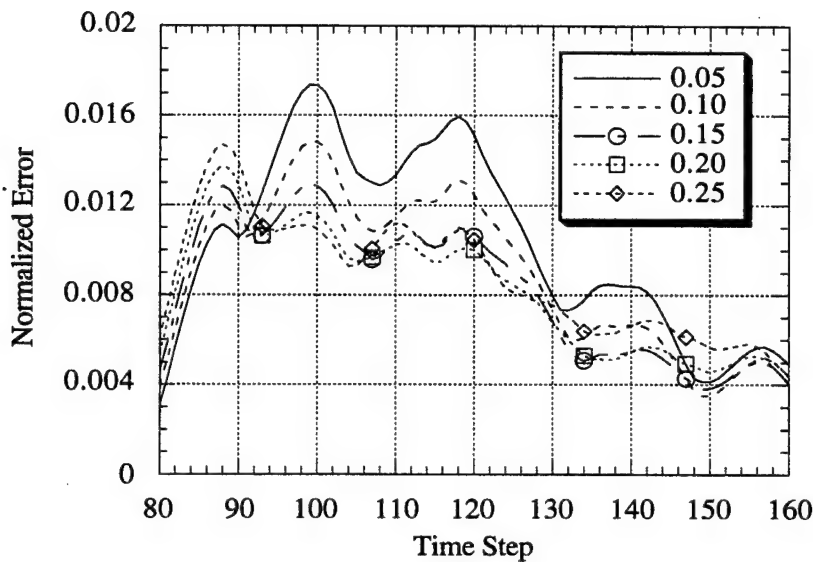


Figure 3.30 Normalized error as a function of time. $\theta_1 = 45^\circ$, $\theta_2 = 0^\circ$ and δ varies as shown in the legend.

Table 3.3 Error for AABC for a point source radiating in free space. Error is normalized to the error from the first-order Mur ABC.

δ	θ_1 (degrees)	θ_2 (degrees)	Error
0.1	45	0	0.154983
0.0	45	0	0.205506
0.1	30	0	0.223243
0.0	45, 0	average	0.253852
0.0	30	0	0.258989
0.1	15	0	0.268537
0.1	0	30	0.276025
0.1	0	15	0.277707
0.0	0	30	0.282492
0.0	15	0	0.298200
0.0	0	15	0.301365
0.0	0	45	0.311096
0.0	15, 0	average	0.324217
0.1	0	45	0.344036
0.0	30, 0	average	0.368374
First-order Mur			1.000000

3.9 Conclusions

The study of the Dispersive Boundary Condition was motivated by a discussion of the shortcomings of the Mur Absorbing Boundary Conditions. The stability issue was discussed in conjunction with the Modified Dispersive Boundary Condition. It was demonstrated that the DBC can be used to effectively absorb guided waves and radiating waves. The DBC was applied to nonuniform meshes and tested with a microstrip line problem and with a radiating point source problem. Several different implementations of the DBC on a nonuniform mesh were presented. The parameters of the DBC were varied and results were presented showing the optimal performance of the DBC in terms of minimizing reflection error. Several different forms of error analysis were presented enabling one to gauge the performance of the DBC in terms of the error as a function of both time and position.

3.10 References

- [3.1] G. Mur, "Absorbing boundary conditions for the finite-difference approximation of the time-domain electromagnetic-field equations," *IEEE Trans. Electromagn. Compat.*, vol. EMC-23, pp. 377-382, November 1981.
- [3.2] T. G. Moore, J. G. Blaschak, A. Taflove, and G. A. Kriegsmann, "Theory and application of radiation boundary operators," *IEEE Trans. Antennas Propagat.*, vol. 36, no. 12, pp. 1797-1811, December 1988.
- [3.3] R. L. Higdon, "Numerical absorbing boundary conditions for the wave equation," *Math. Comput.*, vol. 49, pp. 65-90, July 1987.
- [3.4] R. L. Higdon, "Absorbing boundary conditions for difference approximations to the multi-dimensional wave equation," *Math. Comput.*, vol. 47, pp. 437-459, October 1986.
- [3.5] Z. Bi, K. Wu, C. Wu, and J. Litva, "A dispersive boundary condition for microstrip component analysis using the FDTD method," *IEEE Trans. Microwave Theory Tech.*, vol. 40, pp. 774-777, April 1992.
- [3.6] V. Betz and R. Mittra, "Comparison and evaluation of boundary conditions for the absorption of guided waves in an FDTD simulation," *IEEE Trans. Microwave Guided Wave Lett.*, vol. 2, pp. 499-501, December 1992.

- [3.7] V. Betz, "Absorbing boundary conditions for the finite-difference time-domain analysis of guided-wave structures," M.S. thesis, University of Illinois at Urbana-Champaign, 1993.
- [3.8] J. Fang, "Investigation on the stability of absorbing boundary conditions for the time-domain finite-difference method," *IEEE AP-S Int. Symp.*, Chicago, IL, July 18-25, 1992, pp. 548-551.
- [3.9] R. L. Wagner and W. C. Chew, "An analysis of Liao's absorbing boundary condition," in *J. Electromag. Waves Appl.*; to be published.
- [3.10] K. K. Mei and J. Fang, "Superabsorption - a method to improve absorbing boundary conditions," *IEEE Trans. Antennas Propagat.*, vol. 40, no. 9, pp. 1001-1010, September 1992.
- [3.11] C. J. Railton, E. M. Daniel, D.-L. Paul, and J. P. McGeehan, "Optimized absorbing boundary conditions for the analysis of planar circuits using the finite difference time domain method," *IEEE Trans. Microwave Theory Tech.*, vol. 41, pp. 290-297, February 1993.
- [3.12] C. J. Railton and E. M. Daniel, "A comparison of the properties of radiating boundary conditions in the FDTD method for finite discretization and non-planar waves," *IEEE Trans. Antennas Propagat.*, vol. 42, no. 2, pp. 276-281, February 1994.
- [3.13] S. Bernsten and S. N. Hornsleth, "Retarded time absorbing boundary conditions," *IEEE Trans. Antennas Propagat.*, vol. 42, no. 8, pp. 1059-1064, August 1994.
- [3.14] J. Fang, "Absorbing boundary conditions applied to model wave propagation in microwave integrated circuits," *IEEE Trans. Microwave Theory Tech.*, vol. 42, pp. 1506-1513, August 1994.
- [3.15] J. P. Berenger, "A perfectly matched layer for the absorption of electromagnetic waves," *J. Comp. Phys.*, vol. 114, no. 2, pp. 185-200, October 1994.

CHAPTER 4

CHARACTERIZATION OF MICROSTRIP LINES AND DISCONTINUITIES USING NONUNIFORM ORTHOGONAL FDTD

4.1 Introduction

Accurate characterization of frequency-dependent transmission lines and transmission systems is an important topic in the area of millimeter-wave, microwave, and digital circuit design, in which it is desirable to minimize the size of circuits and electronic packages. This concern with size reduction often forces lines to bend and to be close to one another, which introduces frequency-dependent effects. Moreover, as clock rise times become smaller, the electromagnetic effects of the wave propagating along the signal lines and throughout the circuit become increasingly important. The FDTD method is an excellent tool for solving these types of problems because it provides a full-wave solution for a wide range of frequencies with only a single simulation. Circuit simulators, although very fast, on the other hand, use approximations, which are only valid under somewhat stringent restrictions on frequency range and geometrical features depending upon the circuit elements. Many of the approximations are quasi-static, and thus cannot be used for high frequencies. Additionally, in many instances, circuits are composed of complex transitions which cannot be modeled using circuit simulators. This is not a limitation for the FDTD method, which can solve arbitrarily complicated geometries including active and passive loads [4.1] limited only by the memory limitations of the computer used for the FDTD simulation.

In this chapter, the frequency-dependent characteristics of a uniform microstrip line are calculated, thus demonstrating the applicability of the FDTD method. Use of a Prony technique with the FDTD method is presented and applied to two-port scattering parameter calculations. A special update equation for triangular metallization is

introduced and shown to increase the accuracy of the FDTD method. Finally, the FDTD method and Prony technique are combined to analyze a grounded coplanar waveguide to microstrip line transition.

4.2 Uniform Microstrip Line

In this section, the uniform microstrip line of Fig. 4.1 is analyzed using the FDTD method. The width of line, W , is 150 μm , the height of the substrate, H , is 100 μm , and the dielectric constant, ϵ_r , is 13.0. These same line parameters are used in [4.2] and [4.3]. A uniform cell discretization of $\Delta x = \Delta y = \Delta z = 12.5 \mu\text{m}$ was used and Δt was set to 20.8333 fs. The line was excited with a Blackman-Harris window function with a 3 dB cutoff frequency of around 240 GHz, and the voltage and current were monitored at several locations along the line. The mesh used to describe the microstrip line was 30 x 108 x 160 cells. The bottom wall was a plane of perfect electric conductor, and the top and side walls were truncated with the first-order Mur absorbing boundary condition (ABC). The absorbing boundary conditions used on the walls that terminate the line were varied. Figure 4.2 shows the magnitude of the reflection coefficient due to the absorbing boundary as a function of frequency for the first-order Mur ABC and two implementations of the dispersive boundary condition (DBC).

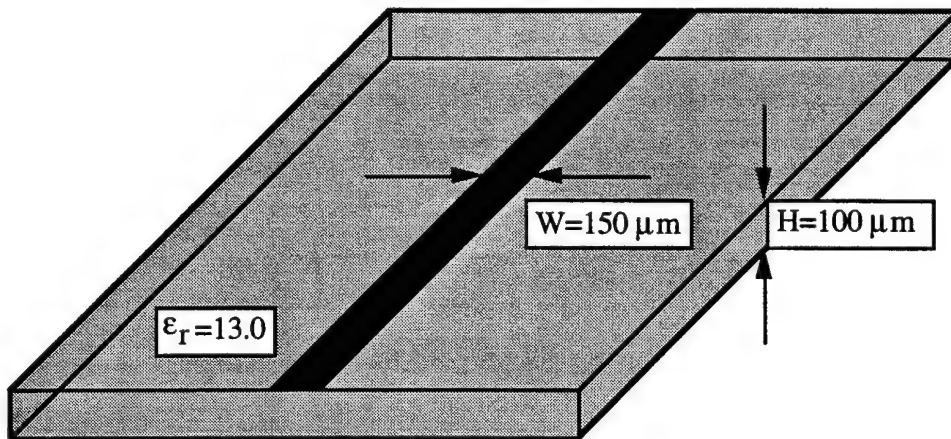


Figure 4.1 Geometry of the uniform microstrip line. The important parameters are the line width, W , the substrate height, H , and the dielectric constant, ϵ_r .

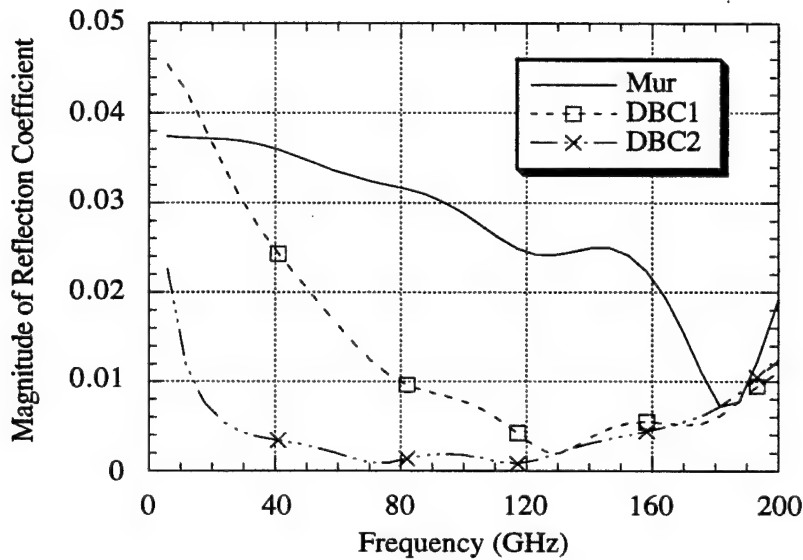


Figure 4.2 Magnitude of reflection coefficient of the imperfect absorbing boundary conditions used to truncate the mesh describing the line in Fig. 4.1. Mur refers to a first-order Mur. The dispersive boundary conditions have $\epsilon_1 = 9.4$ and $\epsilon_2 = 11.2$. DBC1 has $\delta = 0.10$ and DBC2 has $\delta = 0.01$.

Clearly, it is best to use a small value of δ when using the DBC to minimize the amount of reflection. The curve labeled "DBC2" in Fig. 4.2 shows reflections of less than 0.5% over the 20 GHz to 160 GHz frequency range. When compared with the roughly 3% error of the first-order Mur over the same frequency range, the DBC provides a significant reduction in the fields reflected from the ABC. Although the magnitude of the error shown in Fig. 4.2 for the first-order Mur is small, it corrupts the solution enough to cause oscillations in the effective dielectric constant and impedance calculations [4.4]. These oscillations can be removed by using a technique based on Prony's method [4.5]. This method is presented in the next section, and was used to calculate the reflection coefficient shown in Fig. 4.2, as well as the effective dielectric constant shown in Fig. 4.3 and the characteristic impedance shown in Fig. 4.4. There is no noticeable difference between the values calculated using the different ABCs, thus demonstrating the robustness of the technique. The agreement with the results of Becker is quite good.

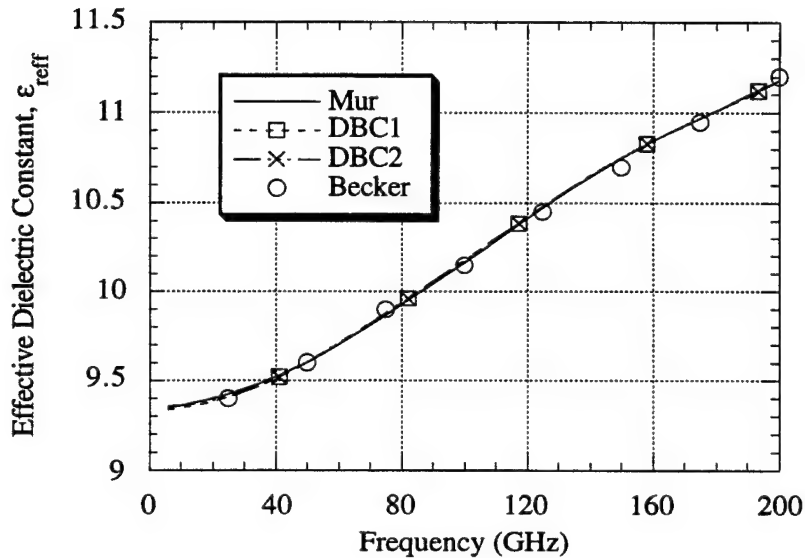


Figure 4.3 Effective dielectric constant for the microstrip line of Fig. 4.1. Absorbing boundary parameters are as noted in Fig. 4.2. The published results of Becker [4.3] are provided as a reference.

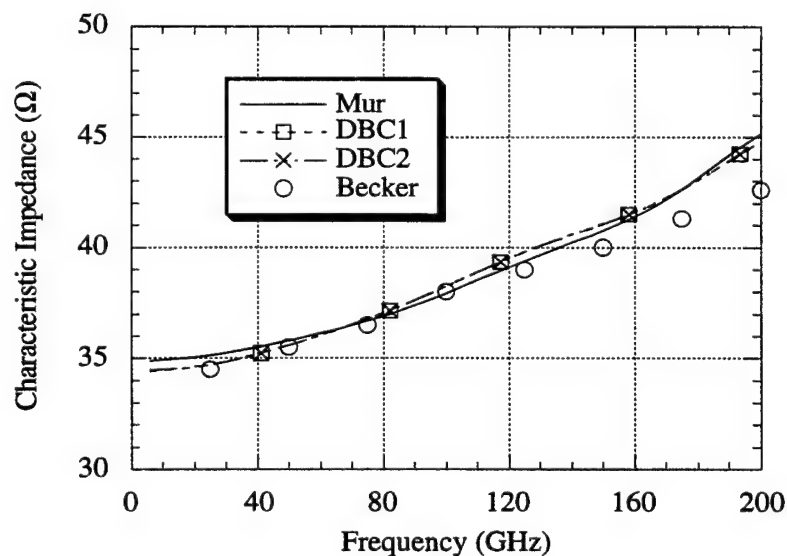


Figure 4.4 Characteristic impedance of the microstrip line of Fig. 4.1. Absorbing boundary parameters are as noted in Fig. 4.2. The published results of Becker [4.3] are provided as a reference.

4.3 Prony's Method for Scattering Parameter Extraction

The usual method [4.6] for determining scattering parameters of microstrip discontinuities requires two FDTD simulations. The first run simulates the uniform microstrip line in order to determine the incident voltage and/or current. The second run simulates the line with the discontinuity and finds the total voltage and/or current on the source side and the transmitted voltage on the other side. The reflected voltage is simply the difference between the total voltage and the incident voltage. The scattering parameters are defined in terms of the Fourier transforms of the time signatures of the incident, reflected, and transmitted voltages as shown in (4.1) and (4.2).

$$S_{11}(f) = \frac{V_{refl}(f)}{V_{inc}(f)} \quad (4.1)$$

$$S_{21}(f) = \frac{V_{trans}(f)}{V_{inc}(f)} \quad (4.2)$$

It is possible to calculate the scattering parameters with only one FDTD simulation and to eliminate the adverse effects from the imperfect ABCs [4.5]. This is achieved by using a method based on Prony's method and transmission line equations. Consider the general microstrip discontinuity problem shown in Fig. 4.5, where the voltage on the source side of the discontinuity consists of a forward traveling wave and a backward traveling wave, as does the voltage on the other side of the discontinuity. If the line runs in the z-direction and the forward traveling source is defined as A , then the voltage on Side Two can be written as

$$V_2(z) = S_{21}Ae^{-\gamma z} + \Gamma_{abc}S_{21}Ae^{-2\gamma L_2}e^{+\gamma z} \quad (4.3)$$

where Γ_{abc} is the reflection due to the imperfection of the absorbing boundary, L_2 is the length of the line from reference plane 2 to the boundary, γ is the propagation constant, and S_{21} is one of the unknown scattering parameters. Similarly, the voltage on Side One can be written as

$$V_1(z) = (A + \Gamma_{abc} S_{11} A e^{-2\gamma L_1}) e^{-\gamma z} + S_{11} A e^{+\gamma z} \quad (4.4)$$

where L_1 is the distance from reference plane 1 to the boundary, and S_{11} is the other unknown scattering parameter. Since the same numerical boundary condition is applied to all boundaries, and the distances from the reference planes to the boundaries are the same, Γ_{abc} is the same on side one as on side two. It should be noted that higher-order products of scattering parameters and reflections due to the boundaries are being neglected.

Both Equations (4.3) and (4.4) are of the form $V(z) = A^+ e^{-\gamma z} + A^- e^{+\gamma z}$, where A^+ and A^- represent the complex amplitude of the forward and backward traveling waves, respectively. These amplitudes, together with the propagation constant, give three unknowns. Thus, if the voltage is monitored at three locations along the line, the three unknowns can be determined in the following manner. First, consider the voltage on Side Two. The voltage is monitored at three z -locations in (4.3) resulting in a system of equations which is solved using the Prony method to determine γ , $S_{21}A$, and Γ_{abc} . Next, three voltages on Side One with Γ_{abc} from Side Two are used to determine A and S_{11} . Finally, the value of A determined on Side One is used to calculate S_{21} . This method is twice as efficient as the usual method for calculating scattering parameters. Numerical results are presented in the next section.

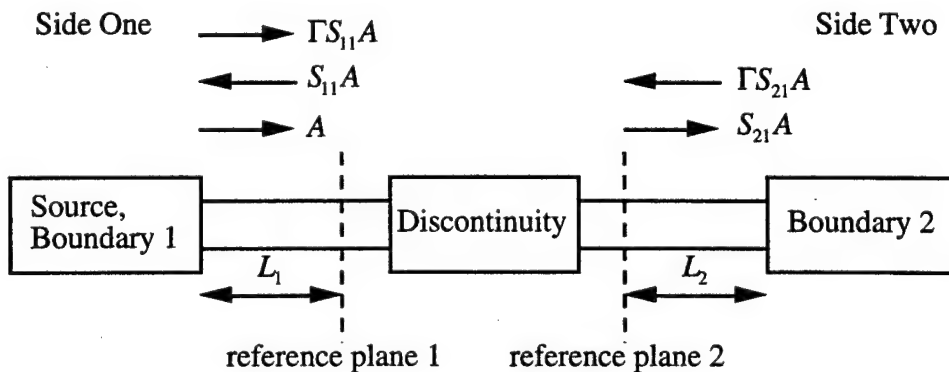


Figure 4.5 General microstrip line discontinuity with scattering parameter reference planes.

4.4 Microstrip Line with Right-Angle Bend

A common microstrip line discontinuity is the right-angle bend. The scattering parameters for this discontinuity will be calculated in this section. The geometry of the right-angle bend is shown in Fig. 4.6. The line is 4.4 mm wide and 55 mm in length on both sides of the bend. The substrate has thickness 1.6 mm and $\epsilon_r = 2.62$. These dimensions result in an impedance of approximately 50Ω near 2.5 GHz. The discretization of the mesh is $\Delta x = 0.533$ mm, $\Delta y = \Delta z = 0.55$ mm, and the time step is $\Delta t = 907.1201$ fs. The reference planes for calculating the scattering parameters are located 32 cells (17.6 mm) away from the bend. The computational domain is 140 x 140 x 15 cells, and the first-order Mur ABC is used to truncate the mesh except for the $x = 0$ boundary which is a perfect electric conductor. The microstrip line is excited 11 mm from the $z = 0$ boundary with a Blackman-Harris window function with a 3 dB cutoff frequency of 10 GHz.

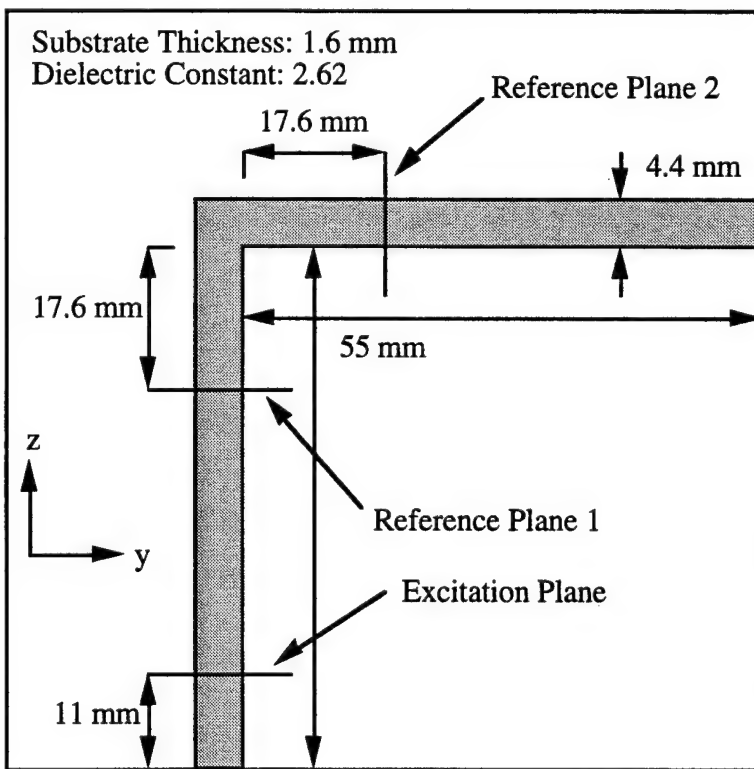


Figure 4.6 Geometry of microstrip line with right-angle bend discontinuity.

The frequency domain results in Figs. 4.7, 4.8, and 4.9 compare the scattering parameters obtained when analyzing the right-angle bend using the FDTD method with two runs, using one FDTD run and the Prony technique, and using the circuit simulator TouchStone by EEsof [4.7]. Results from Touchstone are limited to 14 GHz, and they do not account for radiation losses. The scattering parameters determined by Touchstone satisfy the relationship $S_{11}^2 + S_{21}^2 = 1$. The circuit simulator results provide a decent benchmark, and also show the value of using a full-wave solution. There is some discrepancy in the phase of the circuit simulator compared with the FDTD results. However, this is most likely because there is radiation from the line which is not accounted for by Touchstone. There is no difference between the scattering parameters found using one FDTD run and two FDTD runs. Using the Prony technique for discontinuity problems results in a savings of 50% in simulation time without loss of accuracy. Moreover, this method can be used for accurate calculation of the dispersive characteristics of microstrip lines, as demonstrated in Section 4.2.

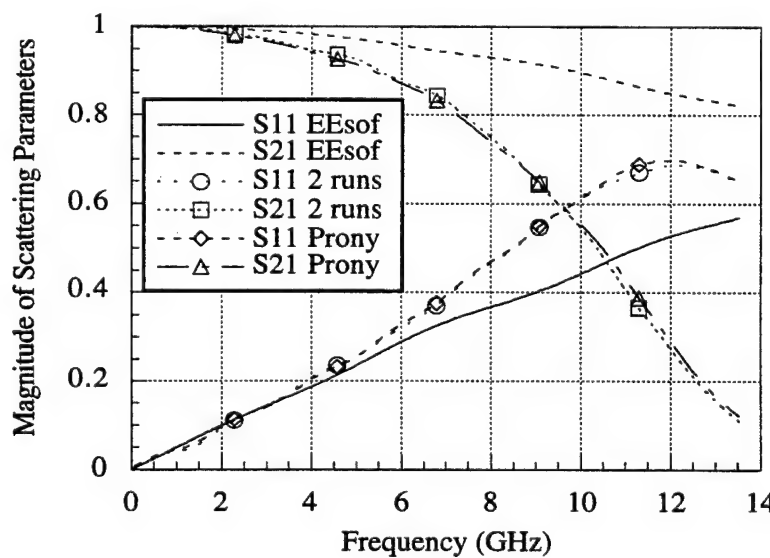


Figure 4.7 Magnitude of the scattering parameters of the right-angle bend as a function of frequency.

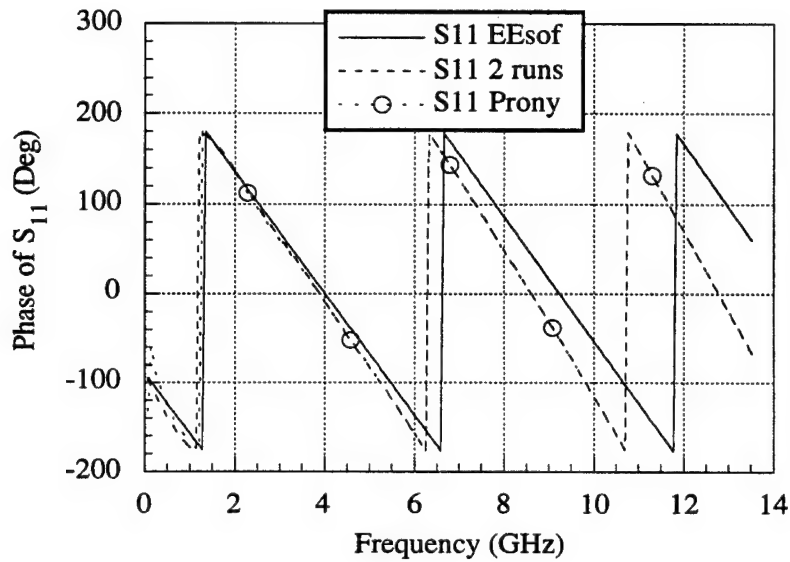


Figure 4.8 Phase of S_{11} of the right-angle bend as a function of frequency.

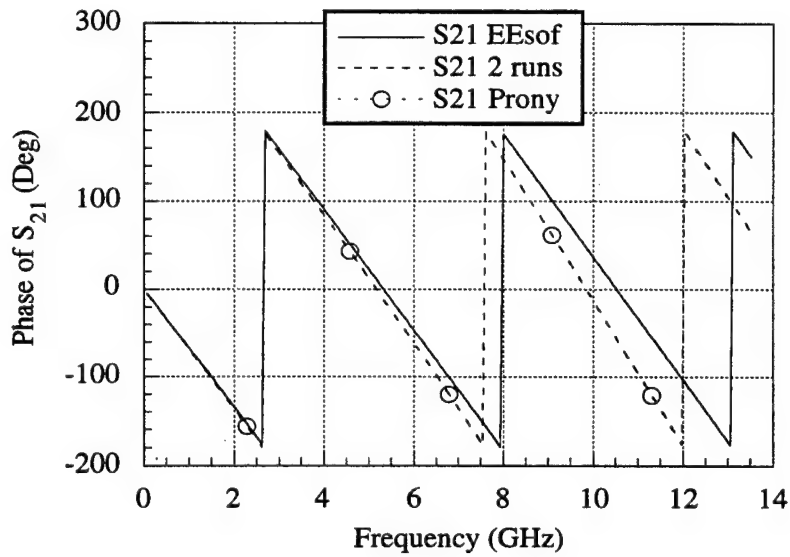


Figure 4.9 Phase of S_{21} of the right-angle bend as a function of frequency.

4.5 Microstrip Line with Mitered Right-Angle Bend

One limitation of the orthogonal FDTD method is that since the computational volume is discretized with cells shaped like bricks, geometries containing features with curves or angles that are not 90° cannot be modeled precisely. The usual practice is to use a staircase approximation to the geometry. In terms of radiation and scattering problems, staircasing usually gives good results since the current distribution in the near-field need not be computed exactly to predict the far-field accurately. However, when this technique is applied to guided-wave or circuit problems, staircasing does have a considerable effect on the results, as will be demonstrated.

A solution to the problem of accurately modeling geometries that are non-Cartesian is to use the general curvilinear FDTD method. This method, however, is expensive in terms of the time required for the update equations and the memory required, but does produce very accurate results. An alternative to the full curvilinear approach is to write a modified update equation which can be applied locally to the cells which contain non-Cartesian features. In order to demonstrate this approach, consider the infinitely thin perfect electric conductor used to model microstrip lines. Modeling lines that run at an angle with respect to the underlying Cartesian coordinate system, as well as lines with mitered corners, are examples of problems well-suited to the modified update equation.

Another common microstrip discontinuity is the mitered right-angle bend, which is shown in Fig. 4.10. The 45° miter is usually approximated in a staircase fashion as shown. A better approach is to model the metal with a triangular cell. Starting with Faraday's Law in integral form,

$$-\oint_c \vec{E} \cdot d\vec{l} = \frac{\partial}{\partial t} \iint_S \vec{B} \cdot d\vec{S} \quad (4.5)$$

and then writing the discretized version of the equation for H_x result in

$$\begin{aligned}
 H_x^{n+1/2}(j, k) &= H_x^{n-1/2}(j, k) + \frac{\Delta t}{\mu \Delta z} [E_y^n(j, k) - E_y^n(j, k-1)] \\
 &\quad - \frac{\Delta t}{\mu \Delta y} [E_z^n(j, k) - E_z^n(j-1, k)]
 \end{aligned} \tag{4.6}$$

Now, assume that the magnetic field H'_x is positioned at the center of the triangle as shown in Fig. 4.10. Following the integration path as shown in the figure gives the following update equation.

$$H_x^{n+1/2}(j, k) = H_x^{n-1/2}(j, k) + \frac{2\Delta t}{\mu \Delta y \Delta z} [E_y^n(j, k) \Delta y + E_z^n(j-1, k) \Delta z] \tag{4.7}$$

Equation (4.7) was implemented to model infinitely thin triangular PEC sections.

Mitered Right-Angle Bend

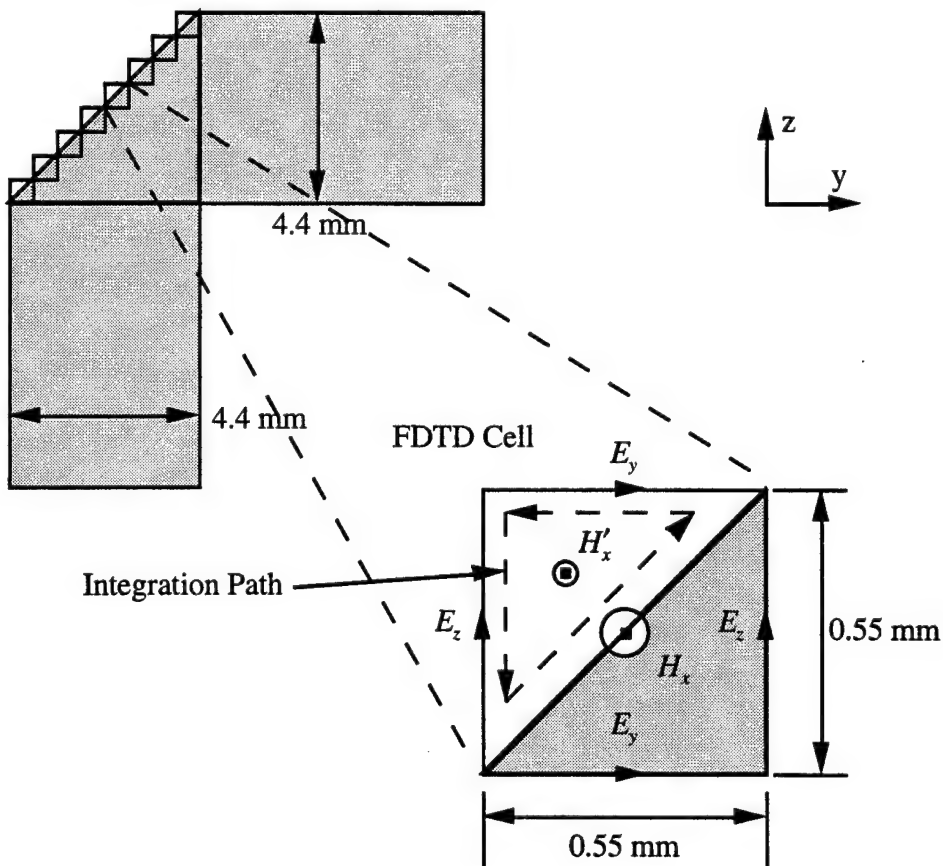


Figure 4.10 Mitered right-angle bend with detailed FDTD cell.

The mitered right-angle bend was simulated with the staircase approximation and the triangle cell approximation. The mesh, excitation, and reference planes are the same as shown in Fig. 4.6. To show the effect of the miter on the bend, Fig. 4.11 shows the voltage at reference plane 1. Here the triangle approximation, the staircase approximation, and the square right-angle bend cases are compared. The miter clearly reduces the reflection, and there is a slight difference between the two miter approximations. Figures 4.12, 4.13, and 4.14 compare the scattering parameters found via FDTD for the mitered bend with those calculated using TouchStone. While there is not much difference between the values of S_{21} computed using the two approximations, there is a significant difference when comparing the S_{11} values. Although the staircase approximation is very fine, it results in a value of S_{11} that is larger than the EEsof result. On the other hand, the triangular cell approximation gives extremely good agreement with EEsof up to about 9 GHz.

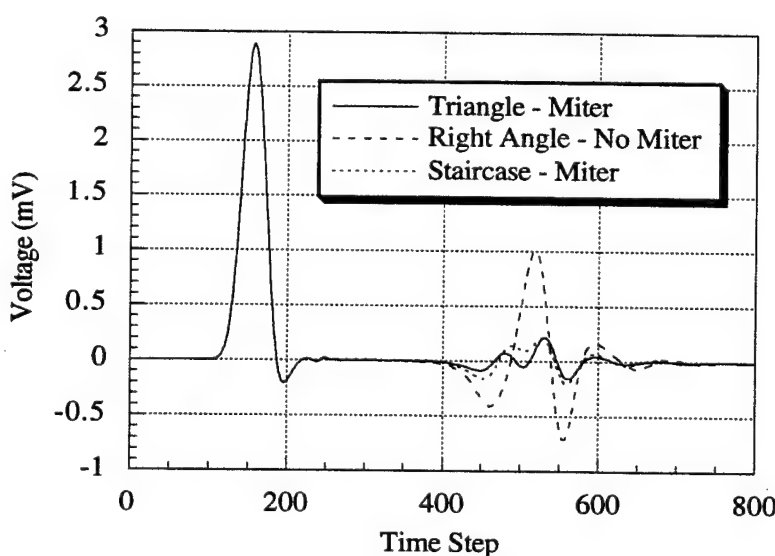


Figure 4.11 Voltage at reference plane 1 as a function of time.

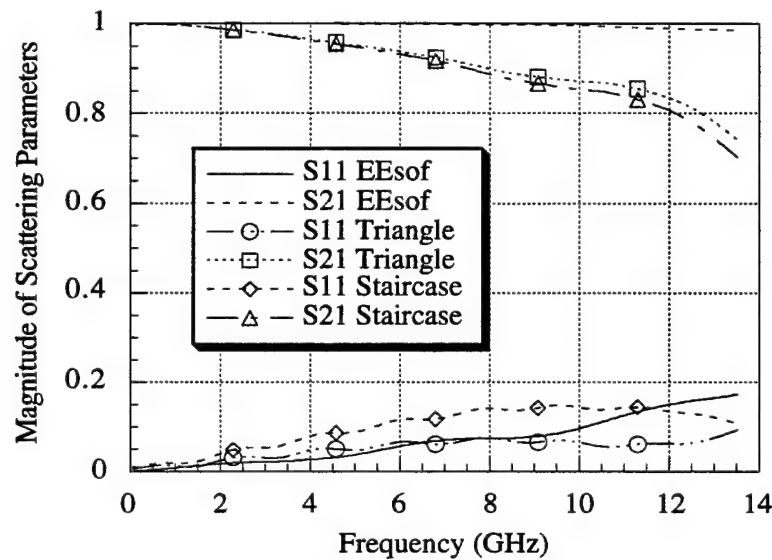


Figure 4.12 Magnitude of scattering parameters for the mitered right-angle bend as a function of frequency.

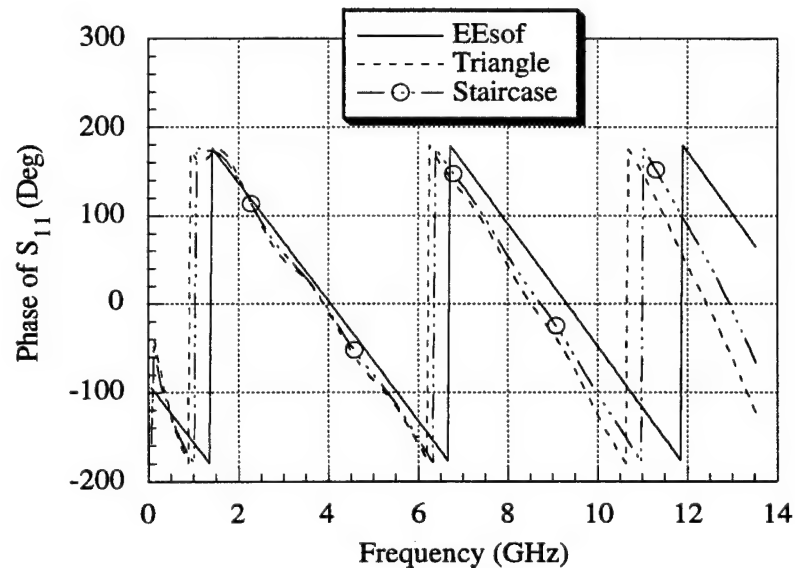


Figure 4.13 Phase of S_{11} for the mitered right-angle bend as a function of frequency.

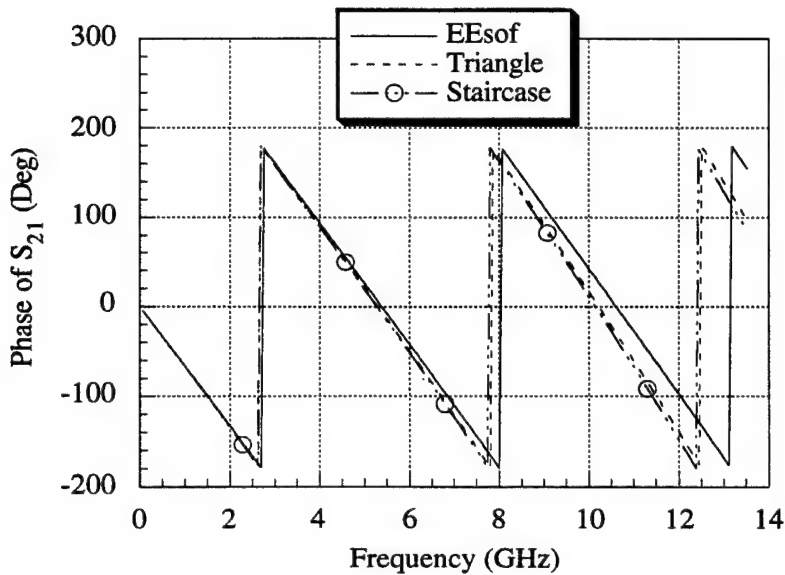


Figure 4.14 Phase of S_{21} for the mitered right-angle bend as a function of frequency.

4.6 Skewed stripline

The effect of the staircase on the fields propagating along a microstrip line can be determined by analyzing a stripline that runs at an angle of 45° with respect to the underlying Cartesian grid. The geometry and approximations are shown in Fig. 4.15, where $W = 2.07$ mm, $H = 5.08$ mm, and the relative dielectric constant is 5. The stripline structure was excited with a Blackman-Harris window function with a 3 dB cutoff frequency of 8.65 GHz, and the voltage was monitored at several locations along the line. An expression for the effective dielectric constant in terms of the Fourier transform of the voltage at two locations, separated by a distance L on the line, is given in (4.8).

$$\epsilon_{\text{eff}}(\omega) = \left[\left(\frac{c_o}{\omega} \right) \ln \left(\frac{\tilde{V}(d)}{\tilde{V}(d+L)} \right) \right]^2 \quad (4.8)$$

where c_o is the speed of light in free space, and $\tilde{V}(d)$ is the Fourier transform of the voltage at position d . Since the structure being analyzed is stripline, it is known that the

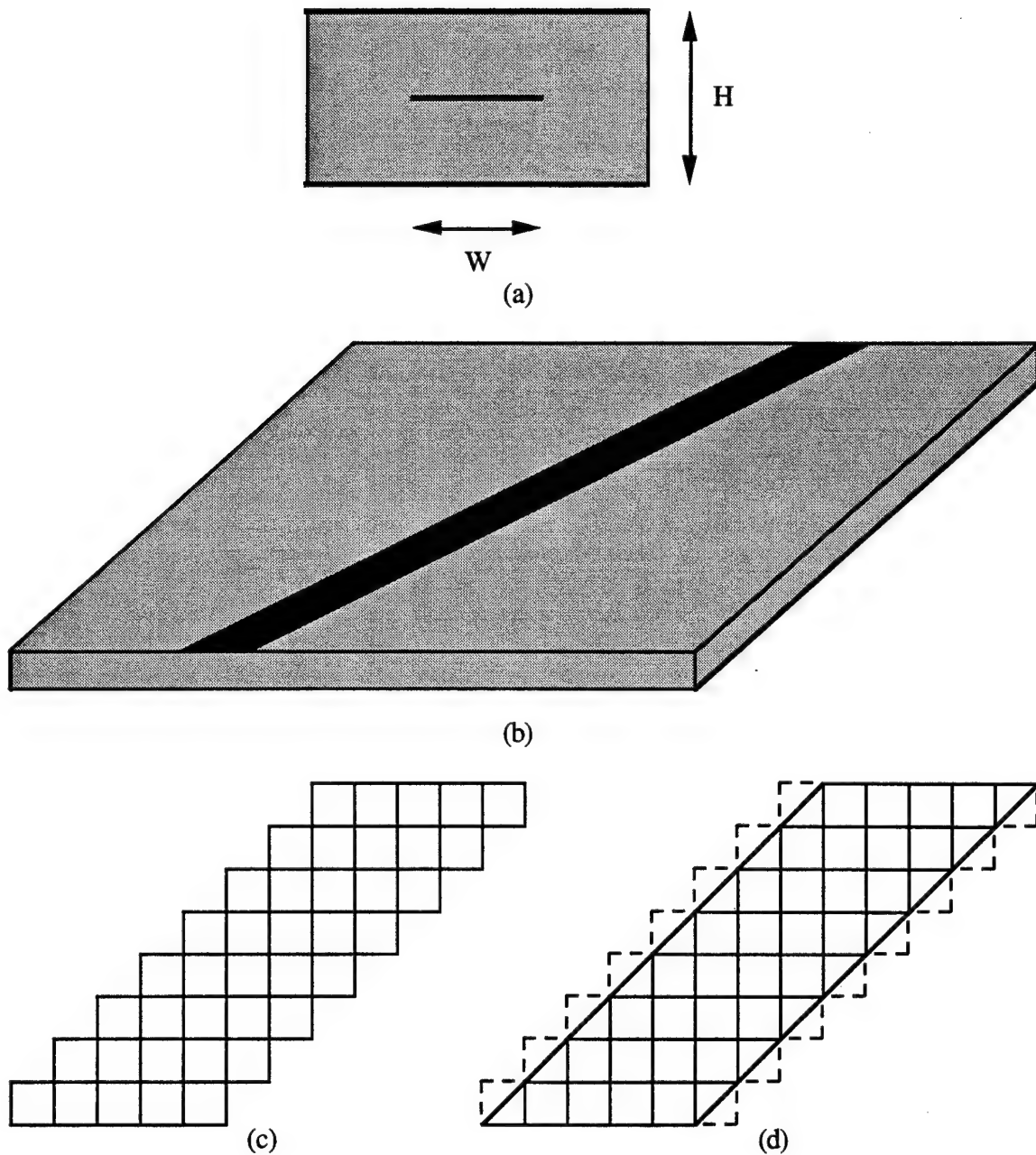


Figure 4.15 (a) Cross-section of stripline with $W = 2.07$ mm and $H = 5.08$ mm. (b) Line at angle of 45° with respect to the underlying grid. (c) Staircase approximation to the line. (d) Triangular cell approximation to the line.

value of $\epsilon_{\text{ref}}(\omega)$ is a constant, and, in this particular case, the constant is 5. Equation (4.8) will be used to calculate ϵ_{ref} for a straight stripline and for the 45° line with the staircase and triangular cell approximations. The deviation of ϵ_{ref} from the expected value will gauge the effectiveness of the approximations.

The voltage as a function of time at two locations 7.7625 mm apart on a straight stripline is shown in Fig. 4.16. Note that there is virtually no dispersion of the voltage pulse as it propagates along the line. Figure 4.17 shows the voltage as a function of time at two locations 10.98 mm apart on the angled stripline of Fig. 4.15. There is a considerable amount of dispersion in both approximations. Since the voltage values are similar, it is helpful to examine the difference between the two. The voltage from the triangular cell approximation is subtracted from the staircase voltage and plotted in Fig. 4.18. This clearly shows that the voltage travels slower when the staircase approximation is used. Exactly how much slower the voltage travels can be ascertained by examining Fig. 4.19 which is a plot of the relative effective dielectric constant as a function of frequency. The staircase approximation yields an error of about 9%, whereas the triangular cell approximation gives an error of at most 3%. This is significant, since doubling the mesh density using the staircase approximation still gives an error of about 5% [4.8]. Using the triangular cell approximation, the accuracy is improved by a factor of three without increasing the size of the problem or slowing the update equations.

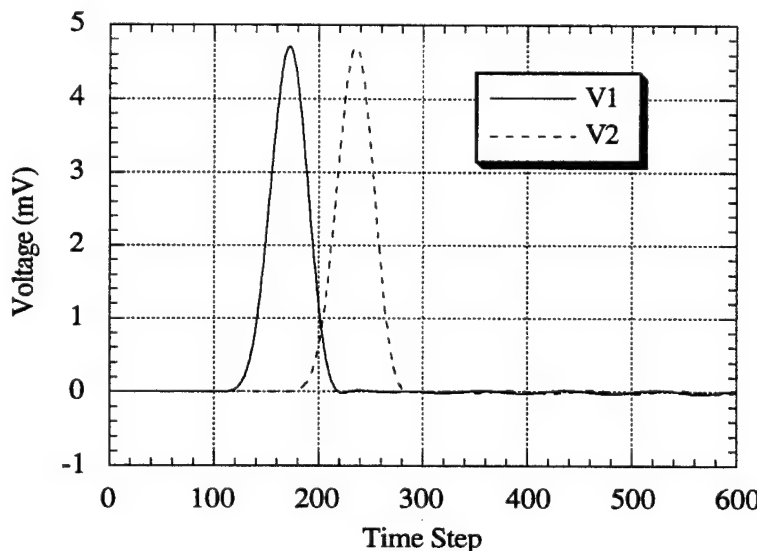


Figure 4.16 Voltage waveforms as a function of time at two positions along a straight stripline. The monitoring positions are 7.7625 mm apart.

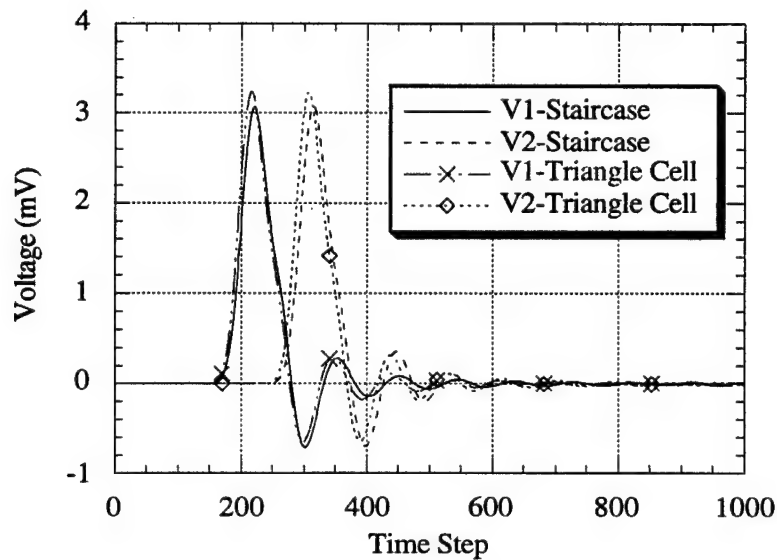


Figure 4.17 Voltage waveforms as a function of time at two positions along an angled stripline. The monitoring positions are 10.98 mm apart.

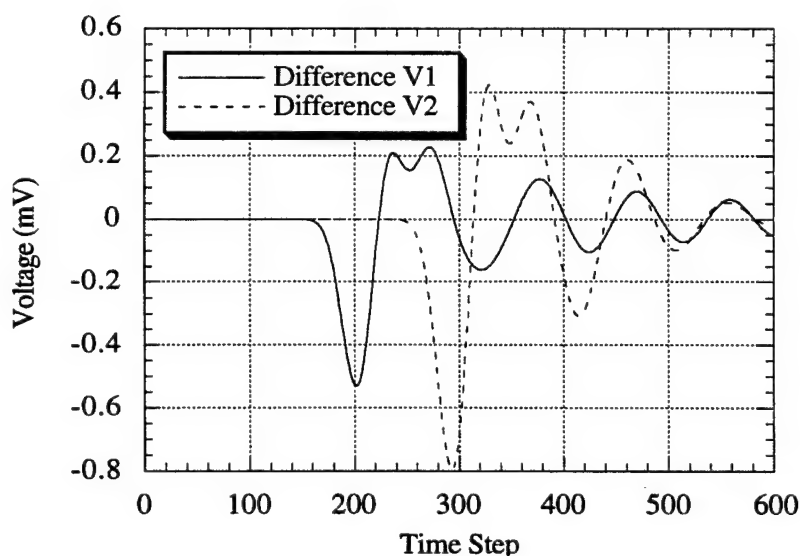


Figure 4.18 Difference between the staircase and triangular cell approximations in the voltage waveforms of Fig. 4.17. The approximations give rise to different propagation constants.

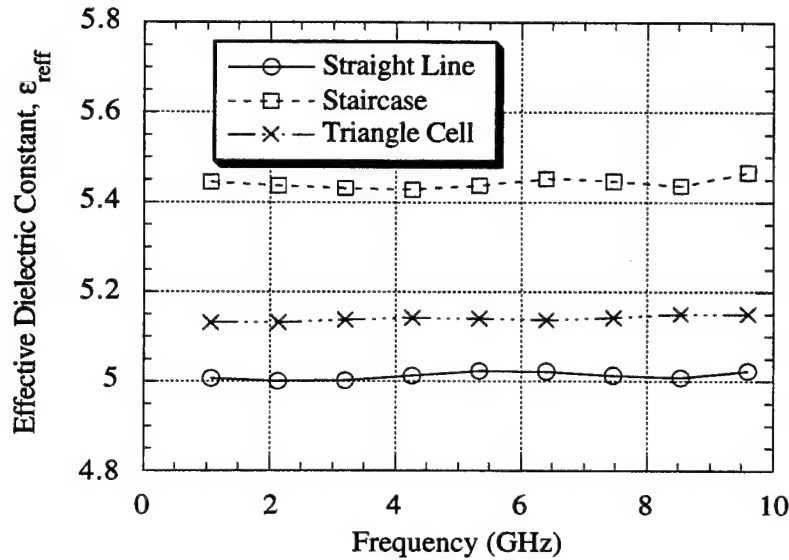


Figure 4.19 Effective dielectric constant as a function of frequency. The triangular cell approximation is three times more accurate than the staircase approximation.

4.7 Straight Stripline

In the previous section, a skewed stripline was analyzed. The effective dielectric constant was calculated as a function of frequency from the time domain voltage. In order to limit the source of error to the staircase or triangular cell approximations, the simulations were stopped before reflections from the ABCs could contaminate the time domain data. In this section, the straight stripline is again considered. However, in this section, the reflections from the ABCs terminating the computational domain will have an effect on the calculation of the effective dielectric constant. Two different ABCs were used on the end walls of the stripline, the first-order Mur and the DBC. The parameters for the DBC were chosen as $\epsilon_{r1} = \epsilon_{r2} = 5.0$ and $\delta = 0.01$. The magnitude of the reflection coefficient due to the ABCs is shown in Fig. 4.20. Both ABCs work very well

absorbing the TEM wave propagating along the stripline. The reflection is less than 0.02% for the DBC in the 0.5 GHz to 4.5 GHz frequency range.

Figure 4.21 shows the effective dielectric constant as calculated using (4.8). The reflection from the first-order Mur causes oscillations in the effective dielectric constant results. The oscillatory behavior is not present in the effective dielectric constant curve calculated using the voltage found with the DBC. The Mur and DBC results are compared to a case in which no reflection is present in the time domain data. When no reflection is present, the time domain voltage signature is four times shorter than that with the reflection present. This explains the difference in the frequency resolution between the Mur, DBC, and straight line cases. Figure 4.22 shows the effective dielectric constant calculated using the Prony technique of Section 4.3. The Prony technique eliminates all oscillatory behavior from the curves. The results are again compared with those for the straight line case, which does not have a reflection present in the time domain data.

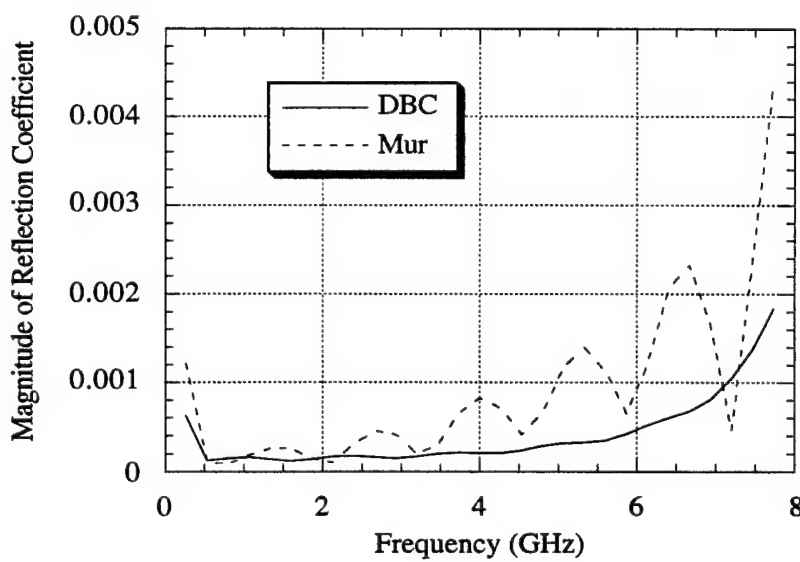


Figure 4.20 Magnitude of reflection coefficients of the absorbing boundary conditions applied to the straight stripline problem. Both the first-order Mur and the DBC perform extremely well for this case.

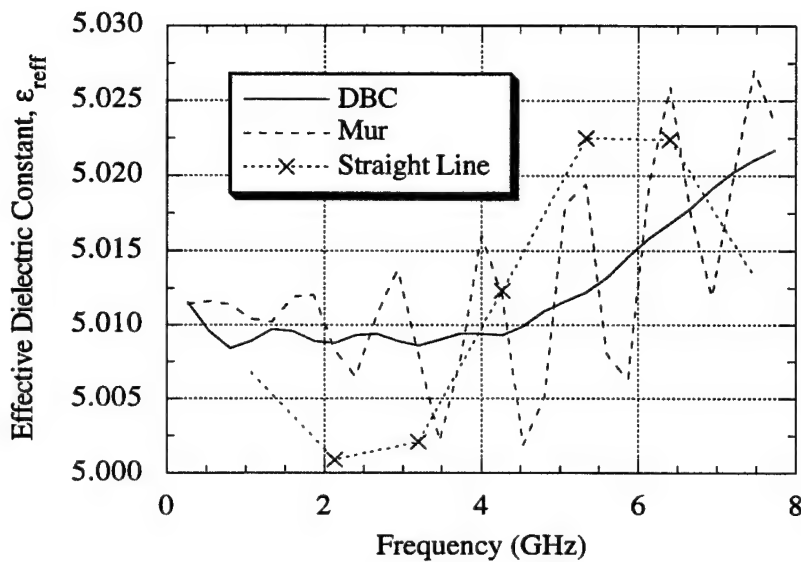


Figure 4.21 Effective dielectric constant for the straight stripline. The effect of the absorbing boundaries is shown. The "straight line" curve was obtained from a time signature with no reflection present.

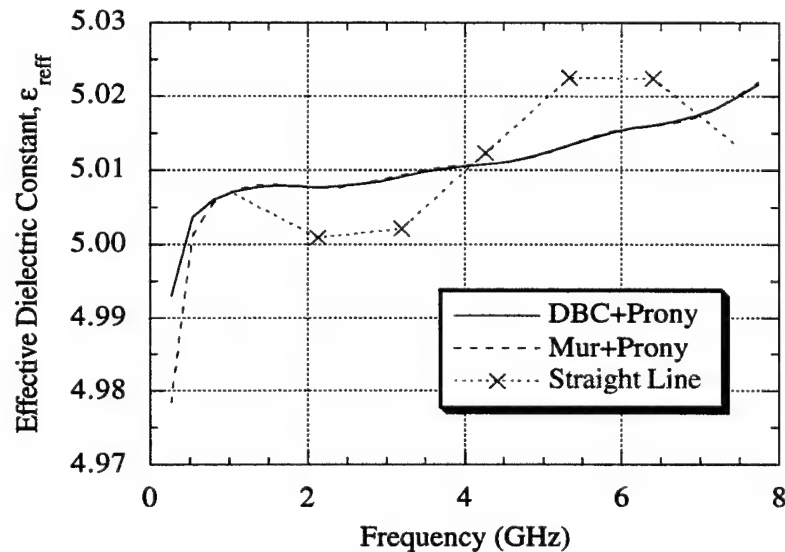


Figure 4.22 Effective dielectric constant for the straight stripline. The Prony technique eliminates the effect of the absorbing boundary. The "straight line" curve was obtained from a time signature with no reflection present.

4.8 Coplanar Waveguide to Microstrip Line

Designing and constructing practical microwave and millimeter-wave circuits often require an accurate characterization of discontinuities that cannot be adequately modeled using circuit simulators. This is especially true at higher frequencies where a full-wave solution to Maxwell's equations is needed. In certain circumstances, when two different types of waveguiding structures are connected, there are simply no models of these types of transitions in circuit simulators. Some examples of transitions typically not found in circuit simulators are the transitions of a microstrip line to a grounded coplanar waveguide, a slotline to a finline waveguide, and a microstrip line to a waveguide. The analysis of the transition from a coplanar waveguide to a microstrip line is presented in this section.

Both quasi-static and full-wave solution methods have been used to characterize a coplanar waveguide [4.9]. A coplanar waveguide is preferred over a microstrip line for several reasons [4.10]. Since the electric field is confined to the narrow slot region, a relatively small amount of the field is subjected to substrate losses as compared with the microstrip line. Additionally, having the ground and signal lines in the same plane is desirable when including devices in the circuit. When the ground and signal lines are not on the same plane, a hole through the substrate is required to reach electric ground; this situation is impractical. Moreover, coupling effects between adjacent lines are very weak since a ground plane separates them. When an additional ground plane is present, as is the case with a grounded coplanar waveguide, the gap width should be small compared to the substrate thickness in order to minimize the effect of the microstrip mode.

The top view of the transition from a grounded coplanar waveguide to a microstrip line is shown in Fig. 4.23. The thickness of the dielectric separating the ground planes is 254 μm and the dielectric constant is 2.2. The thickness of the top ground plane and microstrips is 16.9333 μm . The width of the conducting strip of the coplanar waveguide, W_1 , is 442 μm , and the width of the slot, S_1 , is 54.5 μm . The

transition from the coplanar waveguide to the microstrip line is 1.1 mm long, and the taper angle of the top ground plane is 45° . The distance from the top ground plane to the microstrip line, S_2 , is 930 μm , the taper angle of the center conductor is 11.5° , and the width of the microstrip line is 889 μm .

The mesh used to describe this problem is very dense because of the finite thickness of the conducting strips and the need to accurately model the slot in the coplanar waveguide. The mesh was discretized with $\Delta x = 50 \mu\text{m}$, $\Delta y = 8.5 \mu\text{m}$, and $\Delta z = 16.933 \mu\text{m}$. A nonuniform mesh was used in the y -direction in order to have at least $3*W_2$ of space between the microstrip line and the end of the mesh. The largest Δy was 17 μm . First-order Mur ABCs were used on the y -walls and the top wall. The bottom wall was pec, and the z -walls were terminated with DBCs with $\epsilon_{r_1} = 1.403$, $\epsilon_{r_2} = 2.1$, and $\delta=0.01$.

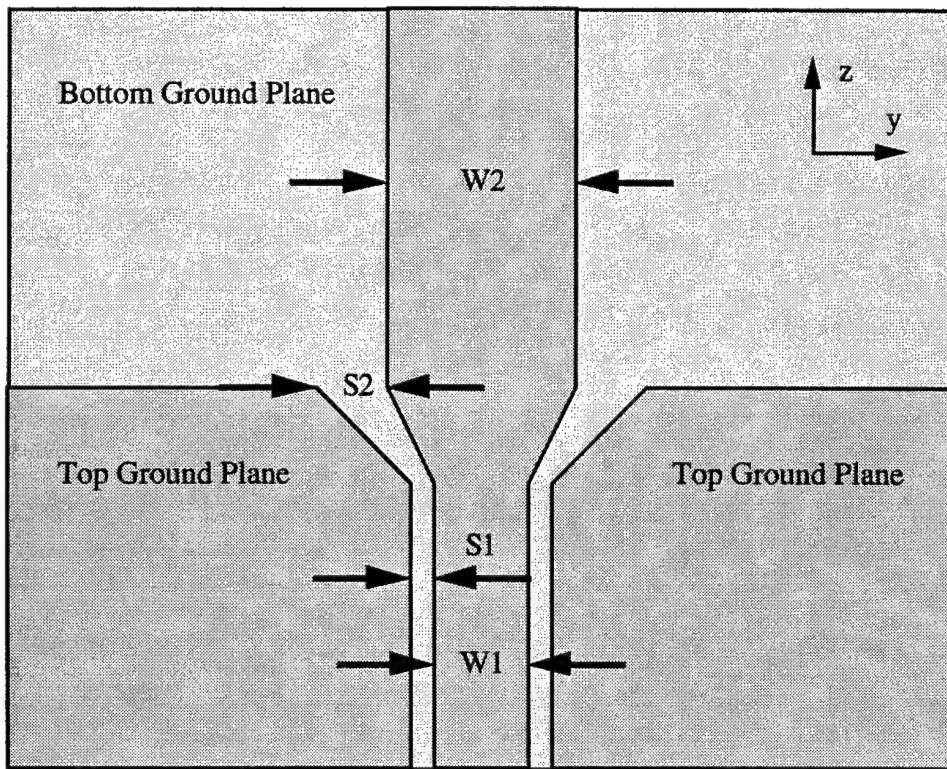


Figure 4.23 Top view of the grounded coplanar waveguide to microstrip line transition. $W_1=442 \mu\text{m}$, $W_2=889 \mu\text{m}$, $S_1=54.5 \mu\text{m}$, and $S_2=930 \mu\text{m}$, and the transition is 1.1 mm long.

The mesh had 40 cells in the x-direction, 300 cells in the y-direction, and 152 cells in the z-direction. The discontinuity was 22 cells long in the z-direction and centered in the mesh. The electric field in the slot of the coplanar waveguide was excited with a Blackman-Harris window function with a 10% cutoff frequency of 100 GHz. The voltage in the slot and the current around the center conductor were monitored at several locations along the coplanar waveguide. The voltage under the center conductor was monitored in the transition region, and on the microstrip side of the problem, the voltage and current were monitored at several locations. Time domain plots of the voltage are shown in Figs. 4.24 - 4.26. The numbers in the plot legends refer to the cell monitoring location in the z-direction. The voltage plots in these figures show that the voltage undergoes considerable reflection because of the transition as well as dispersion due to the air-dielectric interface.

Using the Prony technique to extract forward and backward traveling voltage and current waves, the impedance of the lines was calculated and is shown in Fig. 4.27. The coplanar waveguide impedance is a few ohms lower than the desired 50Ω at 77 GHz.

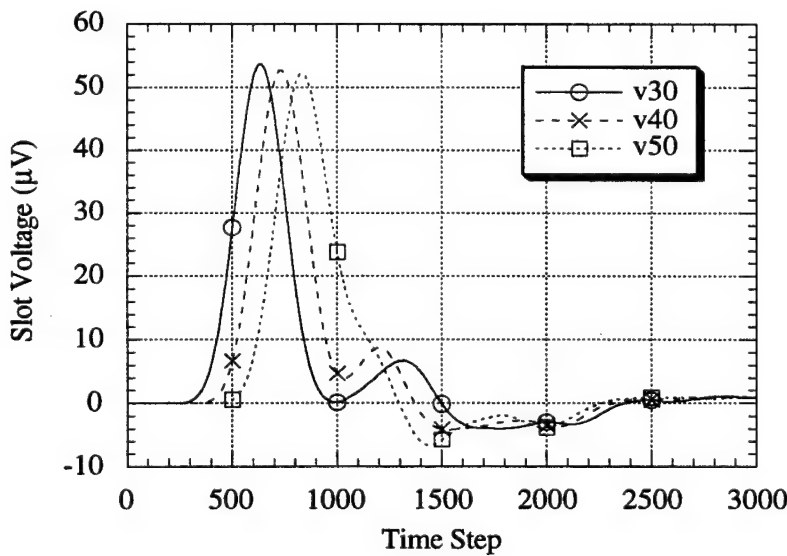


Figure 4.24 Voltage in the slot of the grounded coplanar waveguide as a function of time. The voltage is shown at three successive monitoring locations in the z-direction.

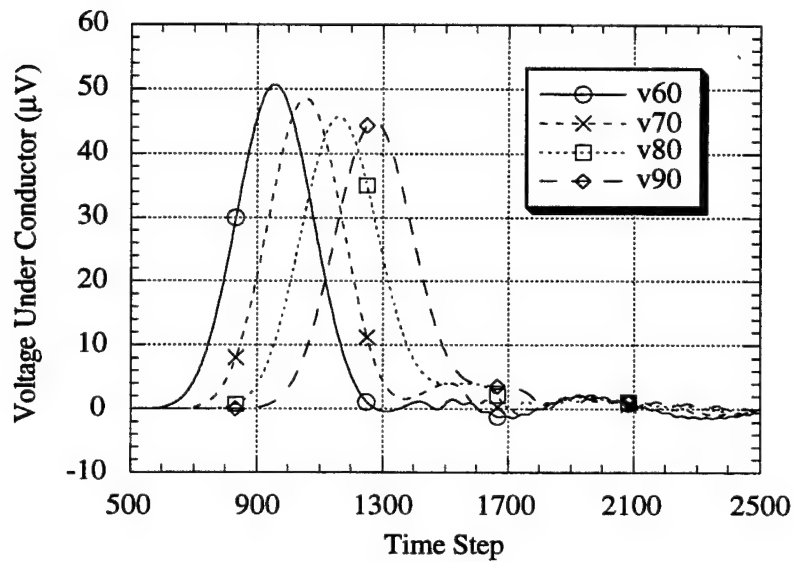


Figure 4.25 Voltage under the conductor in the transition region as a function of time. The voltage is shown at four successive monitoring locations in the z-direction.

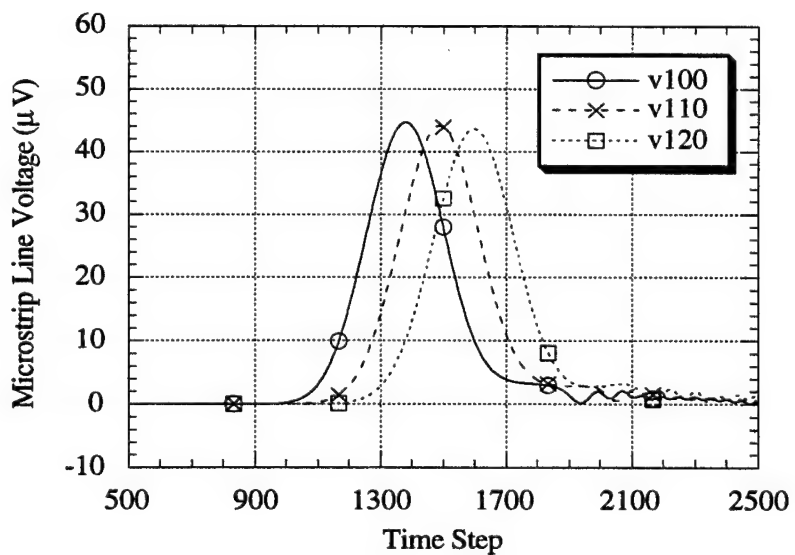


Figure 4.26 Microstrip line voltage as a function of time. The voltage is shown at three successive monitoring locations in the z-direction.

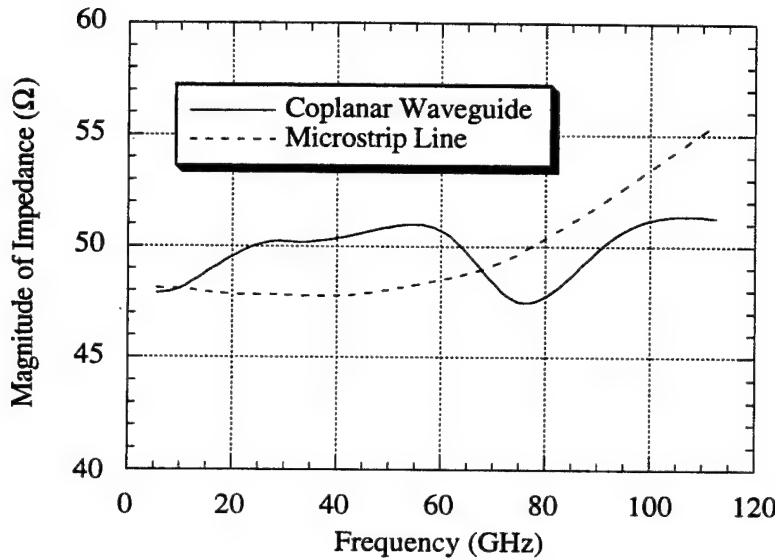


Figure 4.27 Magnitude of the impedance of the grounded coplanar waveguide and the microstrip line as a function of frequency.

Since the impedances on either side of the transition discontinuity are not the same, normalized scattering parameters must be used. The expression for S_{21} is given in (4.9)

$$S_{21}(f) = \sqrt{\frac{Z_2(f)}{Z_1(f)}} \frac{\tilde{I}_2(f)}{\tilde{I}_1(f)} \quad (4.9)$$

where $\tilde{I}_2(f)$ is the Fourier transform of the time domain current on the microstrip side of the discontinuity, $Z_2(f)$ is the impedance of the microstrip line, and the subscript "1" refers to the grounded coplanar waveguide. Running the simulation again with the excitation on the microstrip line side of the discontinuity enables the calculation of all four scattering parameters. The magnitudes of the scattering parameters of the coplanar waveguide to microstrip line transition are shown in Fig. 4.28. The phase is shown in Fig. 4.29. It should be noted that S_{21} and S_{12} were slightly different, so an average of the two values was taken, thereby enforcing reciprocity.

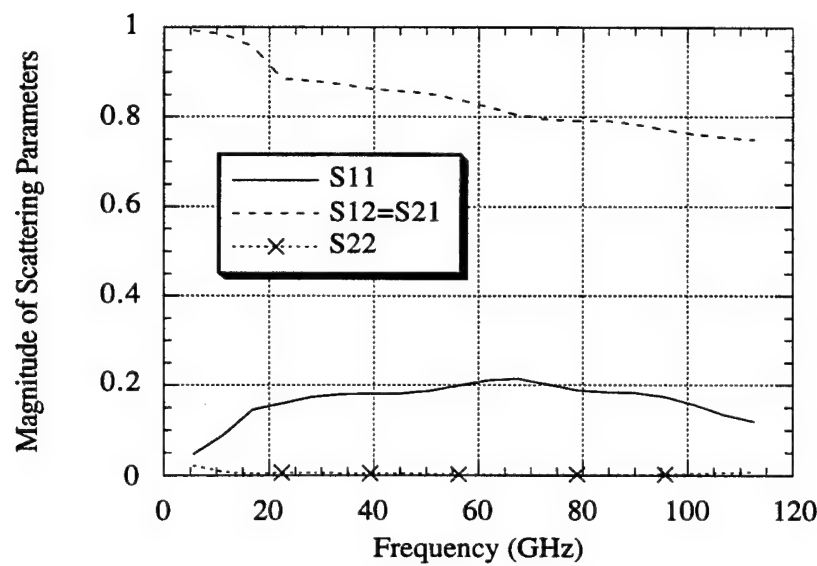


Figure 4.28 Magnitude of the scattering parameters as a function of frequency for the grounded coplanar waveguide to microstrip line transition.

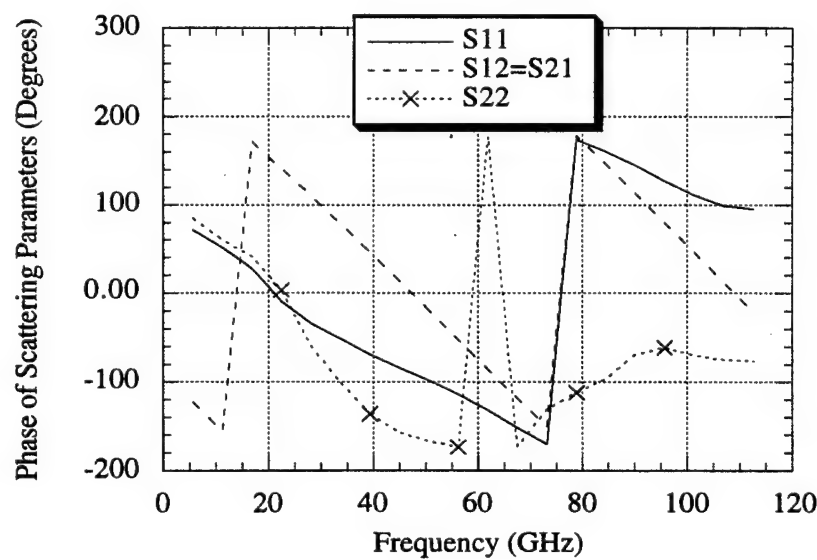


Figure 4.29 Phase of the scattering parameters as a function of frequency for the grounded coplanar waveguide to microstrip line transition.

A final interesting quantity to examine is the normalized power loss, which is given by

$$\text{Power Loss} = 1 - |S_{11}|^2 - |S_{21}|^2 \quad (4.10)$$

when the source is on the port-one side of the discontinuity. The normalized power loss is shown as a function of frequency in Fig. 4.30. The P1 in the legend refers to the source on the coplanar waveguide side, and the P2 refers to the source on the microstrip line side.

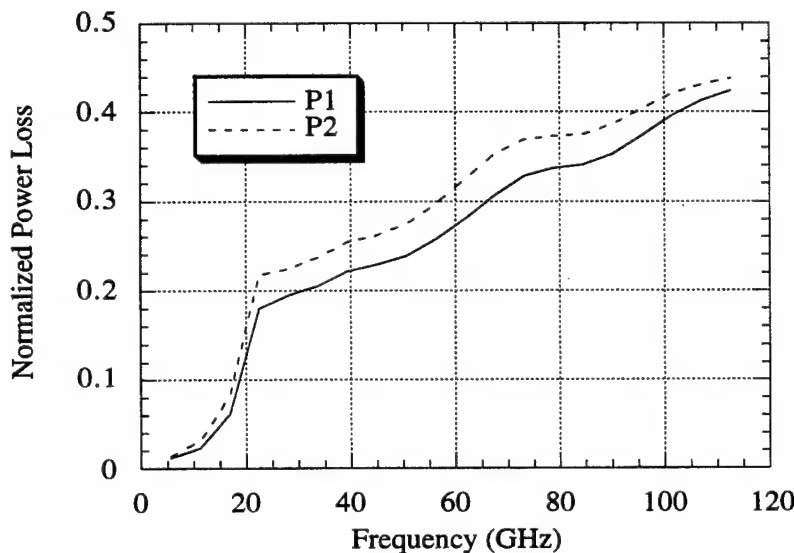


Figure 4.30 Normalized power loss as a function of frequency for the coplanar waveguide to microstrip line transition. P1 refers to the source on the coplanar waveguide side, and P2 refers to the source on the microstrip line side.

4.9 Conclusions

A variety of microstrip line and stripline structures were characterized in this chapter using the FDTD method. A technique based on Prony's method and transmission line equations was introduced, and demonstrated to characterize lines by extracting reflections from ABCs and to enable one to calculate scattering parameters of a two-port

system with a single FDTD simulation. Because of the expense of FDTD simulations in terms of memory and computation time, reducing the number and length of simulations is a worthwhile goal. A special update equation based on a triangular path of integration was introduced and shown to be a significant improvement over the conventional staircase method for approximating planar structures that do not directly correspond to the underlying Cartesian grid. Finally, the transition from grounded coplanar waveguide to microstrip line was investigated. Both the nonuniformity of the mesh and the Prony technique for scattering parameter extraction were important in this example. The grounded coplanar waveguide design presented very nearly achieves a match at 77 GHz. However, there is still significant power loss. While it is believed that a certain amount of power loss is inevitable due to the geometry of the discontinuity, perhaps the power loss could be abated through the use of a tuning stub on the coplanar waveguide.

4.10 References

- [4.1] M. Piket-May, A. Taflove, and J. Baron, "FD-TD modeling of digital signal propagation in 3-D circuits with passive and active loads," *IEEE Trans. Microwave Theory Tech.*, vol. 42, no. 8, pp. 1514-1523, August 1994.
- [4.2] X. Zhang, J. Fang, K. K. Mei, and Y. Liu, "Calculations of the dispersive characteristics of microstrips by the time-domain finite-difference method," *IEEE Trans. Microwave Theory Tech.*, vol. 36, no. 2, pp. 263-267, February 1988.
- [4.3] W. D. Becker, P. H. Harms, and R. Mittra, "Time-domain electromagnetic analysis of interconnects in a computer chip package," *IEEE Trans. Microwave Theory Tech.*, vol. 40, no. 12, pp. 2155-2163, December 1992.
- [4.4] J. Fang, "Absorbing boundary conditions applied to model wave propagation in microwave integrated circuits," *IEEE Trans. Microwave Theory Tech.*, vol. 42, no. 8, pp. 1506-1513, August 1994.
- [4.5] S. Kosanovich (private communication), May 1994.
- [4.6] X. Zhang and K. K. Mei, "Time-domain finite-difference approach to the calculation of the frequency-dependent characteristics of microstrip discontinuities," *IEEE Trans. Microwave Theory Tech.*, vol. 36, no. 12, pp. 1775-1787, December 1988.
- [4.7] TouchStone, EEsof, Inc., 5795 Lindero Canyon Rd., Westlake Village, CA 91362.

- [4.8] S. Kosanovich, "Numerical modeling of three-dimensional integrated circuit structures using full-wave, time domain, electromagnetic solution techniques," Ph.D. dissertation, University of Illinois at Urbana-Champaign, 1995.
- [4.9] K. C. Gupta, R. Garg, and I. J. Bahl, *Microstrip Lines and Slotlines*. Norwood, MA: Artech, 1979.
- [4.10] M. Muraguchi, T. Hirota, A. Minakawa, K. Ohwada, and T. Sugeta, "Uniplanar MMIC's and their applications," *IEEE Trans. Microwave Theory Tech.*, vol. 36, no. 12, pp. 1896-1901, December 1988.

CHAPTER 5

CHARACTERIZATION OF COUPLED MICROSTRIP LINES AND COUPLED STRIPLINES USING NONUNIFORM ORTHOGONAL FDTD

5.1 Introduction

Coupled microstrip lines and coupled striplines are used in the design of directional couplers, filters, impedance matching networks, baluns, and delay lines [5.1]. Coupled lines are also important in digital circuits where undesired crosstalk can occur when signal lines are brought into close proximity of each other [5.2]. There has been extensive work published in the area of coupled line analysis and design. A selected sample of some of this work is listed in the references, [5.3] - [5.11]. Various numerical methods have been employed in the study of coupled lines, including the even and odd mode method, the coupled mode formulation, the Green's function method, the variational method, Fourier-series expansion method, and the conformal mapping technique [5.4]. In [5.7] the spectral Galerkin procedure was used. Time domain models were developed in [5.6] and [5.8] - [5.10] utilizing quasi-TEM matrices. These methods require the solution of an eigenvector problem. The asymmetric coupled line case is defined and treated with the quasi-TEM approach in [5.10].

The purpose of this chapter is to use the full-wave solution provided by the FDTD method to characterize coupled microstrip lines and coupled striplines. First, the symmetric problem is considered and an even and odd mode theory is used in addition to the methods of Chapter 4 to characterize the lines. The methods of Chapter 4 are extended to handle the asymmetric case. This new method is presented, followed by numerical examples analyzing coupled symmetric and asymmetric lines. Where possible, FDTD results are compared with circuit simulator data. Finally, a multidielectric asymmetric coupled stripline problem is analyzed.

5.2 Symmetric Coupled Microstrip Lines

In this section, the symmetric coupled microstrip lines of Fig. 5.1 are analyzed using FDTD and the Prony technique described in Section 4.3. The lines are parallel and run in the z -direction. The width of each line is 300 μm and the separation between the lines is also 300 μm . The substrate below the infinitely thin lines is 250 μm thick and has a dielectric constant of 4.5.

The general N -line system supports N different modes. For this case, there are two lines, so there are two modes. Because of the symmetry of the structure, it is straightforward to determine the field distributions of the two modes, which can be referred to as the even and odd modes. For the even mode, the lines have the same voltage, whereas for the odd mode, the lines have voltages which are equal in magnitude but 180 degrees out of phase [5.1]. One approach for determining the effective dielectric constant and impedance of each mode is to model the coupled lines twice, once with an even mode excitation, and once with an odd mode excitation. Using voltage and current data, the effective dielectric constant and impedance are found as detailed in Chapter 4. Another approach is to use a symmetry plane between the lines. Again the problem is solved twice, once using a plane of perfect electric conductor for the odd mode, and once using a plane of perfect magnetic conductor for the even mode [5.11].

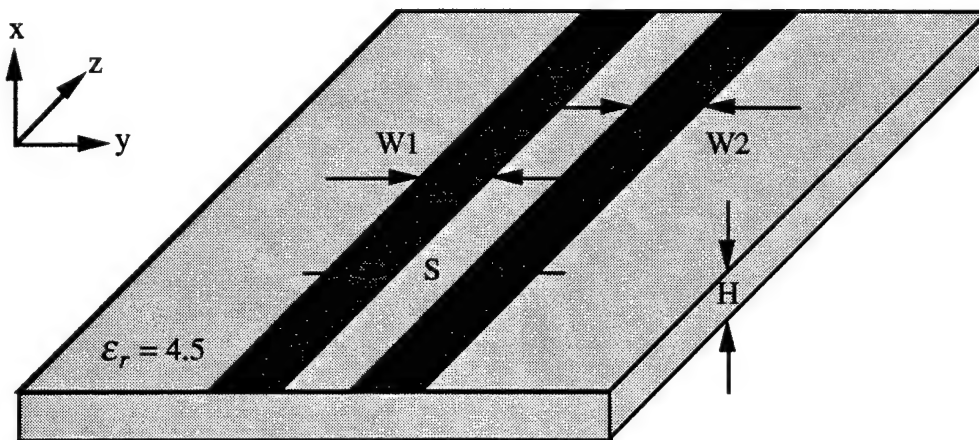


Figure 5.1 Geometry of coupled microstrip lines. For the symmetric case in this section, $S = W_1 = W_2 = 300 \mu\text{m}$. The substrate thickness, H , is 250 μm .

The method used in this work requires only one FDTD simulation. The lines are excited with an arbitrary voltage distribution, which by definition is a linear superposition of the even and odd mode field distributions [5.1]. For the example presented in this section, line 1 was excited and line 2 was not excited. Figure 5.2 shows the line current on line 1 at two positions on the line as a function of time. Position 1 is located 0.25 cm from the source and position 2 is 1.125 cm from the source. The amplitude of the current on line 1 decays as energy is coupled into line 2 as the voltage and current travel down the line. This phenomenon is clearly displayed in Fig. 5.3, which shows the line current on line 2 as a function of time. In Fig. 5.3 the amplitude of the current increases as the distance from the source increases.

The even and odd mode currents are given in (5.1) and (5.2).

$$I_{even} = (I_1 + I_2)/2.0 \quad (5.1)$$

$$I_{odd} = (I_1 - I_2)/2.0 \quad (5.2)$$

where I_1 and I_2 are the currents on line 1 and line 2, respectively. Equations (5.1) and (5.2) are valid in both the time domain and the frequency domain. The even mode

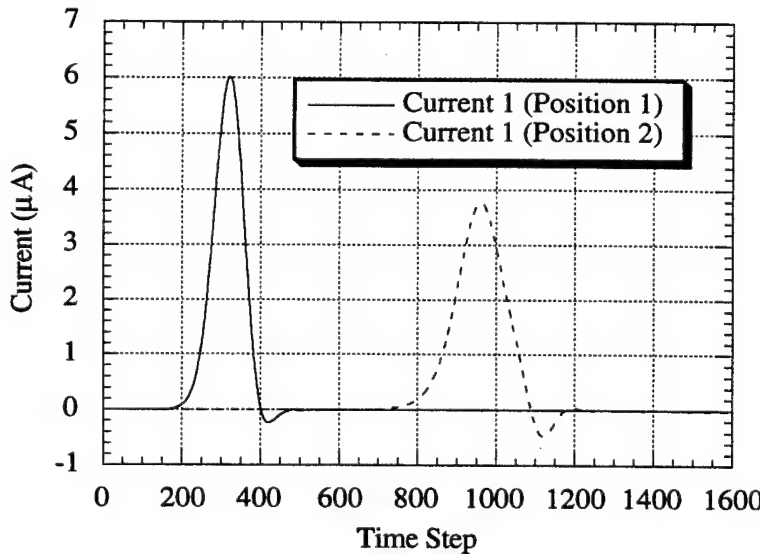


Figure 5.2 Line current on line 1 as a function of time. Position 1 and position 2 are 0.875 cm apart.

current was determined using (5.1), and is plotted as a function of time in Fig. 5.4. Equation (5.2) was used to calculate the odd mode current, which is shown in Fig. 5.5. Comparing Fig. 5.4 and Fig. 5.5, it is clear that the odd mode current propagates faster than the even mode current.

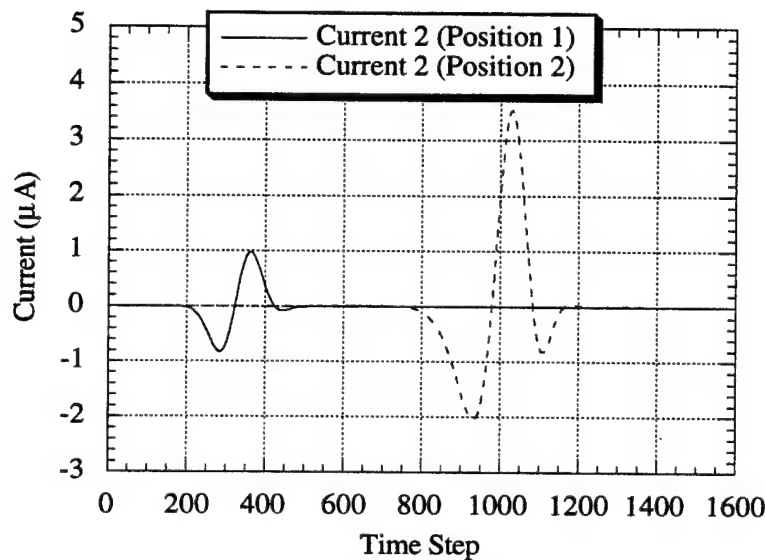


Figure 5.3 Line current on line 2 as a function of time. Position 1 and position 2 are 0.875 cm apart.

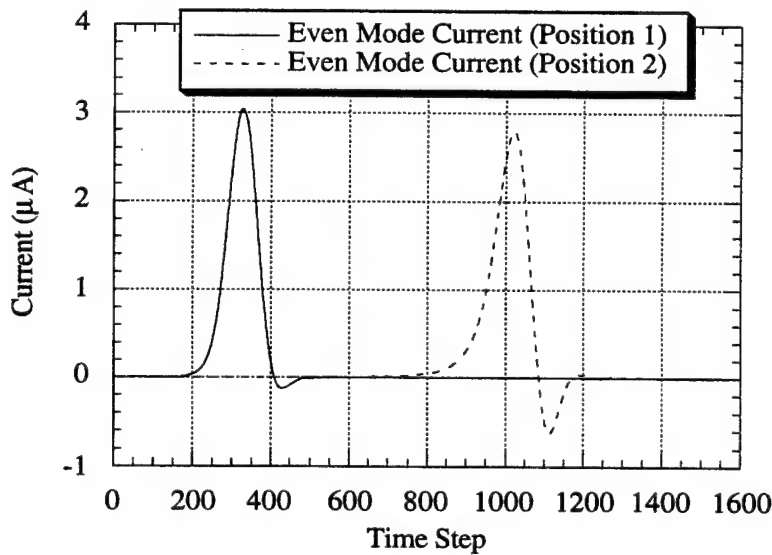


Figure 5.4 Even mode current as a function of time. Position 1 and position 2 are 0.875 cm apart.

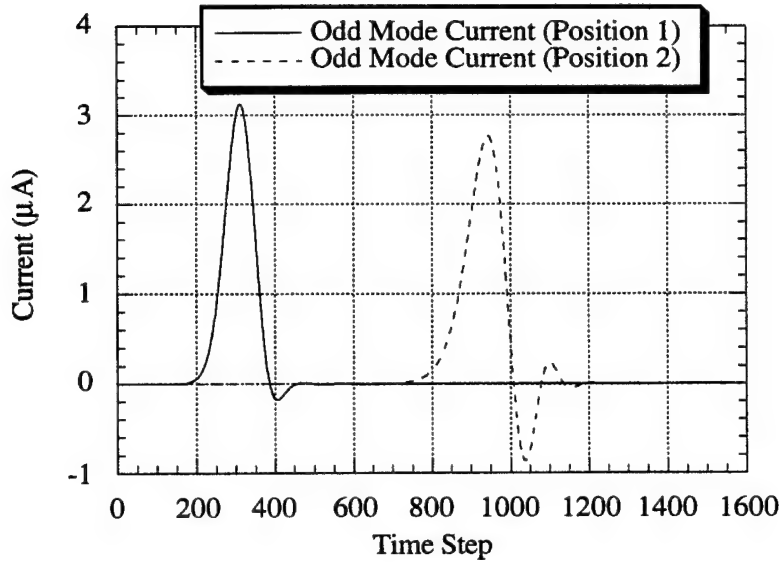


Figure 5.5 Odd mode current as a function of time. Position 1 and position 2 are 0.875 cm apart.

The effective dielectric constant and impedance are found using the procedure in Section 4.3, which takes into account the presence of reflections in the time domain data due to the ABCs. The even and odd mode effective dielectric constants are shown in Fig. 5.6. FDTD results are compared with results from the circuit simulator LINECALC [5.12]. The agreement for the odd mode is excellent. For the even mode, however, there is about a 4% difference between the FDTD and LINECALC values at the low frequency end of the graph. The difference is less than 3% at a frequency of 40 GHz. The impedance is plotted as a function of frequency in Fig. 5.7. Again, the FDTD results are compared with the LINECALC results. The agreement between the FDTD values and the LINECALC values is excellent. The impedance of a single isolated line as calculated using LINECALC is provided as a reference. At low frequencies, the even mode impedance is about 12% larger than the single line impedance. At high frequencies, the even mode impedance is about 15% larger than the single line impedance. The odd mode impedance is about 14% smaller than the single line impedance.

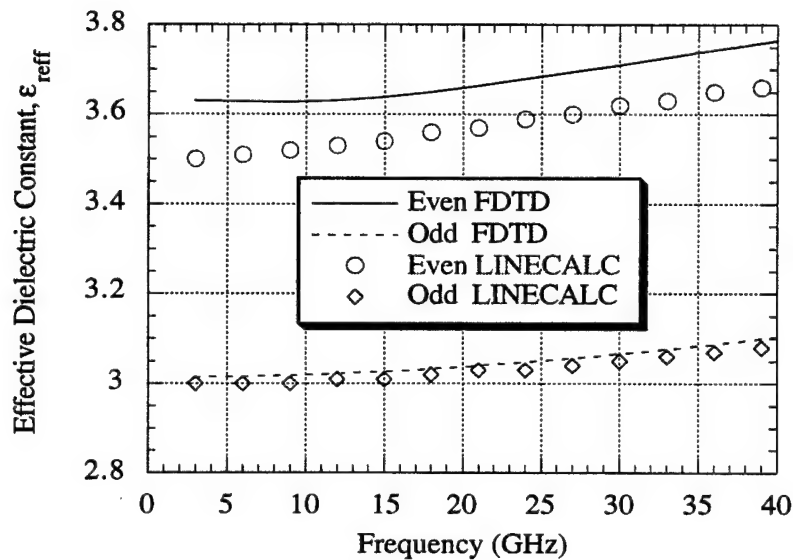


Figure 5.6 Effective dielectric constant as a function of frequency for the symmetric coupled microstrip lines in Fig. 5.1.

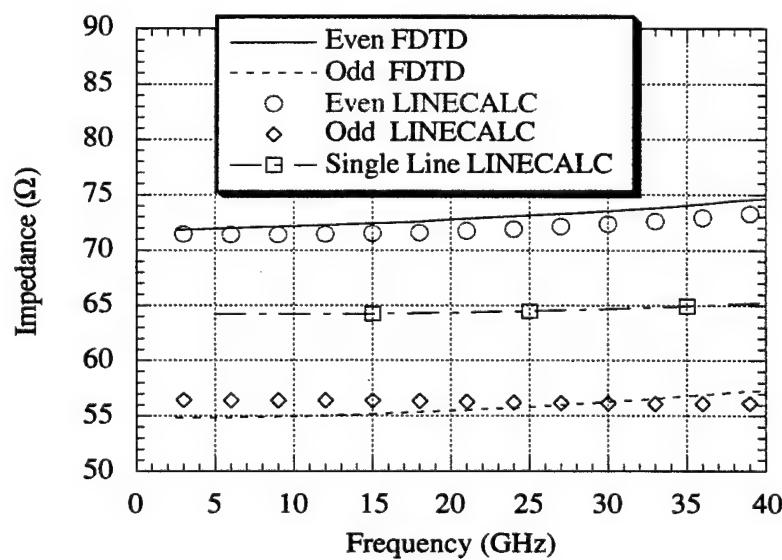


Figure 5.7 Even and odd mode impedances as functions of frequency for the symmetric coupled microstrip lines in Fig. 5.1.

5.3 Prony's Method for Mode Extraction

A new approach for mode extraction of coupled lines is presented in this section. Neglecting the reflections from the ABCs, the voltage on either line of a coupled two-line system can be written in terms of the modal voltages as

$$V(z) = A_1 e^{-\gamma_1 z} + A_2 e^{-\gamma_2 z} \quad (5.3)$$

where

$$\gamma_i = \alpha_i + j\beta_i \quad (5.4)$$

and A_i is the complex amplitude of the voltage mode. Similarly, an expression for the current is given in (5.5)

$$C(z) = B_1 e^{-\gamma_1 z} + B_2 e^{-\gamma_2 z} \quad (5.5)$$

where γ_i is defined in (5.4). There are six unknowns in (5.3) and (5.5), namely A_1 , A_2 , B_1 , B_2 , γ_1 , and γ_2 . Once these unknowns are determined, it is straightforward to calculate the modal effective dielectric constants and modal impedances.

The unknowns in (5.3) and (5.5) can be determined using Prony's method [5.13]. The following derivation will be based on the expression for the voltage in Equation (5.3). The voltage is monitored at four or more locations in the z -direction. These monitoring points should be equally spaced. The four time domain voltage responses are transformed to the frequency domain and written as V_0 , V_1 , V_2 , and V_3 . Equation (5.3) is rewritten as (5.6).

$$V(z) = A_1 u_1^z + A_2 u_2^z \quad (5.6)$$

The u_i are then given by

$$u_i = \frac{-\phi_1}{2} \pm \sqrt{\left(\frac{\phi_1}{2}\right)^2 - \phi_2} \quad (5.7)$$

where

$$\phi_1 = \frac{V_1 V_2 - V_0 V_3}{V_0 V_2 - V_1^2} \quad (5.8)$$

and

$$\phi_2 = \frac{V_2^2 - V_1 V_3}{V_1^2 - V_0 V_2} \quad (5.9)$$

and the two values of u_i are determined by the \pm operator in (5.7).

When applying this method, it is important that reflections from the ABCs are not present in the time domain data. Reflections can be avoided by simply making the problem long in the z-direction and stopping the simulation before reflections from the ABCs can contaminate the fields at the monitoring locations. This will reduce the number of points in the time domain which leads to coarser resolution in the frequency domain. For many applications, this is not a problem, since the frequency domain data are smooth and do not require fine resolution.

5.4 Coupled Microstrip Lines

The technique presented in the previous section will be demonstrated in this section to calculate the effective dielectric constant and impedance for the two modes of the coupled microstrip lines shown in Fig. 5.1. For this case, $W_1 = W_2 = 300 \mu\text{m}$, and $S = 50 \mu\text{m}$. Since the lines are close together, it is expected that the coupling effects will be greater than in the example in Section 5.2.

Line 1 was excited with a Blackman-Harris window function with a 3 dB cutoff frequency of 78.9 GHz and line 2 was not excited. The voltage and current were monitored along the coupled lines, transformed to the frequency domain, and used to calculate effective dielectric constants and impedances. Figure 5.8 shows the two modal effective dielectric constants and compares them with the even and odd effective dielectric constants calculated using LINECALC. The agreement between the LINECALC and FDTD values is excellent for the odd mode. For the even mode, the difference is only 1.3%. Even and odd mode impedances are shown in Fig. 5.9. The agreement for the even mode is excellent but the odd mode calculated using FDTD is considerably lower than the LINECALC impedance. Increasing the mesh density in the cross-section would improve the FDTD results. As in Fig. 5.7, the impedance of a single isolated line is shown for comparison with the even and odd mode impedances. As the lines are moved closer together, the coupling becomes stronger, and there is greater

deviation of the even and odd mode impedances from the characteristic impedance of the isolated line.

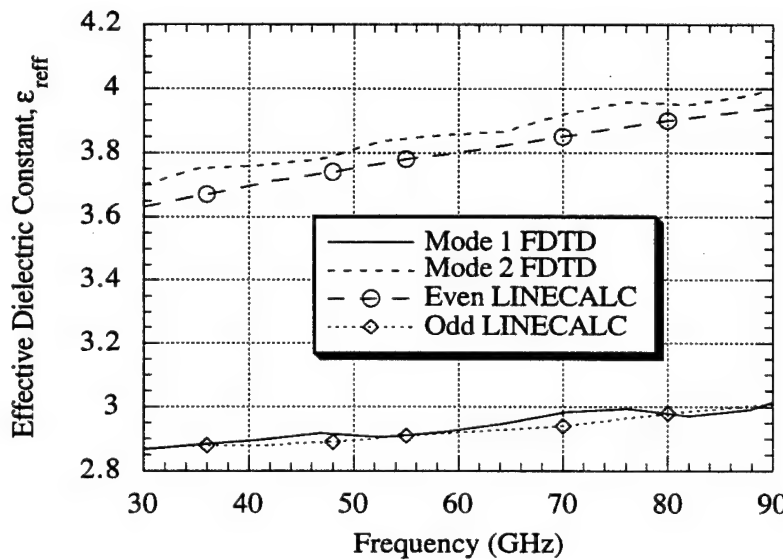


Figure 5.8 Effective dielectric constant as a function of frequency for symmetric coupled microstrip lines with $S = 50 \mu\text{m}$.

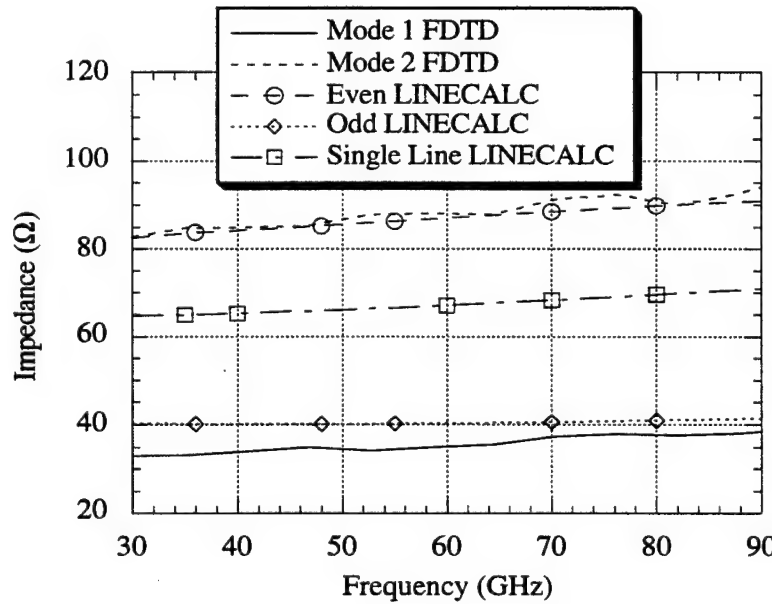


Figure 5.9 Even and odd mode impedances as functions of frequency for symmetric coupled microstrip lines with $S = 50 \mu\text{m}$.

5.5 Asymmetric Coupled Microstrip Lines

Consider the geometry shown in Fig. 5.1. If $W_1 \neq W_2$, the method presented in Section 5.2 for calculating the modal effective dielectric constants and impedances cannot be used. However, the method presented in Section 5.3 can be used. Numerical results will be presented for asymmetric coupled lines with $W_1 = 300 \mu\text{m}$, $W_2 = 200 \mu\text{m}$, and $S = 50 \mu\text{m}$. Line 1 was excited and energy coupled into line 2. The voltage and current were monitored at several equally spaced sampling locations along the lines. Effective dielectric constants and impedances were then calculated, as described in the previous section.

Figure 5.10 shows the effective dielectric constant as a function of frequency. Values from the FDTD simulation are compared to values from LINECALC. Since LINECALC does not solve the asymmetric case, two sets of LINECALC data are shown. One set is for symmetric lines with width, $W = 300 \mu\text{m}$, and separation, $S = 50 \mu\text{m}$. These data are labeled "Even 300" and "Odd 300" in the graph legend in Fig. 5.10. The "Even 200" and "Odd 200" labels refer to LINECALC results for symmetric lines with width, $W = 200 \mu\text{m}$, and separation, $S = 50 \mu\text{m}$. As shown in Fig. 5.10, the values of the effective dielectric constant for mode 1 from the FDTD simulation are between those from the LINECALC calculations. This is the expected result. If it is assumed that FDTD values for mode 2 are slightly larger than they should be, as was the case in Fig. 5.6 and Fig. 5.8, the FDTD data are consistent with the results from LINECALC.

Modal impedance values are displayed in Figs. 5.11 and 5.12 for line 1 and line 2, respectively. The FDTD values are very reasonable, with the exception of mode 1 on line 1, which is most likely smaller than it should be. However, the overall results suggest that the approach presented in Section 5.3 is a good method for characterizing asymmetric coupled microstrip lines.

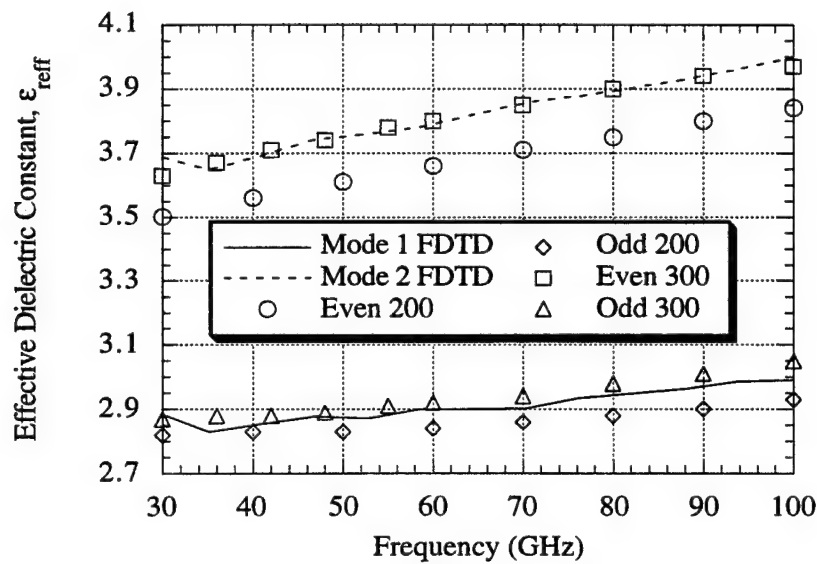


Figure 5.10 Even and odd mode effective dielectric constants as functions of frequency for asymmetric coupled microstrip lines with $W_1 = 300 \mu\text{m}$, $W_2 = 200 \mu\text{m}$, and $S = 50 \mu\text{m}$. The FDTD results are compared with circuit simulator results for symmetric coupled lines with a separation of $50 \mu\text{m}$.

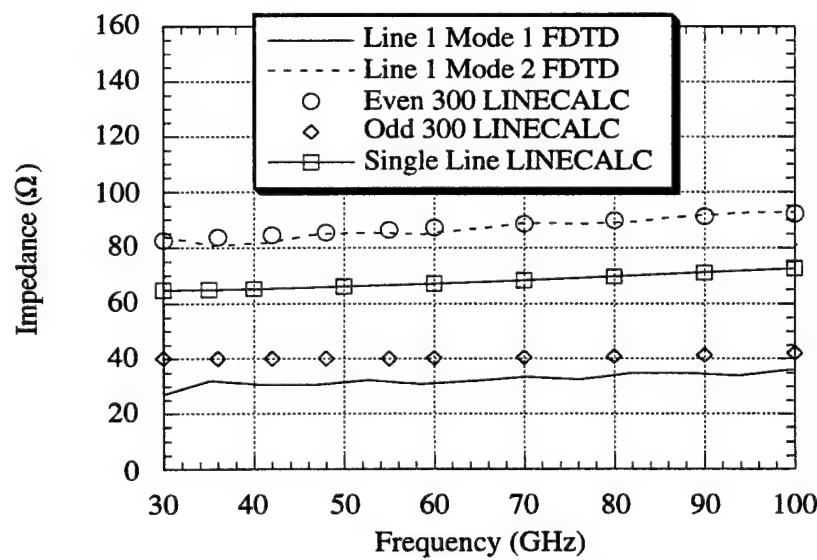


Figure 5.11 Impedance as a function of frequency for asymmetric coupled lines. The modal impedances calculated on line 1 ($W_1 = 300 \mu\text{m}$) are compared with circuit simulator results for symmetric coupled microstrip lines with width $300 \mu\text{m}$. The single line result shows the impedance of an isolated line with width $300 \mu\text{m}$.

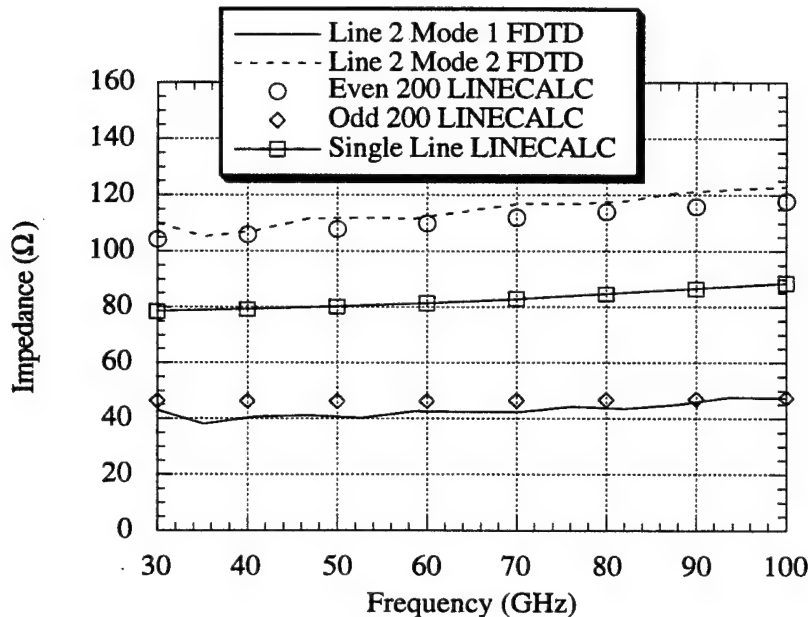


Figure 5.12 Impedance as a function of frequency for asymmetric coupled microstrip lines. The modal impedances calculated on line 2 are compared with circuit simulator results for the symmetric case with $W = 200 \mu\text{m}$. The single line result shows the impedance of an isolated line with width $200 \mu\text{m}$.

5.6 Asymmetric Coupled Striplines

The previous sections in this chapter dealt with the analysis of coupled microstrip lines, and FDTD results were compared with results from LINECALC. In this section, the effective dielectric constant of asymmetric coupled striplines will be determined. LINECALC results are not available for this structure because of the asymmetry and variation of the dielectric. The geometry is shown in Fig. 5.13, where $W_1 = 300 \mu\text{m}$, $W_2 = 200 \mu\text{m}$, $S = 50 \mu\text{m}$, $H_1 = H_2 = 250 \mu\text{m}$, and the top and bottom layers of the dielectric have dielectric constants of 2.2 and 4.5, respectively. In order to extract the effective dielectric constant for the asymmetric coupled striplines, line 1 is excited with a Blackman-Harris window function with a 3 dB cutoff frequency of 45.6 GHz and line 2 is left unexcited. Figure 5.14 shows the line current on line 1 as a function of time. The amplitude of the current decays as energy is coupled into line 2. This is shown in

Fig. 5.15, where the amplitude of the line current on line 2 increases as the monitoring location moves farther away from the source.

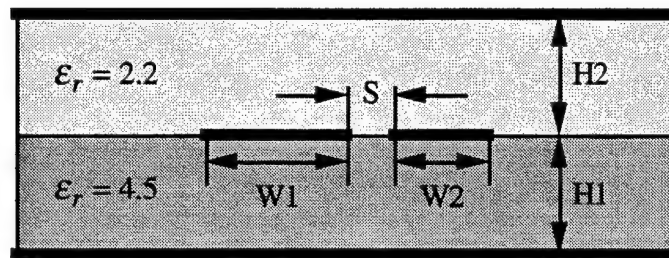


Figure 5.13 Geometry of asymmetric coupled striplines. $W_1 = 300 \mu\text{m}$, $W_2 = 200 \mu\text{m}$, $S = 50 \mu\text{m}$, and $H_1 = H_2 = 250 \mu\text{m}$.

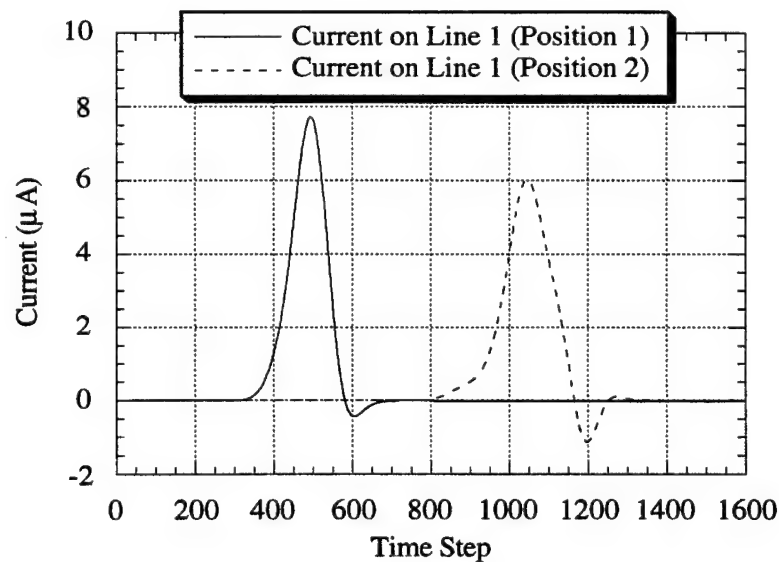


Figure 5.14 Line current on line 1 for the asymmetric coupled stripline in Fig. 5.13. Position 1 and position 2 are 0.750 cm apart.

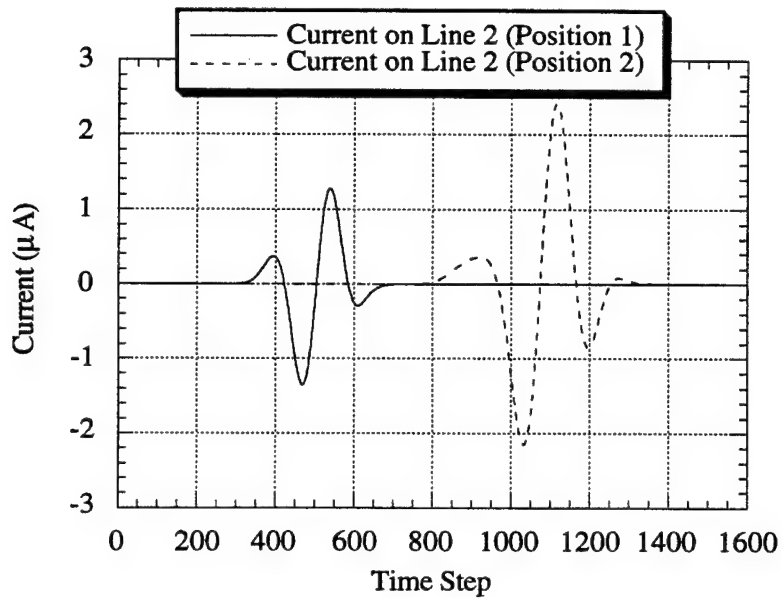


Figure 5.15 Line current on line 2 for the asymmetric coupled stripline in Fig. 5.13. Position 1 and position 2 are 0.750 cm apart.

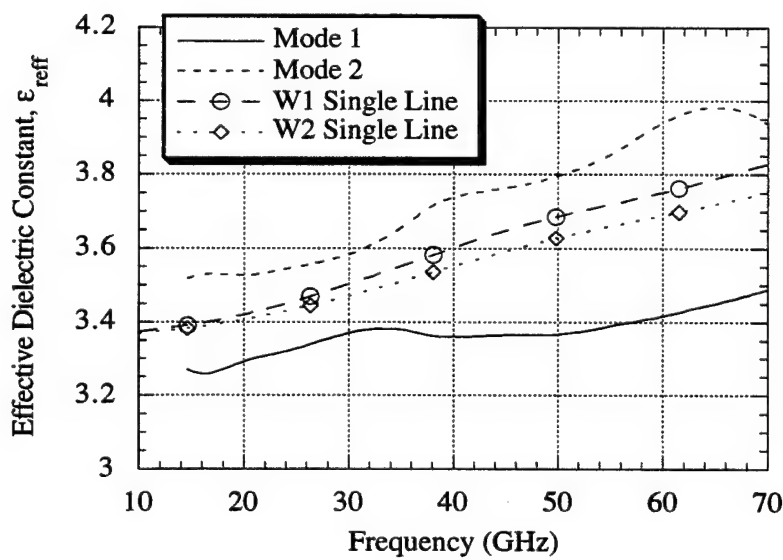


Figure 5.16 Effective dielectric constant as a function of frequency for the asymmetric coupled stripline in Fig. 5.13. The modal effective dielectric constants are compared with the effective dielectric constants of the isolated stripline embedded in the mixed dielectric. $W_1 = 300 \mu\text{m}$, and $W_2 = 200 \mu\text{m}$.

The effective dielectric constant is plotted as a function of frequency in Fig. 5.16. The two modal effective dielectric constants are compared to the effective dielectric constants for single isolated striplines of widths 300 μm and 200 μm , respectively. Since LINECALC results are not available, FDTD results for the isolated lines are used to compare with the modal results. As is the case with microstrip lines, the modal effective dielectric constants are greater than and less than the effective dielectric constant for the single line case. This type of behavior suggests that these results are reasonable.

5.7 Conclusions

Coupled microstrip lines and coupled striplines were analyzed in this chapter. The FDTD method was used in conjunction with techniques based on Prony's method to calculate modal effective dielectric constants and impedances with a single FDTD simulation. Moreover, the new approach presented was not dependent upon the symmetry of the lines. Numerical results for symmetric and asymmetric lines were presented and compared with results from LINECALC. An asymmetric coupled stripline problem with mixed dielectric substrate was analyzed, and the coupled results were compared with single line results obtained using FDTD since problems with layered dielectrics cannot be modeled using LINECALC. The results from the method presented were shown to be acceptable. The method could be further improved to account for the modal reflections due to the ABCs. This would require determining the roots of a fourth-order polynomial rather than the roots of a quadratic. Another possible avenue of research would be to use the pencil of functions method [5.14] to set up the eigenvector problem for the general coupled N-line system.

5.8 References

[5.1] H. B. Bakoglu, *Circuits, Interconnections, and Packaging for VLSI*. Reading, MA: Addison-Wesley, 1990.

- [5.2] K. C. Gupta, R. Garg, and R. Chadha, *Computer-Aided Design of Microwave Circuits*. Dedham, MA: Artech House, 1981.
- [5.3] R. Jansen, "High-speed computation of single and coupled microstrip parameters including dispersion, high-order modes, loss and finite strip thickness," *IEEE Trans. Microwave Theory Tech.*, vol. 26, no. 2, pp. 75-82, February 1978.
- [5.4] R. Garg and I. J. Bahl, "Characteristics of coupled microstriplines," *IEEE Trans. Microwave Theory Tech.*, vol. 27, no. 7, pp. 700-705, July 1979.
- [5.5] J. H. Hinton, "On design of microstrip lines," *IEEE Trans. Microwave Theory Tech.*, vol. 28, no. 3, p. 272, March 1980.
- [5.6] J. E. Schutt-Aine and R. Mittra, "Analysis of pulse propagation in coupled microstrip lines," *IEEE Trans. Circuits & Syst.*, vol. 32, pp. 1214-1219, December 1985.
- [5.7] E. G. Farr, C. C. Chan, and R. Mittra, "A frequency-dependent coupled-mode analysis of multiconductor microstrip lines with application to VLSI interconnection problems," *IEEE Trans. Microwave Theory Tech.*, vol. 34, no. 2, pp. 307-310, February 1986.
- [5.8] F. Romeo and M. Santomauro, "Time-domain simulation of n coupled transmission lines," *IEEE Trans. Microwave Theory Tech.*, vol. 35, no. 2, pp. 131-136, February 1987.
- [5.9] G. Ghione, I. Maio, and G. Vecchi, "Modeling of multiconductor buses and analysis of crosstalk, propagation delay, and pulse distortion in high-speed GaAs logic circuits," *IEEE Trans. Microwave Theory Tech.*, vol. 37, no. 3, pp. 445-456, March 1989.
- [5.10] G. G. Gentili and M. Salazar-Palma, "The definition and computation of modal characteristic impedance in quasi-TEM coupled transmission lines," *IEEE Trans. Microwave Theory Tech.*, vol. 43, no. 2, pp. 338-343, February 1995.
- [5.11] W. D. Becker, P. H. Harms, and R. Mittra, "Time-domain electromagnetic analysis of interconnects in a computer chip package," *IEEE Trans. Microwave Theory Tech.*, vol. 40, no. 12, pp. 2155-2163, December 1992.
- [5.12] LINECALC, EEsof, Inc., 5795 Lindero Canyon Rd., Westlake Village, CA 91362.
- [5.13] S. L. Marple, *Digital Spectral Analysis with Applications*. Englewood Cliffs, NJ: Prentice-Hall, 1987.
- [5.14] Y. Hua and T. K. Sarkar, "Generalized pencil-of-function method for extracting poles of an EM system from its transient response," *IEEE Trans. Antennas Propagat.*, vol. 37, no. 2, pp. 229-234, February 1989.

CHAPTER 6

ANALYSIS OF MICROSTRIP ANTENNAS USING FDTD

6.1 Introduction

The FDTD method has been applied to analyze a variety of radiating microstrip and wire structures [6.1]-[6.10]. The main advantage of the FDTD method over moment method techniques for complex geometries is that the preprocessing required for FDTD is virtually negligible when compared to the preprocessing required to derive and implement the requisite Green's functions for the method of moments. In this chapter, the near-field to far-field transformation is discussed, followed by the analysis of a complicated balun-fed folded dipole antenna. Next the benefits of using the nonuniform orthogonal FDTD method are demonstrated through the analysis of microstrip patch antennas. The results obtained are compared with experimental measurements.

6.2 Near-field to Far-field Transformation

There are several methods for obtaining far-field patterns from near-field data in an FDTD simulation [6.11]-[6.13]. The method reported in [6.13] provides frequency results over a wide band, but requires an exorbitant amount of memory to store entire time signatures at the observation locations. In this work, the method reported in [6.11] was implemented. It is a single frequency method that is not expensive in terms of memory requirements as compared to the method in [6.13]. A brief summary of the procedure in [6.11] is presented here.

To determine the radiation pattern or far-field data for a general radiator or scatterer, one typically approaches the problem by solving for the currents on the surface of the radiator. The currents are then transformed to the far field using a Fourier transform. However, when the radiator is a complex geometry containing multiple layers of dielectric and metallization in both the vertical and horizontal directions, it is

extremely difficult to derive an accurate Green's function, which is required in order to solve for the currents. This is not a difficulty for the FDTD method, which solves for the fields everywhere within the computational volume. Therefore, Huygens' Equivalence Principle can be applied in a straightforward manner. The radiator is enclosed by an equivalent surface as shown in Fig. 6.1. The tangential electric and magnetic fields on the surface are used to calculate the equivalent electric and magnetic surface currents. Electric and magnetic potentials are calculated from the currents as shown in Equation (6.1).

$$\begin{bmatrix} \vec{A} \\ \vec{F} \end{bmatrix} = \left(\frac{e^{-jk_o r}}{4\pi r} \right) \iint_{S_a} \begin{bmatrix} \vec{J} \\ \vec{M} \end{bmatrix} e^{-jk_o r' \cos \xi} ds'_a \quad (6.1)$$

where $r' \cos \xi = (x' \cos \phi + y' \sin \phi) \sin \theta + z' \cos \theta$. Expressions for the far field are determined using the simple free-space Green's function. The integration is carried out numerically by a straightforward summation.

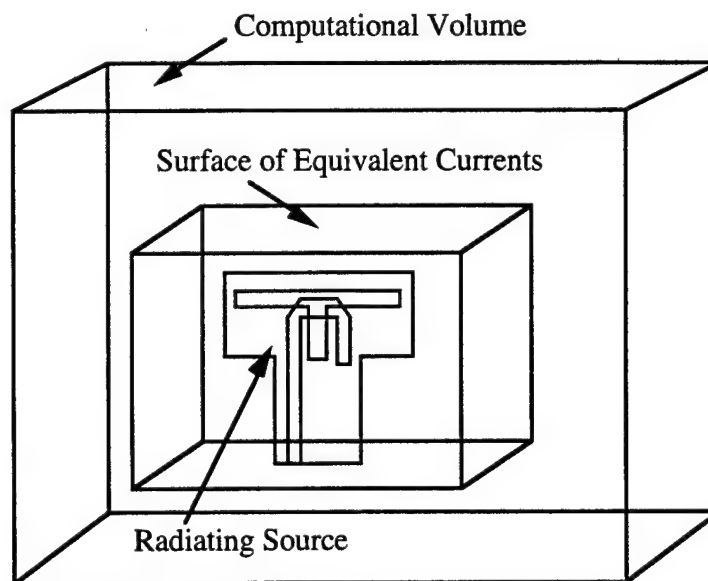


Figure 6.1 Schematic representation of radiating source surrounded by equivalent sources.

The electric field components E_θ and E_ϕ are then given by Equations (6.2) and (6.3)

$$E_\theta = (-jk_o\eta_o) \left[A_\theta + \frac{F_\phi}{\eta_o} \right] \quad (6.2)$$

$$E_\phi = (-jk_o\eta_o) \left[A_\phi - \frac{F_\theta}{\eta_o} \right] \quad (6.3)$$

where η_o is the intrinsic impedance of free space. It should be noted that the expressions in (6.1) - (6.3) are written in the frequency domain. Since FDTD is a time domain method, the magnitude and phase of the surface currents are determined by assuming that fields have settled to the steady-state solution. The maximum and minimum values of the field or current at a given location on the equivalent surface are determined by searching the data and the slope of the data as time progresses. However, the entire time signature is not stored. Only three time points are required per field location.

6.3 Balun-Fed Folded Dipole

The objectives of the work presented in this section are to use the FDTD method to calculate the standing wave ratio as a function of frequency, and to calculate far-field radiation patterns at several frequencies, for the balun-fed folded dipole designed and tested by Proudfoot [6.14]. Advantages of the balun-fed folded dipole were reported in [6.14] and will be summarized here. The balun-fed folded dipole combines the moderate bandwidth of the folded dipole with the double tuning capabilities of the balun to provide a significant increase in bandwidth compared to that of conventional microstrip patches. The high impedance of the folded dipole leads to a narrow microstrip line feed, which is important from the fabrication standpoint. Low impedances lead to wide lines, which in certain instances are actually wider than the radiating element. A final advantage of the balun-fed folded dipole is that its endfire properties and shielding ground plane make it attractive for use in arrays.

The balun-fed folded dipole antenna shown in Figs. 6.2 and 6.3 is a fairly complicated structure. A “tee” shape is etched away from copper forming the conducting arms of the folded dipole. The length of the folded dipole is 3.048 cm, the width of the top arm is 0.1016 cm, the width of the bottom arm is 0.3810 cm, and the etched gap separating the arms is 0.0508 cm. The dipole is excited with a 0.1151 cm wide microstrip-line balun feed. The copper of the folded dipole extends towards the source, is three times as wide as the microstrip line, and serves as the ground for the feeding microstrip line. The etched slot parallel to the feed line has the same width as the feed line. The dipole and the feeding line are separated by a dielectric with a thickness of 0.16 cm and relative permittivity equal to 4.4. The microstrip line is impedance matched at the orthogonal ground plane, which has a hole in it. The orthogonal ground plane is 40.64 cm by 40.64 cm, and located at the $z = 0$ plane, 2.027 cm from the center of the folded dipole. These physical dimensions are found in [6.14], and some are from measurements of an element at the Rome Laboratory, Hanscom Air Force Base. There is some uncertainty associated with the dimensions determined by measurement because the measured element was a prototype.

Examining the time signature of the voltage gives a physical picture of the effects of the discontinuities. Figure 6.4 shows the voltage under the microstrip line at $z = -1.0$ cm and $z = 0.5$ cm. The effects of the hole in the orthogonal ground plane and the antenna are shown in Fig. 6.4(a). There is a peak in the voltage response due to the hole at time step 400. Later, at approximately time step 850, the reflection caused by the antenna is seen. Figure 6.4(b) shows that there is a difference between the uniform line case and the antenna case before the discontinuity of the antenna is encountered because of the hole in the orthogonal ground plane. This agrees with the results in Fig. 6.4(a).

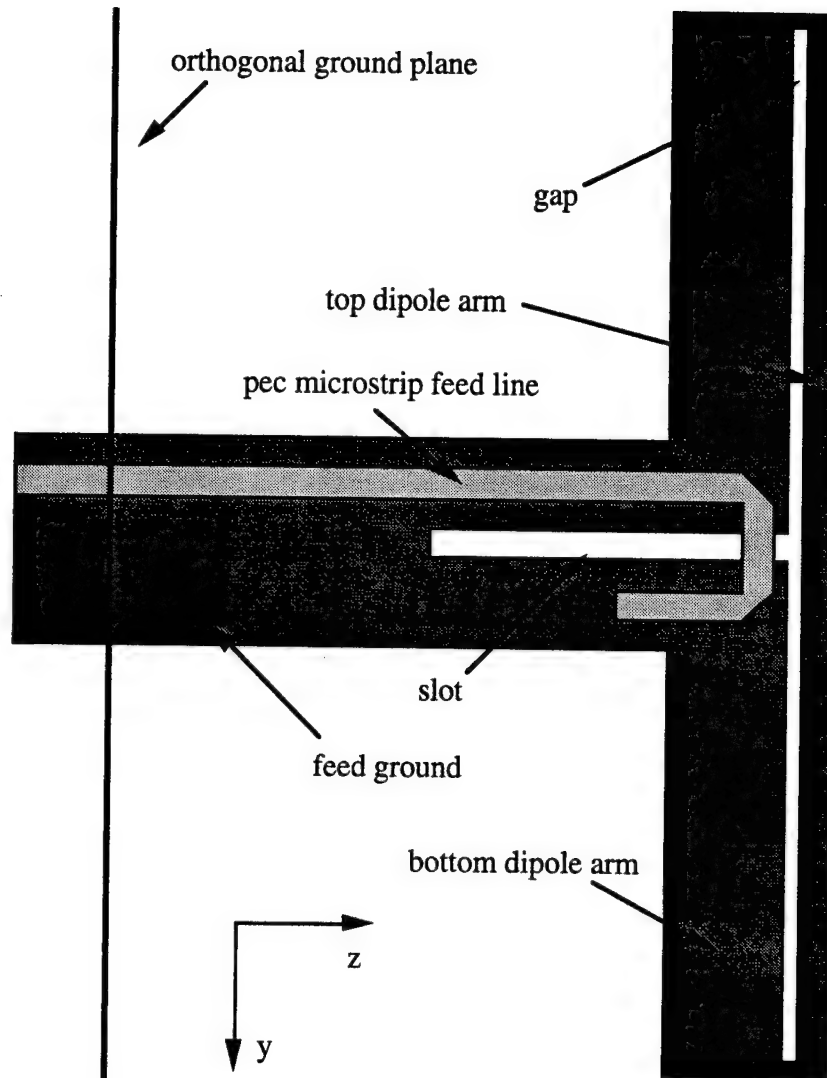
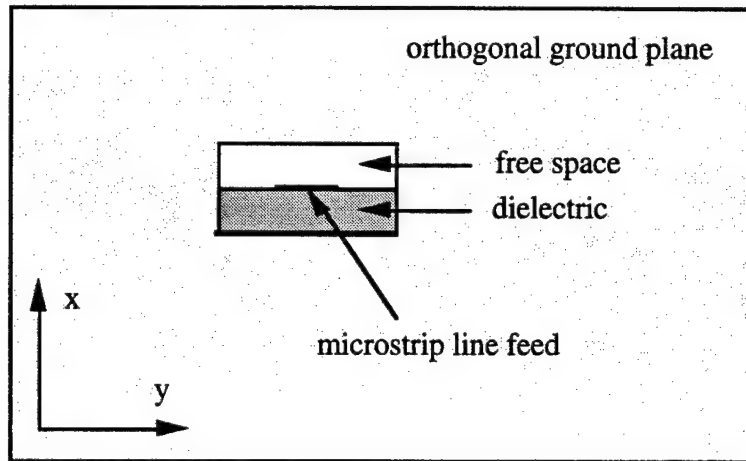
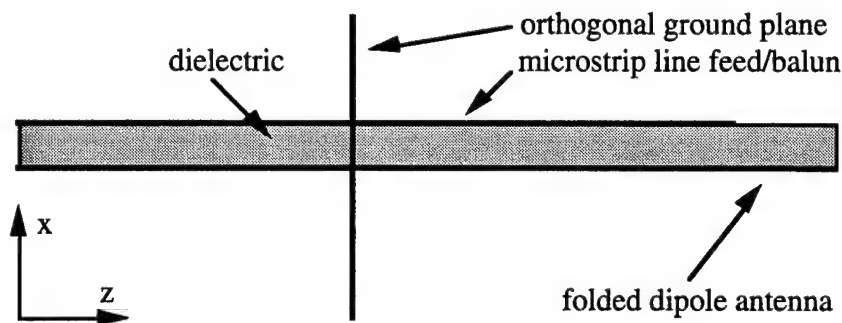


Figure 6.2 Balun-fed folded dipole antenna. A layer of dielectric material separates the microstrip line feed from the folded dipole. The folded dipole is an extension of the ground for the feed. A hole in the orthogonal ground plane allows the microstrip line to pass through.

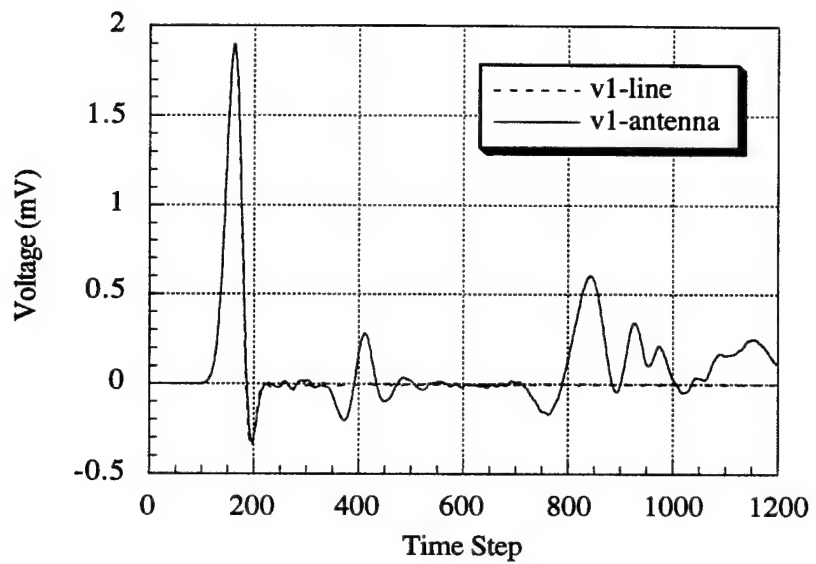


(a)

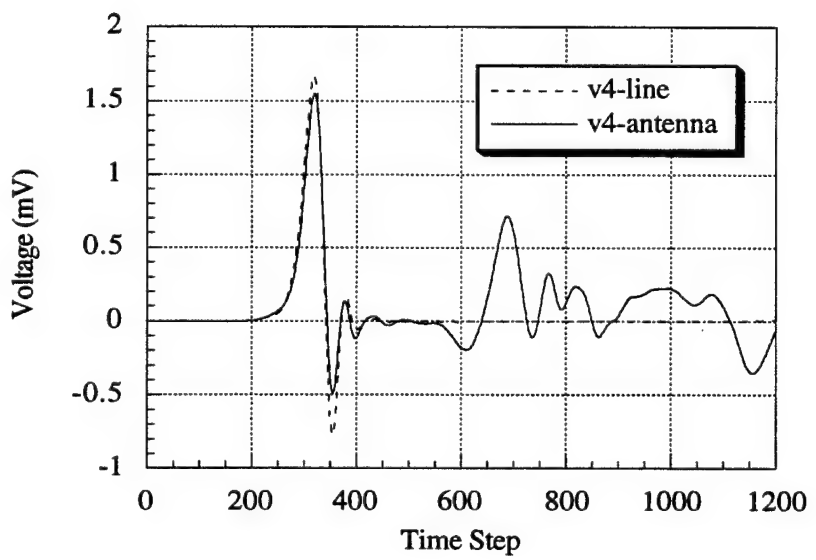


(b)

Figure 6.3 Cross-sections of the balun-fed folded dipole antenna. (a) The x-y plane. (b) The x-z plane.



(a)



(b)

Figure 6.4 Voltage along the microstrip feed line as a function of time. (a) At $z = -1.0$ cm. (b) At $z = 0.5$ cm.

The SWR was calculated by first subtracting the time signature of the voltage of the uniform line from the time signature of the voltage of the balun-fed folded dipole with an orthogonal ground plane and calling this the reflected voltage. Next, the reflected voltage and the incident voltage (the voltage of the uniform line) were transformed to the frequency domain via the fast Fourier transform. The magnitude of the SWR was then computed with the following formula:

$$SWR = \left(1 + \frac{|V_{refl}|}{|V_{inc}|} \right) \Bigg/ \left(1 - \frac{|V_{refl}|}{|V_{inc}|} \right) \quad (6.4)$$

The SWR was also computed using the magnitudes of the incident and reflected currents rather than the magnitudes of the incident and reflected voltages in Equation (6.4).

In Fig. 6.5, the SWR computed using the FDTD method is compared to the measurements and theory reported in [6.14]. The FDTD voltages and currents were monitored at $z = 0.0$ cm. Circles labeled FDTD voltage and FDTD current indicate that the SWR was computed using either voltage or current. The results from the FDTD method appear to capture the general trend of the measured response; however, the agreement is not that good. This is likely due to the fact that several defining features of the feed and the dipole were approximated.

When applying this method to the balun-fed folded dipole with an orthogonal ground plane, a key point is that the equivalent surface totally encloses the radiating element. This presents a problem since the mesh used for calculating radiation patterns has a discretization of $\Delta x = 0.04$ cm, $\Delta y = 0.03$ cm, and $\Delta z = 0.05$ cm. Since the orthogonal ground plane has physical dimensions of 40.64 cm by 40.64 cm, the mesh would have to be more than 1,016 cells in the x-direction and more than 1,355 cells in the y-direction. These numbers are each an order of magnitude too large for computers with 128 MB of RAM. However, by truncating the mesh in the x- and y-directions, so that the orthogonal ground plane extends to the edge of the mesh in the x- and y-directions, the ground plane appears to be of infinite extent as far as the mesh is concerned.

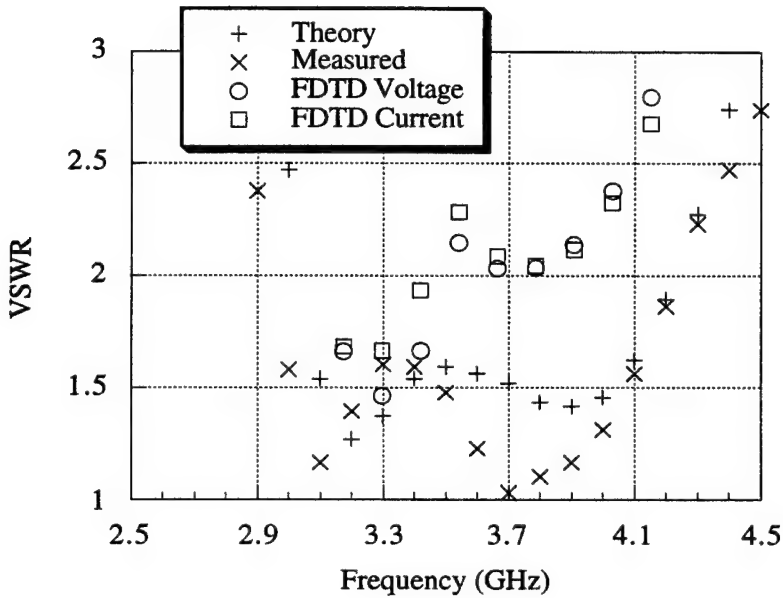
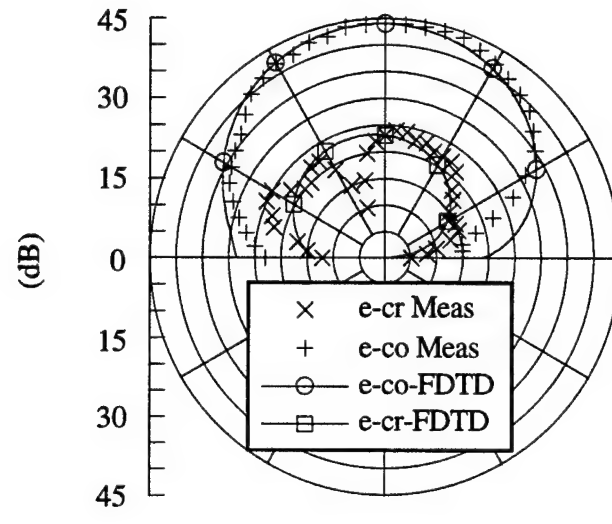


Figure 6.5 Standing-wave ratio of the balun-fed folded dipole. FDTD calculation with reference plane at $z = -0.5$ cm.

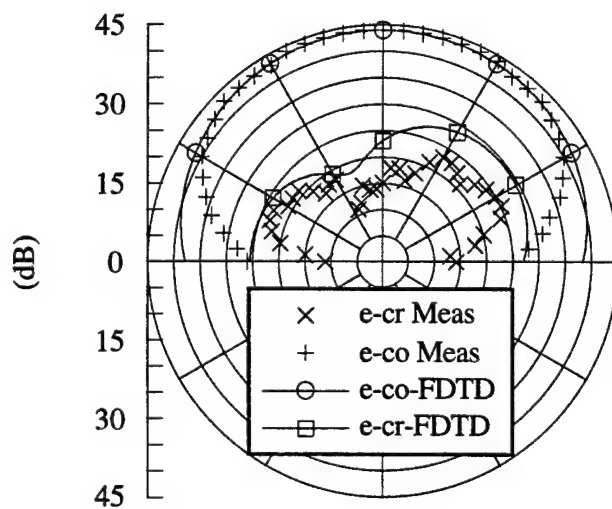
Although this model does prevent electric fields from propagating around a finite perfectly conducting plane, it will not lead to correct radiation patterns in the lower half plane because the equivalent surface that attempts to surround the radiator does not totally enclose it. Instead, the orthogonal ground plane intersects the equivalent surface and introduces undesirable effects for angles near grazing. However, it does provide a useful approximation for the far field in the upper half plane.

Radiation patterns comparing the co-polarized and cross-polarized fields with measurements [6.14] for single frequency excitations are shown in Figs. 6.6 and 6.7. In Fig. 6.6, the frequency of excitation was 3.7 GHz; there is good agreement between the FDTD results and the measurements, although the FDTD cross-polarized field does miss a null. Figure 6.7 compares the radiation patterns of the measurements at 3.7 GHz and the FDTD simulation at 3.4 GHz. The agreement between the FDTD results and measurements is better at this frequency than in Fig. 6.6. Overall, the agreement between

the measurements and the FDTD results is very good considering that the numerical model has a much smaller orthogonal ground plane than the structure that was measured.

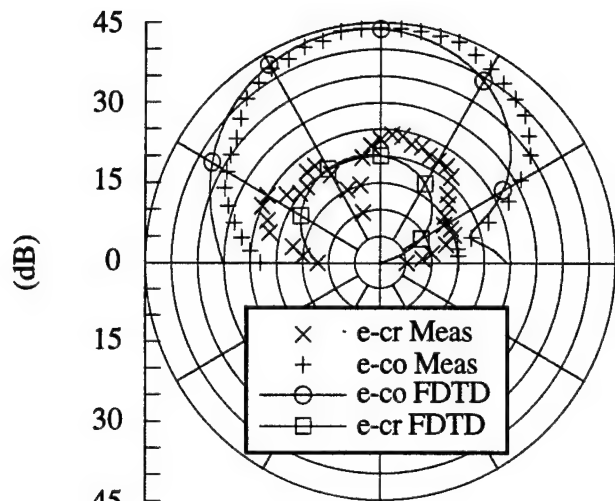


(a)

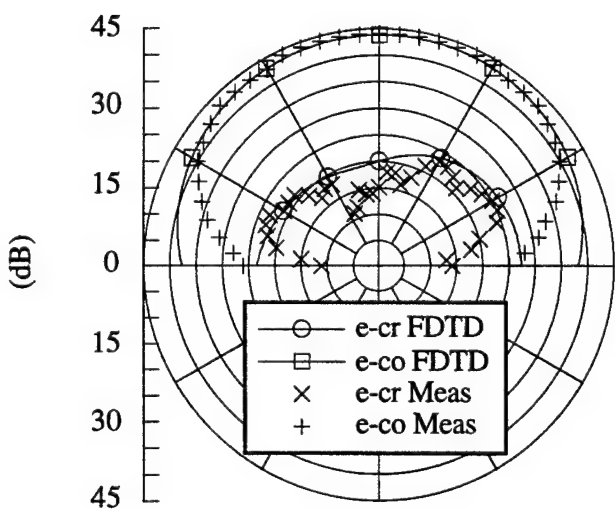


(b)

Figure 6.6 Radiation patterns at frequency 3.7 GHz. Co-polarized field is labeled e-co. Cross-polarized field is labeled e-cr. (a) E-plane. (b) H-plane.



(a)



(b)

Figure 6.7 Radiation patterns. Measurements are at frequency 3.7 GHz, and FDTD results are at 3.4 GHz. Co-polarized field is labeled e-co. Cross-polarized field is labeled e-cr. (a) E-plane. (b) H-plane.

6.4 Microstrip-Line Fed Patch Antenna

A microstrip-line fed patch antenna was built and measured. S_{11} and a radiation pattern are calculated using the FDTD model, and the results are compared with measurements. The antenna, shown in Fig. 6.8, is center fed and has a finite ground plane. The presence of the finite ground plane makes this problem well-suited for FDTD, whereas moment method techniques have difficulty handling the finite ground plane when calculating the radiation pattern. Measurements of S_{11} were performed on the HP8510 network analyzer. TRL standards, shown in Fig. 6.9, were built and used to calibrate the network analyzer.

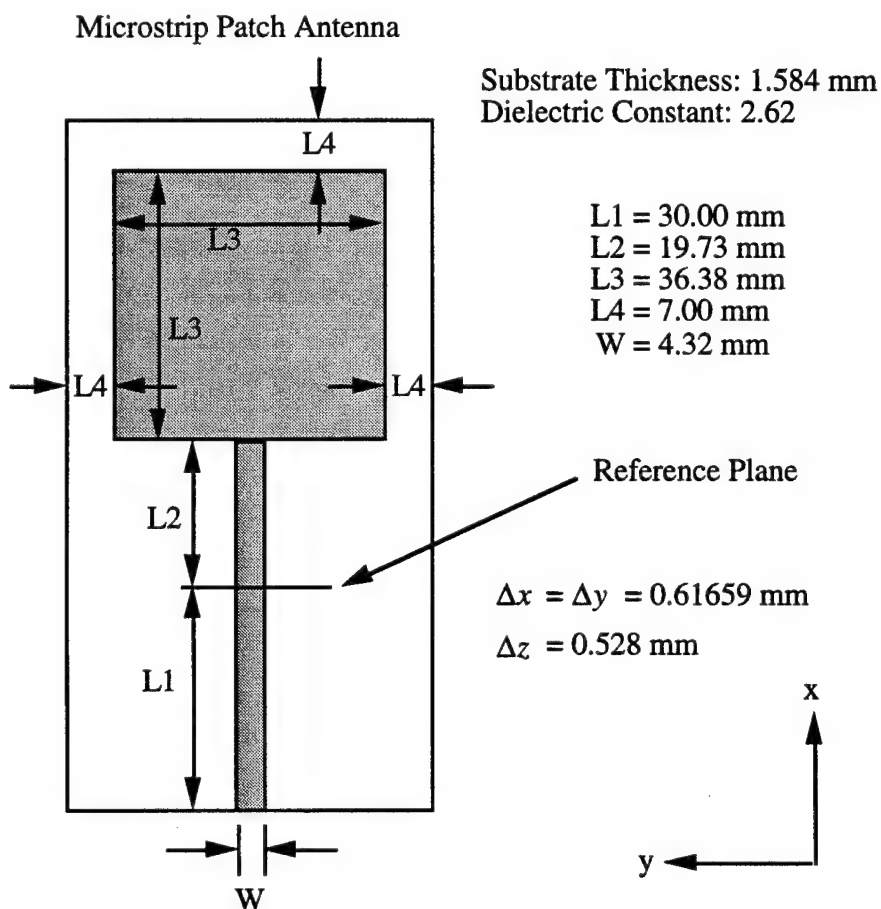


Figure 6.8 Microstrip-line fed patch antenna with finite ground plane.

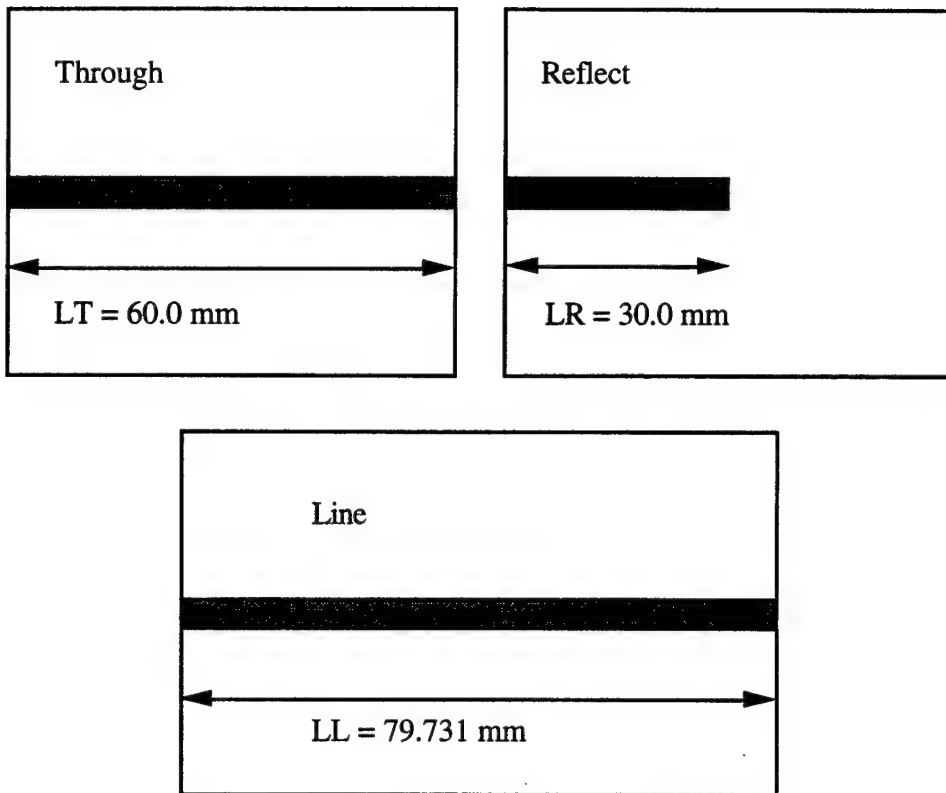


Figure 6.9 TRL standards used to calibrate network analyzer.

The Prony technique was used to calculate S_{11} at the reference plane. The magnitude and phase of S_{11} are plotted in Figs. 6.10 and 6.11. The agreement between the measurements and the FDTD results is excellent:

The far field was calculated as detailed in the previous section. The microstrip line was excited at the resonance frequency. The radiation pattern in the yz -plane is shown in Fig. 6.12. Measured values and FDTD results are both normalized to 30 dB at $\theta = 0^\circ$ for plotting purposes. Again, the agreement between the results is excellent. Note that there is significant power in the $z < 0$ half-space.

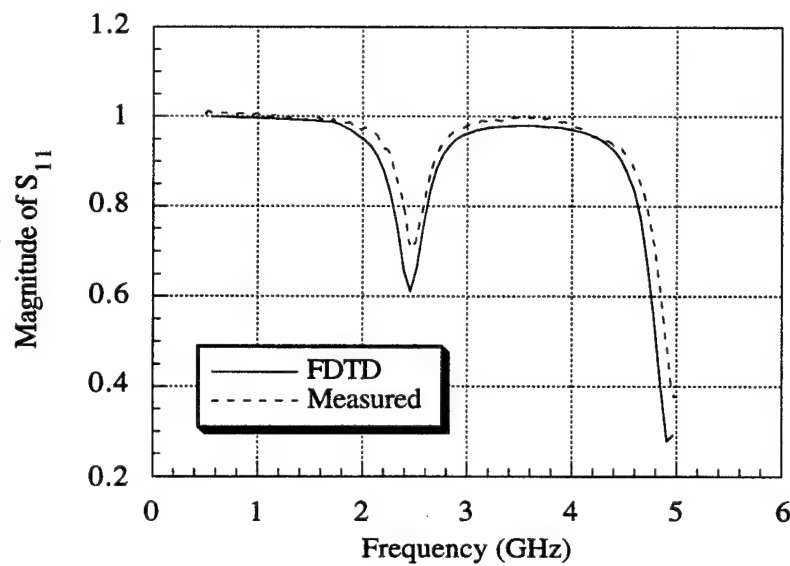


Figure 6.10 Magnitude of S_{11} for the microstrip patch antenna.

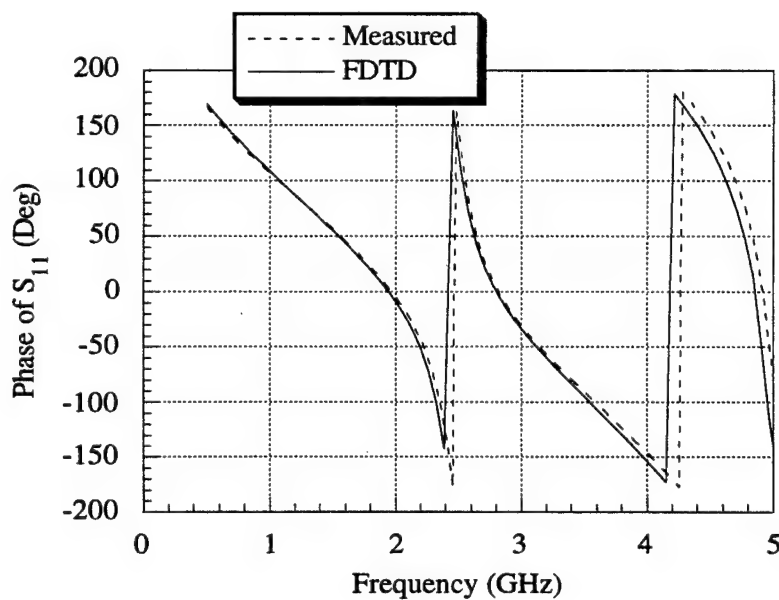


Figure 6.11 Phase of S_{11} in degrees for the microstrip patch antenna.

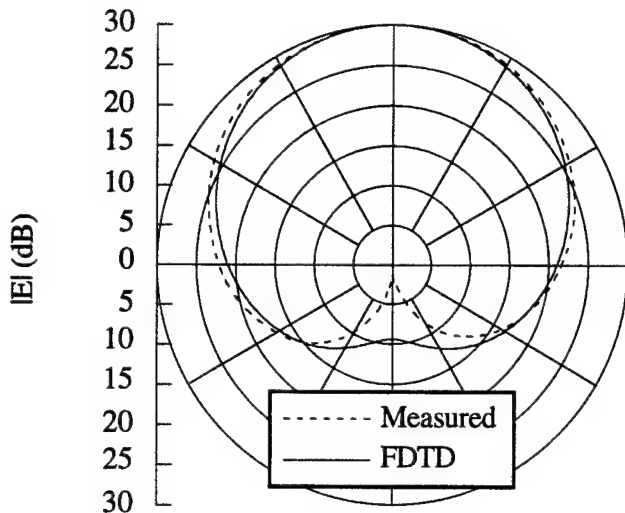


Figure 6.12 Far-field radiation pattern in the yz-plane. $|E|$ -phi vs. theta.

6.5 Coaxial-Line Fed Microstrip Patch Antenna

Not only does the nonuniform orthogonal approach result in considerable savings of memory and accelerate computation times, it also allows for the accurate modeling of rectangular geometries. In this section, a microstrip-line fed patch antenna is analyzed in order to demonstrate the reduction in required memory. Next, coax fed patches are analyzed, demonstrating the flexibility of the nonuniform mesh.

The microstrip-line fed patch antenna investigated in this section is similar to that shown in Fig. 6.8. The patch is 4 cm by 4 cm and the feed line is 10 cm long and 0.4 cm wide. The substrate is 0.15875 cm thick with a relative dielectric constant of 2.55 and the ground plane is infinite. This geometry was modeled using a uniform mesh that was 120 cells by 180 cells by 30 cells with $\Delta x = \Delta y = 0.1$ cm and $\Delta z = 0.0529166$ cm, and the simulation ran for 8192 time steps. Using the nonuniform feature in the z-direction, it was possible to model the same space with 15 cells as opposed to 30 cells. Since the number of unknowns was cut in half, the simulation was run for 16384 time steps in the

same amount of computation time as the uniform case. Doubling the length of the time signal gives twice as much resolution in the frequency domain. Figure 6.13 shows the magnitude of S_{11} computed using the uniform and nonuniform methods. Note that the nonuniform method shows a deeper null that is missed by the uniform method due to the shorter time signature. Increased resolution in the frequency domain could be obtained with the same total computer time by allowing the cells to grow in the x- and y-directions as well.

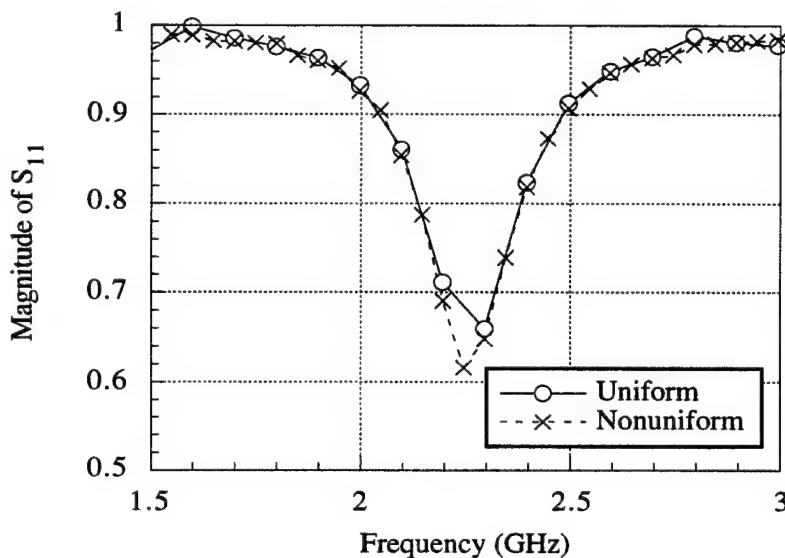
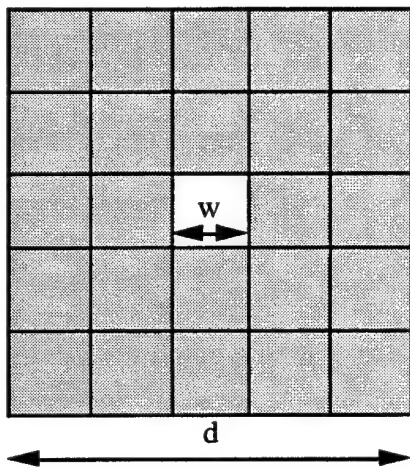


Figure 6.13 Magnitude of S_{11} of microstrip-line fed patch antenna. Uniform simulation had 8192 time steps and nonuniform simulation had 16384 time steps.

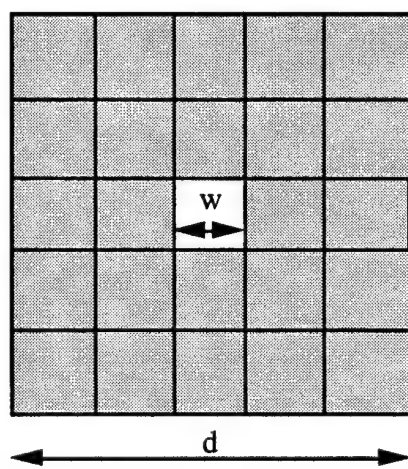
It is straightforward to model a microstrip line fed patch antenna. To obtain a $50-\Omega$ line, a circuit simulator is used to determine the width of the conductor given the substrate thickness and dielectric constant. The coax fed patch is slightly more involved. The circular inner and outer conductors are approximated by square conductors. This approximation is reasonable if the proper impedance can be obtained. Choices for feed impedances are severely limited using the uniform method. Equation (6.5) gives the ratio of the widths of the outer and inner conductors for a dielectric filled square coaxial line with impedance Z_o [6.15].

$$\frac{w}{d} = \frac{0.9259}{e^{Z_o \sqrt{\epsilon_r} / 59.37}} \quad (6.5)$$

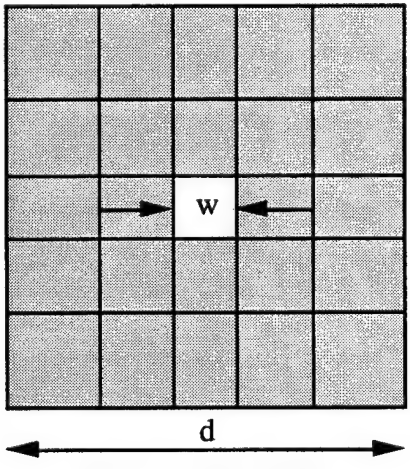
For the case of a 50- Ω line with $\epsilon_r = 3.6$, $d/w = 5.3383$. Clearly, this would be difficult to realize using a small number of cells and the uniform approach. However, with the nonuniform method, this ratio can be obtained using five cells in each direction as shown in Fig. 6.14.



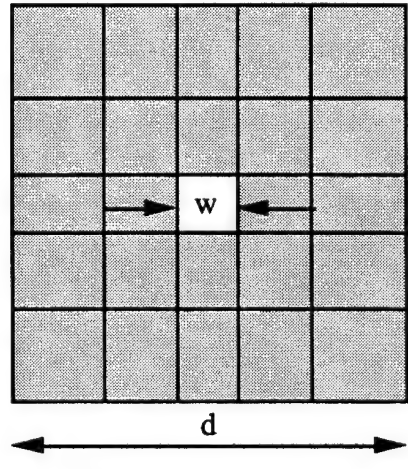
Case 1: $d/w = 5.3383$



Case 2: $d/w = 5.620$



Case 3: $d/w = 6.28$



Case 4: $d/w = 6.625$

Figure 6.14 Cross-sections of four different meshes to describe a 50- Ω square coaxial line. In all four cases, $\epsilon_r = 3.6$.

Unfortunately, the FDTD modeling of the ratios determined by (6.5) does not lead to the desired impedance, so the ratio of the widths of the inner and outer conductors was varied as shown in Fig. 6.14, and the resulting impedances are shown in Fig. 6.15. These results were obtained using the Prony technique described previously to extract the reflection due to the imperfect absorbing boundaries.

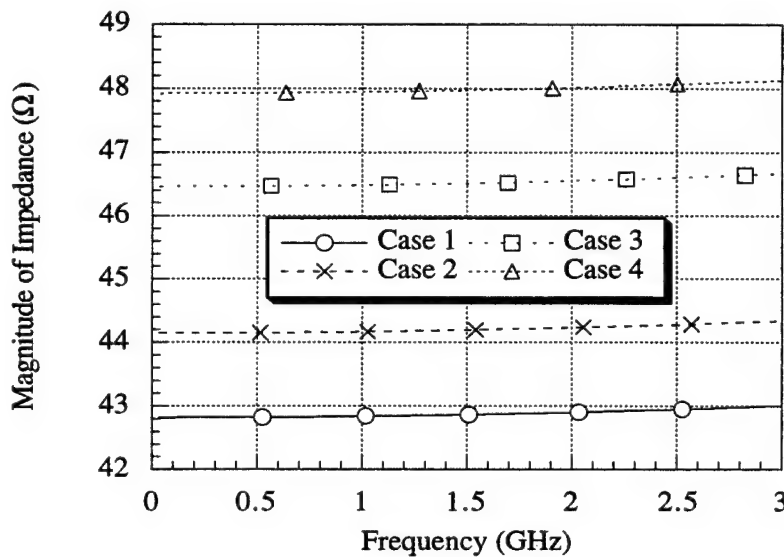


Figure 6.15 Magnitude of impedance of square coaxial line.

A coax fed patch antenna is shown in Fig. 6.16. The dimensions of the patch and the position of the feed point would require a prohibitively large computational domain using a uniform mesh. With the nonuniform mesh, the geometry is accurately modeled with a reasonable number of unknowns. The mesh is 111 cells by 111 cells by 93 cells, and there is approximately 60 mm between the patch antenna and the absorbing boundaries.

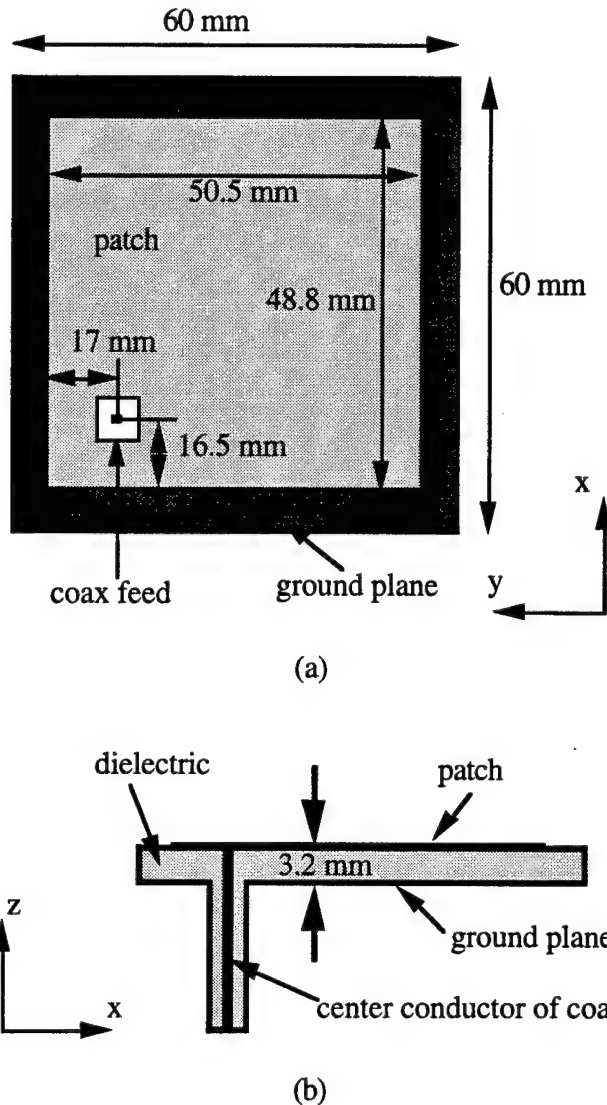


Figure 6.16 Coax fed microstrip patch antenna. The dielectric constant is 3.6. (a) Top view. (b) Side view.

The microstrip patch antenna was designed for circular polarization, built, and measured. Tuning stubs were used to enhance the performance of the antenna, but records of the sizes and locations of the stubs were not kept. Measured results are shown in Fig. 6.17, where the frequency starts at $f_1 = 1.48$ GHz and stops at $f_2 = 1.60$ GHz, and the location of the reference plane is unknown. This antenna was modeled using nonuniform orthogonal FDTD, and results are shown in Figs. 6.18 - 6.20, where the

frequency starts at $f_1 = 1.4420$ GHz and stops at $f_2 = 1.5461$ GHz, and the reference plane is located at the junction between the coaxial feed and the ground plane. The input impedance for the antenna is shown in Fig. 6.18. There is a loop near resonance, so the difference between the lengths of the sides has to be reduced for better performance. A 4.2 mm by 2.7 mm tuning stub was placed on the 50.5 mm side, effectively increasing the length of the shorter side. The input impedance for the antenna with this tuning stub is shown in Fig. 6.19. The cusp in the input impedance is not very deep, suggesting that the tuning stub is too large. The stub was reduced to 2.8 mm by 2.7 mm. The input impedance for the antenna with the smaller tuning stub is shown in Fig. 6.20. The difference between the measured and calculated resonant frequencies is less than 1.5%. Further refinements of the position and size of the tuning stub would further improve the agreement between the measured results and the FDTD results.

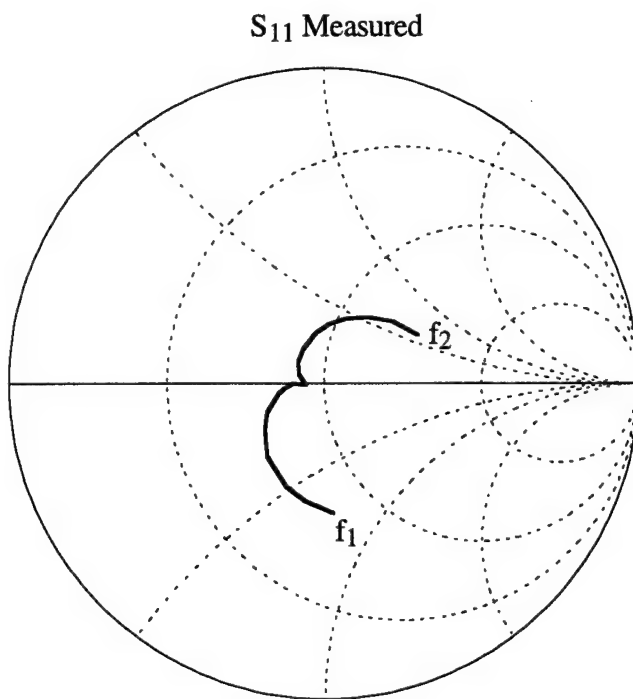


Figure 6.17 Measured input impedance of coax fed patch antenna. Frequencies f_1 and f_2 are 1.48 GHz and 1.60 GHz, respectively.

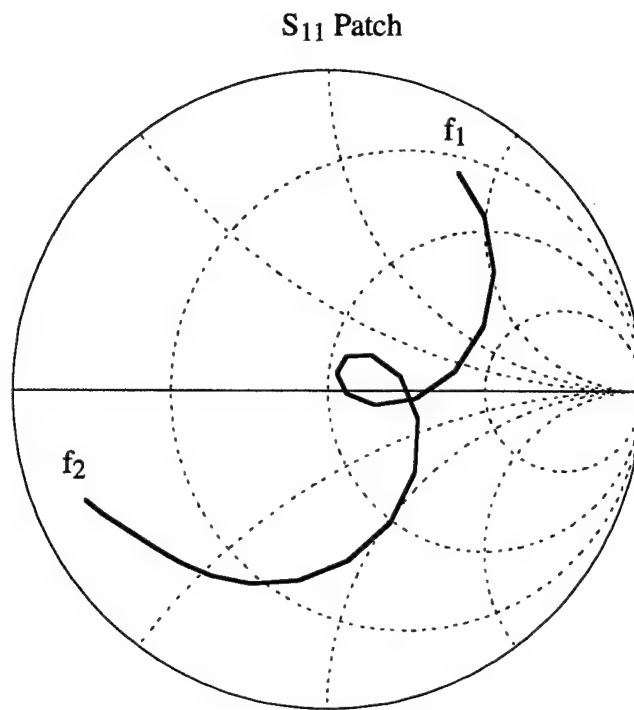


Figure 6.18 Input impedance of coax fed patch antenna. Frequencies f_1 and f_2 are 1.442 GHz and 1.5461 GHz, respectively.

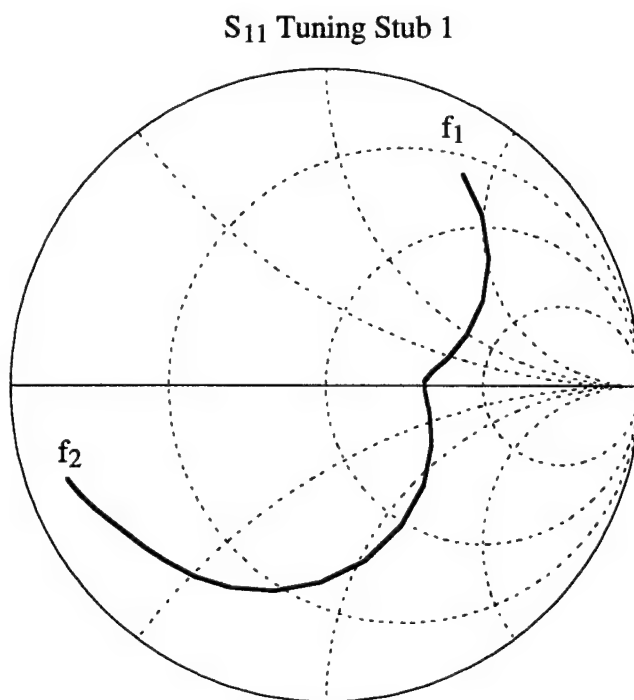


Figure 6.19 Input impedance of coax fed patch antenna with tuning stub. Frequencies f_1 and f_2 are 1.442 GHz and 1.5461 GHz, respectively.

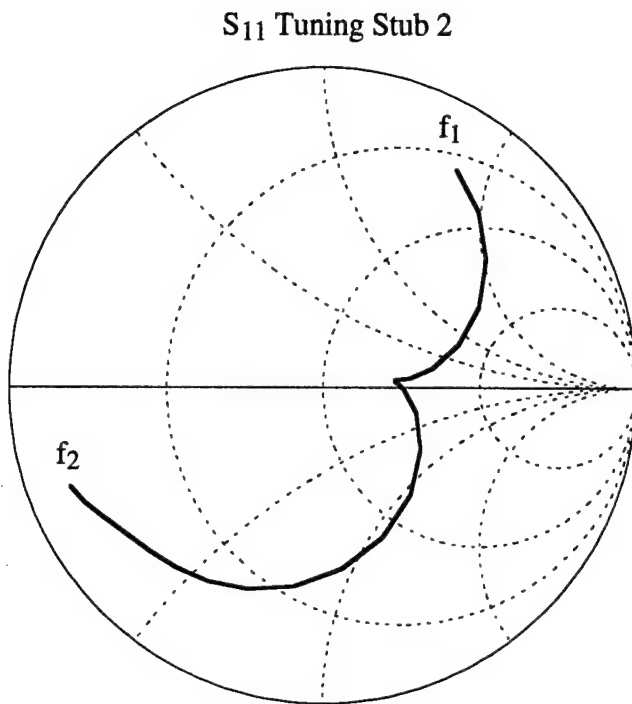


Figure 6.20 Input impedance of coax fed patch antenna with tuning stub. Frequencies f_1 and f_2 are 1.442 GHz and 1.5461 GHz, respectively.

6.6 Conclusions

The FDTD method was applied to analyze a very complicated geometry, namely a printed circuit folded dipole with an integrated balun. The numerical results from the FDTD model were compared with theoretical and measured results. The results for the radiation pattern were in excellent agreement with the measured data. However, the SWR calculations were much more sensitive to the modeling approximations. Therefore, a center fed microstrip line fed patch antenna was constructed, measured, and modeled with FDTD. The FDTD results were shown to be in excellent agreement with the experimental measurements. The nonuniform orthogonal method was used in order to accurately model coaxially fed microstrip patch antennas. The nonuniformity allows much greater accuracy in describing the geometry as compared with the uniform method,

which requires that patch dimensions and features be integral multiples of the cell discretization. Such a restriction is entirely impractical. Although the nonuniform grid gives enhanced modeling capabilites, there is room for improvement in the modeling and calculation of input impedance of coaxially fed patch antennas using the FDTD method, specifically for design purposes.

6.7 References

- [6.1] J. G. Maloney and G. S. Smith, "A study of transient radiation from the Wu-King resistive monopole - FDTD analysis and experimental measurements," *IEEE Trans. Antennas Propagat.*, vol. 41, no. 5, pp. 668-678, May 1993.
- [6.2] T. Kashiwa, T. Onishi, and I. Fukai, "Analysis of microstrip antennas on a curved surface using the conformal grids FD-TD method," *IEEE Trans. Antennas Propagat.*, vol. 42, no. 3, pp. 423-427, March 1994.
- [6.3] E. Thiele and A. Taflove, "FD-TD analysis of Vivaldi flared antennas and arrays," *IEEE Trans. Antennas Propagat.*, vol. 42, no. 5, pp. 633-641, May 1994.
- [6.4] S. Chebolu, J. Svilgelj, and R. Mittra, "Efficient modeling of microstrip antennas using the finite difference time domain method," *Proc. Ant. Appl. Symposium*, sec. III, pp. 1-22, Sep. 1994.
- [6.5] A. Reineix and B. Jecko, "Analysis of microstrip patch antennas using the finite difference time domain method," *IEEE Trans. Antennas Propagat.*, vol. 37, no. 11, pp. 1361-1369, Nov. 1989.
- [6.6] D. M. Sheen, S. M. Ali, M. D. Abouzahra, and J. A. Kong, "Application of the three-dimensional finite-difference time domain method to the analysis of planar microstrip circuits," *IEEE Trans. Microwave Theory Tech.*, vol. 38, no. 7, pp. 849-857, July 1990.
- [6.7] E. M. Daniel and C. J. Railton, "Fast finite difference time domain analysis of microstrip patch antennas," *IEEE APS Symposium*, vol. 1, pp. 414-417, June 1991.
- [6.8] C. Wu, K. L. Wu, Z. Bi, and J. Litva, "Modeling of coaxial-fed microstrip patch antenna by finite difference time domain method," *Electron. Lett.*, vol. 27, no. 19, pp. 1691-1692, Sept. 1991.
- [6.9] W. J. Buchanan, N. K. Gupta, and J. M. Arnold, "Simulation of radiation from a microstrip antenna using three-dimensional finite-difference time-domain (FDTD) method," *Proc. Eighth Int'l. Conf. Ant. Propagat.*, IEE Conf. Publ. 370, pp. 639-642, 1993.
- [6.10] B. Toland, J. Lin, B. Houshmand, and T. Itoh, "FDTD analysis of an active antenna," *IEEE Microwave Guided Wave Lett.*, vol. 3, no. 11, Nov. 1993.

- [6.11] A. Taflove and K. Umashankar, "Radar cross section of general three-dimensional scatterers," *IEEE Trans. Electromagn. Compat.*, vol. EMC-25, pp. 433-440, November 1983.
- [6.12] K. S. Yee, D. Ingham, and K. Shlager, "Time-domain extrapolation to the far field based on FDTD calculations," *IEEE Trans. Antennas Propagat.*, vol. 39, no. 3, pp. 410-413, March 1991.
- [6.13] R. J. Luebbers, K. S. Kunz, M. Schneider, and F. Hunsberger, "A finite-difference time-domain near zone to far zone transformation," *IEEE Trans. Antennas Propagat.*, vol. 39, no. 4, pp. 429-433, April 1991.
- [6.14] P. M. Proudfoot, "A printed circuit folded dipole with integrated balun," RADC-TR-89-237, October 1989.
- [6.15] Y. T. Lo and S. W. Lee, *Antenna Handbook*. New York: Van Nostrand Reinhold, 1988.

CHAPTER 7

CONCLUSIONS AND FUTURE WORK

The nonuniform orthogonal FDTD method was developed and demonstrated on a wide variety of problems. The nonuniform orthogonal FDTD method is superior to the conventional FDTD method in several aspects. The nonuniform discretization provides great flexibility in modeling geometries, whereas dimensions must be integral multiples of a fixed cell discretization in the conventional method. Moreover, the ability of the mesh to be dense in areas of interest and then gradually expand to a relatively coarse mesh makes it possible to efficiently analyze two classes of problems. These classes of problems are (a) geometries with fine features, and (b) large geometries. Furthermore, the orthogonality of the method preserves the speed of the conventional method.

Chapter 2 presented the nonuniform orthogonal FDTD method. Update equations were derived from the general curvilinear FDTD update equations and shown to be of the same form as the conventional update equations, thus demonstrating the preservation of the speed of the update equations. Memory requirements were shown to be only marginally larger than for the conventional method. This is significant when compared with the curvilinear method, which is expensive in terms of both memory requirements and loss of speed. The error associated with the nonuniform grid was discussed. A numerical example demonstrated that gradual growth rates in the mesh discretization lead to errors that can be maintained at acceptably low levels. A more rigorous approach to the analysis of the nonuniform grid error is suggested for future work.

A dipole radiating in the presence of lossy layered media was analyzed, and shown to give excellent results when compared with analytic and moment method results. The nonuniform orthogonal FDTD method resulted in significant savings of memory and computation time when compared with the conventional FDTD method. The nonuniform orthogonal FDTD method was also applied to the finline waveguide structure. The

FDTD results obtained were shown to be in good agreement with results from the regular solution of the singular integral equation.

Chapter 3 provided a numerical analysis of the dispersive boundary condition (DBC) applied to nonuniform grids. Stability and dc offsets were discussed, and the DBC was tested with radiating and guided wave problems. Error analysis was carried out in the time domain, the frequency domain, and spatially. Analysis of Liao's ABC applied to nonuniform grids is a suggested direction for further study.

Chapter 4 presented a variety of methods for calculating the frequency-dependent characteristics of microstrip lines, striplines, and discontinuities. A Prony technique with the FDTD method was presented and applied to two-port scattering parameter calculations. A local mesh refinement technique was introduced for triangular metallization and demonstrated to increase the accuracy of the FDTD method. The FDTD method and Prony technique were combined to analyze the complicated transition from a grounded coplanar waveguide to a microstrip line. Further analysis of the microstrip line to the grounded coplanar waveguide transition is suggested. Microstrip or coplanar waveguide stubs should be able to provide a good match at frequencies of interest.

The methods of Chapter 4 were extended in Chapter 5 to handle a broader class of problems. The new method was presented, followed by numerical examples analyzing coupled symmetric and asymmetric lines. A multidielectric asymmetric coupled stripline problem was also analyzed. A possible avenue for research involves applying the general pencil-of-function method in a manner similar to that presented in Chapter 5. This method should permit the extraction of general modal information for arbitrary coupled line structures.

Chapter 6 discussed the application of the FDTD method to analyze microstrip antennas. A near-field to far-field transformation was discussed, followed by the analysis of a complicated balun-fed folded dipole antenna. The benefits of using the nonuniform

orthogonal FDTD method were demonstrated through the analysis of microstrip patch antennas. The results obtained were compared with experimental measurements. Excellent results were obtained for the microstrip line fed patch antenna. However, improvements can be made to calculate the input impedance more accurately when modeling coaxially fed microstrip patch antennas.

VITA

John Allan Svilgelj was born in Akron, OH, on March 23, 1968. He attended Michigan State University, where he was a Distinguished Freshman Scholar, an Eastman Kodak Scholar, and a National Merit Scholar. In the summer of 1988, he worked at Eastman Kodak in Rochester, NY, developing interface software for a video proofing system. During his senior year at Michigan State, he conducted undergraduate research in the area of traveling wave antennas. He graduated with high honors from Michigan State University with a B.S.E.E. in 1990. He enrolled at the University of Illinois at Urbana-Champaign, where he held fellowships from the University of Illinois and Northrop Corporation, for the 1990-1991 academic year. He was awarded a Department of Defense fellowship for the 1991-1994 academic years. He earned the M.S.E.E. in May of 1992. He spent the summer of 1993 conducting research at Rome Laboratory, Hanscom Air Force Base, MA. He held teaching assistantships in electromagnetics and a Northrop fellowship for the 1994-1995 academic year.

Mr. Svilgelj is a member of Eta Kappa Nu, Tau Beta Pi, Phi Kappa Phi, Pi Mu Epsilon, and the Institute of Electrical and Electronics Engineers. He is the co-author of the following publications

- [1] L. W. Epp, K. W. Whites, J. Svilgelj, K. O. Merewether and R. Mittra, "An analysis of lossy, finite frequency selective surfaces using the resistive boundary condition and an impedance boundary condition model," *Proc. IEEE-APS Int. Symp.*, London, Ontario, Canada, pp. 268-271, June 1991.
- [2] John Svilgelj, E. Michielssen, and R. Mittra, "Numerical study of the chiral properties of the wire helix and periodic arrangements of wire helices," Electromagnetic Communication Laboratory Technical Report No. 92-1, May 1992.
- [3] J. Svilgelj, E. Michielssen, and R. Mittra, "Numerical study of chiral properties of the wire helix," *Proc. IEEE-APS Int. Symp.*, Chicago, IL, pp. 695-698, June 1992.
- [4] John Svilgelj, Eric Michielssen, and Raj Mittra, "Absorption characteristics of periodic arrangements of infinite helices," *IEEE Trans. Microwave Guided Wave Lett.*, vol. 2, no. 12, pp. 495-496, December 1992.

- [5] J. Svilaplj, E. Michielssen, and R. Mittra, "Chiral properties of isolated and periodic arrangements of helices," *Proc. Chiral '94 Symp.*, Perigueux, France, May 1994.
- [6] R. Mittra, W. L. Ko, P. Harms, U. Pekel, and J. Svilaplj, "Detection of high conductivity objects buried in seafloor sediments," *Proc. IEEE-APS Int. Symp.*, Seattle, WA, pp. 1426-1429, June 1994.
- [7] Siva Chebolu, John Svilaplj, and Raj Mittra, "Efficient modeling of microstrip antennas using the finite difference time domain method," *Proc. Antenna Applications Symp.*, Allerton Park, IL, September 1994.